uOttawa

L'Université canadienne
Canada's university

Fuel Residence Times for Clean Combustion of Coal in a Pressurized Fluidized Bed - Cold Flow Study

Marc-André Séguin

Thesis submitted to the
Faculty of Graduate and Postdoctoral Studies
In partial fulfillment of the requirements
For the M.A.Sc. degree in Chemical Engineering

Department of Chemical and Biological Engineering
Faculty of Engineering
University of Ottawa

Abstract

Anthropogenic Climate Change is amongst the greatest challenges of human civilization. A key area that will play a large role in mitigating its effects are clean fossil fuel applications. Clean coal combustion is one such application with an urgent timeline. This can be achieved with an oxygen-fired pressurized fluidized bed combustor with downstream carbon capture and sequestration. In relation to pressurized fluidization processes, understanding the influence of pressure on bed hydrodynamics and in turn their effect on parameters including fuel residence time is essential. For the proposed combustor, the heat exchanger boiler tubes are submerged in the fluidized bed such that the effect of a horizontal tube bank on the fuel residence time is also of great importance. The main focus of present work was to evaluate the impact of gas velocity, pressure, presence of a tube bank and fuel feed rate on the average fuel residence time. Experiments were conducted under cold flow conditions in a pilot-scale pressurized fluidized bed with an inner diameter of 0.15 m. The fluidization material was relatively large glass beads (1.0 mm in diameter) while the fuel particles were simulated with smaller glass beads (40 to 138 μm in diameter), susceptible to entrainment. Operating pressures and superficial gas velocities tested were between 101.3 and 1200 kPa and 0.4 and 1.1 m/s respectively. To simulate coal combustors, experiments were then conducted in a continuous mode where the fuel particles were continuously fed to the fluidized bed of large particles over a desired period of time. Downstream, entrained particles were continuously captured to determine the entrainment rate and mass of fuel particles inside the fluidized bed at steady state, which yielded the average fuel residence time. The combination of elevated pressure with the tube bank present was found to enhance gas bubble break up and reduce the average gas bubble size. In turn, this increased the average fuel residence time of 83 μm

particles by nearly 3 fold to a value of 77 s in comparison to 27 s at atmospheric pressure. The effect of gas velocity was not found to be statistically significant under the range tested. Similarly the effect of increased fuel feed rate by 50% neither had a statistically significant impact.

Keywords: Fluidized bed, residence time, tube bank, pressure, entrainment, fines.

Résumé

Le changement climatique anthropique est l'un des plus grands défis de la civilisation humaine. Un domaine clé qui jouera un rôle important dans l'atténuation de ses effets sont les applications propres aux combustibles fossiles. La combustion propre du charbon est une de ces applications avec un échéancier urgent. Don l'objectif de cette recherche, par l'intermédiaire d'une chambre de combustion à lit fluidisé sous pression alimenté à l'oxygène avec capture et séquestration du carbone en aval. En ce qui concerne les processus de fluidisation sous pression, il est essentiel de comprendre l'influence de la pression sur l'hydrodynamique du lit et, à son tour, son effet sur les paramètres, y compris le temps de résidence du carburant. Pour la chambre de combustion proposée, les tubes de chaudière de l'échangeur de chaleur sont immergés dans le lit fluidisé de sorte que l'effet d'une banque de tubes horizontaux sur le temps de résidence du carburant est également d'une grande importance. L'objectif principal du présent travail était d'évaluer l'impact de la vitesse du gaz, de la pression, de la présence de la banque de tubes et du débit d'alimentation du carburant sur le temps de résidence moyen du carburant. Les expériences ont été menées dans des conditions de circulation froide dans un lit fluidisé sous pression à l'échelle pilote avec un diamètre intérieur de 0,15 m. Le matériau de fluidisation était constitué de billes de verre relativement grandes (1,0 mm de diamètre) tandis que les particules de carburant étaient simulées avec des billes de verre plus petites (40 à 138 µm de diamètre) susceptibles d'être entraînées. Les pressions d'opération et les vitesses de gaz superficielles testées étaient entre 101,3 et 1200 kPa et 0,4 et 1,1 m/s respectivement. Pour simuler une chambre de combustion au charbon, les expériences ont été menées dans un mode continu où les particules de carburant étaient alimentées en continu dans le lit fluidisé de grandes particules sur une période de temps souhaitée. En aval,

les particules entraînées ont été capturées en continu pour déterminer le taux d'entraînement et la masse des particules de carburant à l'intérieur du lit fluidisé à l'état d'équilibre, ce qui a donné le temps de résidence moyen du carburant. La combinaison de la pression élevée avec la banque de tubes présente a été trouvée à améliorer la rupture des bulles de gaz et en sorte réduire la taille moyennes des bulles de gaz. Par la suite, cela a augmenté le temps de résidence moyen du carburant pour les particules de 83 µm d'environ un facteur de 3, à une valeur de 77 s par rapport à 27 s à la pression atmosphérique. L'effet de la vitesse du gaz n'a pas été trouvé statistiquement significatif dans la gamme testée. De même, l'effet de l'augmentation du débit d'alimentation du carburant par 50% n'a pas eu d'impact statistiquement significatif.

Mots-clés: Lit fluidisé, temps de résidence, banque de tubes, pression, entraînement, particules fines.

Table of Contents

List of Figures

List of Tables

Nomenclature

Symbols	Definition (units)
A_c	Fluidization column cross sectional area (m^2)
Ar	Archimedes number (-)
C_D	Drag coefficient (-)
$d_{B,\Delta P}$	Estimated average bubble size using pressure drop measurements (m)
$d_{crit.}$	Critical diameter where entrainment rate levels off
d_p	Particle diameter (m)
d_{pi}	Diameter of particle size (i) (m)
$\dot{E}$	Entrainment rate of fines at steady state (kg/s)
$\dot{E}_{ih}$	Entrainment rate of fines for particle size (i) at height (h) (kg/s)
g	Earth gravitational constant (9.81 m/s^2)
$h_{\Delta P,Freeboard}$	Height of the freeboard differential pressure measurement (m)
K_{ih}	Elutriation rate constant for particle size (i) at height (h) ($kg/m^2 \cdot s$)
m_{FB}	Mass of fines in the fluidized bed (kg)
$m_{Freeboard}$	Mass of fines in the entire freeboard section (kg)
$m_{Freeboard,\Delta P}$	Mass of fines in the freeboard DP measurement section (kg)
MW	Molecular weight of gas composition
P	Gas operating pressure
R	Ideal gas constant (8.3145 J/mol·K)
Re_p	Particle Reynolds number (-)
Re_t	Particle terminal Reynolds number (-)
t	Time (s)
T	Gas operating temperature
U_{ex}	Excess gas velocity (m/s)
U_g	Superficial gas velocity (m/s)
U_{mf}	Minimum fluidization velocity (m/s)
U_p	Particle velocity (m/s)
U_{slip}	Particle slip velocity (m/s)
U_t	Particle terminal velocity (m/s)
U_{ti}	Terminal velocity of particle size (i) (m/s)
x	Gas velocity exponent for entrainment rate correlation (-)
$x_{FB,i}$	Mass fraction of fines of particle size (i) in the fluidized bed (-)
$x_{E,i}$	Mass fraction of fines of particle size (i) in the entrained flow of fines from the fluidized bed (-)

Greek Symbols	Definition (units)
β	Systems constant for entrainment rate correlation (variable units)
ΔP	Pressure differential (Pa)
$\Delta P_{Freeboard}$	Differential pressure measurement in the freeboard (Pa)
Δt	Time interval (s)
ε	Gas voidage (-)
$\varepsilon_{Freeboard}$	Gas voidage in the freeboard (-)
ε_{mf}	Gas voidage at minimum fluidization (-)
ρ_f	Fluid density (kg/m^3)
ρ_g	Gas density (kg/m^3)
ρ_p	Particle density (kg/m^3)
$\sigma_{\Delta P}$	Standard deviation of the differential pressure fluctuations (Pa)
θ_{convey}	Particle residence time in the injector convey line (s)
θ_{Elbow}	Particle residence time in the large elbow above the fluidized bed (s)
θ_{FB}	Average fines residence time in the fluidized bed (s)
$\theta_{FB,i}$	Average residence time of particle size (i) in the fluidized bed (s)
$\theta_{Freeboard}$	Particle residence time in the freeboard (s)
$\theta_{to\ Filter}$	Particle residence time in the filter upstream piping (s)
θ_{total}	Residence time of fines in entire fluidization apparatus (s)
μ	Gas viscosity (Pa·s)

Acknowledgments

I would like to express my appreciation to my supervisor Dr. Poupak Mehrani and co-supervisor Dr. Arturo Macchi for their continued support, encouragement and knowledgeable insights throughout. I am incredibly thankful for Dr. Mehrani approaching me and giving me this opportunity to work on such a pristine research project. Not only was the research – clean coal combustion - extremely dear to my heart and enjoyable, as my supervisor she was very patient, flexible, trustworthy and inspiring. She has a great work ethic and was a great role model for myself. Dr. Macchi was incredibly insightful as well, it was always pleasant and educational catching up with him during our weekly meetings. He was a great outside observer, with thoughtful advice on our research project and even with everyday life.

I would like to extend my thanks to the remainder of the collective research group at the University of Ottawa, including: Di Song, Dr. Andrew Sowinski, Valois Parisien, Johnny Matta, Fawzi Salama, Fahad Chowdhury, Eric Mielke and Shazadi Rana who helped me design, commission, operate, and maintain the system, conduct experiments, in addition to our many shared discussions and theories relating to fluidization.

I would like to thank Dr. Robin Hughes for his incredible leadership at Natural Resources Canada CanmetENERGY and his knowledgeable team. He was the main anchor behind this incredible collective effort to advance clean coal combustion. He too, was very supportive, grateful, insightful and engaging during my research. Scott Champagne was another great contributor from CanmetENERGY, as he helped tremendously designing and commissioning the feeding system and capture system. David McCalden and Jeff Slater were also helpful throughout the commissioning of equipment to transition to our continuous experiments. At the head of the

collective partnership was our industrial client, Gas Technology Institue (GTI) in USA, for which I am very grateful for the contributions made by Bill Follett and Mark Fitzsimmons.

I would also like to thank the great help from undergraduate students that were under my supervision during the past two years. Namely, Ayoub Dayib (batch testing), Emi Luka (transitioning to continuous experiments), Jordan Hirano (tube bank experiments), Peter Gaudet (mitigating the effect of electrostatics) and Curtis Strong (finishing the experimental matrix).

Also this work could not have been completed without the fantastic help from the staff of the Department of Biological and Chemical Engineering at the University of Ottawa. Starting with our knowledgeable and quality technicians Louis Tremblay, Gérard Nina and Franco Ziroldo. Our helpful and kind administrative staff Francine Pétrin and Sylvie Saindon, and finally the remaining professors no matter how big or small their contributions were.

Finally, I would like to thank my friends, family and loved ones during this demanding but incredibly enriching experience. Despite the numerous long nights and early mornings, I always arrived home to a supportive and reassuring group of peers. Notably, my girlfriend Véronick Préseault, my brother Phil and my friend Rob. The same goes to all my friends whom I may not have been able to see as much, but when we did meet, they were always enthusiastic and we made the most of it. A big final thanks goes to my two incredible parents Nicol Séguin and Anne Proulx-Séguin, whom I love very much, and have raised me with all the right qualities and attributes to complete this journey successfully.

This material is based upon work funded in-part by the United States Department of Energy under Award Number DE-FE0009448 and in part by the Government of Canada's Program of Energy Research and Development. This report was prepared as an account of work sponsored by

In addition, a portion of the project funding was provided by Alberta Innovates.

Chapter 1. Introduction

1.1. Climate Change

Climate Change is a hot topic issue today for multiple reasons. Some people are in profound disbelief, others fear the idea of *another* tax, and on the other end of the spectrum, some are afraid of turning Earth into an inhabitable inferno. Despite the mixed opinions, most of the controversy stems from the fact most solutions to help combat and mitigate the effects of Climate Change – proposed, though of and discovered - also entail a very different way of life for the average citizen, business and government body. A way of life that includes limited fossil fuel use, greater environmental awareness, carbon pollution taxation, costly new capital investments, investment in sustainable infrastructure, mass electrification and increased energy efficiency among others. For some, the challenge of changing their lifestyles or business practices seems to outweigh the negative consequences of Climate Change, motivating inaction. Meanwhile, there are those who see fighting Climate Change as part of the grander fight to achieve human sustainability on Earth and therefore are fully committed. After all, the continuous use of fossil fuels is not sustainable.

In the end, one thing is certain, human induced Climate Change is real, and it is happening [1]. The only uncertainty is the rate at which the climate is warming and changing. In any case, significant changes have already been observed; atmospheric CO_2 concentrations alone have risen nearly 35% since 1750, from 280 ppm [2] to 390 ppm in 2011 [3], the highest level in 800,000 years. Now, as of March 2016, the 400 ppm milestone in atmospheric CO_2 concentrations has been attained [4]. In order not to destabilize our Climate, the safe level of carbon dioxide in the atmosphere was said to be 350 ppm [4].

In parallel, average temperatures have also seen a significant increase both locally and globally. On a global scale, the average temperature on Earth has approximately increased by 0.8°C from pre-industrial years in 1880 to present day 2016 [5, 6, 7]. However, the increase in temperature by Climate Change is even more pronounced around the poles and in polar countries such as Canada. For instance, in Artic Canada, the temperature was seen to increase by 1.6-2.2°C for a sampling period of 1948 to 2009 [8]. Since the sampling period does not date back to the year 1880, the actual rise in temperature for Artic Canada from 1880 to 2016 would be even greater than the reported 1.6-2.2°C. Nonetheless, it is evident that the Canadian Artic is warming at greater, alarming rate [8]. By extension, the same can be said for Canada altogether, as Southern Canada reported an average temperature increase of 0.9-1.7°C from 1948 to 2009 [8]; again greater than the average global temperature increase. Finally, the scientific consensus is well established with 97% of climate scientists in agreement on the long term effects of Climate Change [1].

More importantly, is the cost of inaction – as can be seen from the negative effects described below. It is much greater than the cost of action, and the detrimental costs associated to Climate Change will only escalate [3]. Thus, it is imperative action is taken now such that the latter, graver effects can be mitigated for future generations.

Negative effects of Climate Change are plentiful and go well beyond increased temperatures and atmospheric CO_2 concentrations. They include increased drought, violent precipitations, extreme weather events, species extinction, ocean acidification and coral bleaching. In addition, there will be increased area burned by wildfires, threats to human health, ecosystems in peril, sea level rise, flooding, coastal erosion, glacial retreat and loss of and increased damage to infrastructure. There will also be decreased Arctic sea ice, ice sheets in Greenland and Antarctic,

snowpack, permafrost, streamflow in rivers and crop productivity. As a result, the snow season will continue to shorten, while our summers experience uncomfortable heat waves. But this can all be avoided, or at the very least mitigated.

More problematic is the notion that Climate Change due to carbon dioxide – and its effects – will persist for many centuries to come [3]. Simply, because equilibrium of carbon dioxide between the atmosphere, biosphere and oceans is a slow, global process occurring over decades to millennia [3]. This is unique to carbon dioxide as other greenhouse gases (GHGs) attain much quicker equilibrium [3]. As a result, even if emissions were halted today, Climate Change caused by carbon dioxide will persist for many centuries [3]. Finally, what is also dreadful, is the ability of Climate Change to experience a positive feedback and self-accelerate. For example, the ability of currently trapped, stable carbon gases being released by the warming of permafrost and the oceans due to higher temperatures. In turn, the stable carbon gases released will further accelerate Climate Change, further increasing global temperatures, and the cycle continues. Hence the positive feedback. Another example, is the decrease in sea ice, a surface very reflective of sunlight, however as it melts, and loses surface area to opaque sea water, the energy is no longer being reflected but instead, most is being absorbed. On a last note, it is worth highlighting the biggest human induced causes of carbon pollution fueling Climate Change. Only by addressing the problem at its source can it be stopped effectively.

1.1.1. Primary sources of GHG emissions and carbon pollution

There are many contributing factors for increased GHG emissions and the most notable sources are discussed in order to have a complete overview of Climate Change, and its possible mitigation. The key is identifying which sectors are the biggest emitters. Discussing the relevant

efficiencies of each process using fossil fuels is also important. Figure 1.1 demonstrates the global GHG emissions by economic sector and indicates clearly the biggest GHG emitting sectors; of which 4 sectors were found to account for approximately 84% of all GHG emissions.

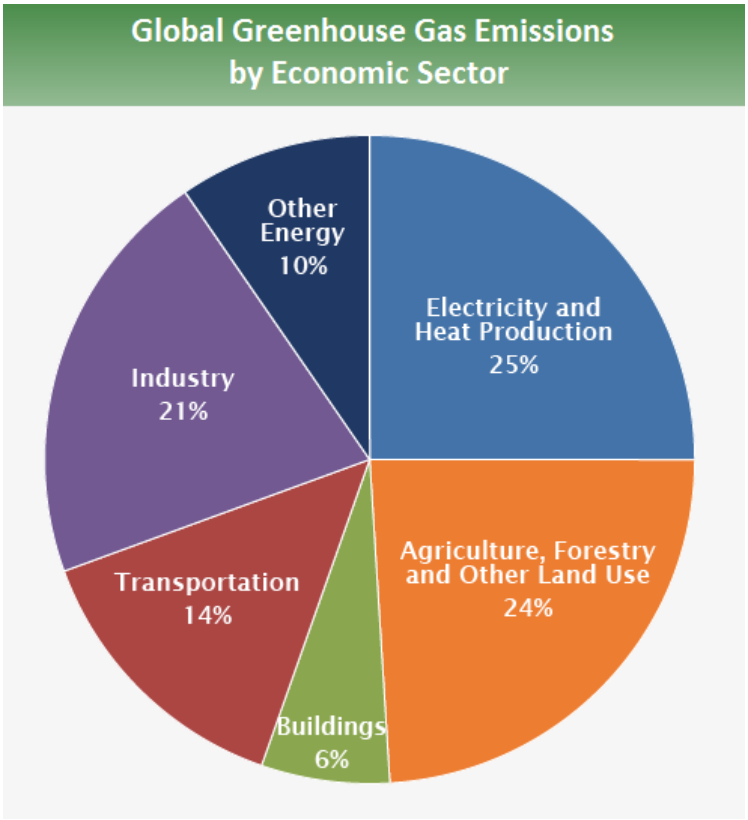

Figure 1.1. Global greenhouse gas emissions by economic sector [9].

These 4 big emitting sectors include: Electricity and Heat Production – Agriculture and Deforestation – Industry – Transportation. Starting with electricity and heat production. The biggest problematic in this sector regarding GHG emissions is the use of carbon-intensive fossil fuels like coal for production of heat and electricity. Switching to zero-emission processes, utilizing carbon capture and sequestration, using less carbon-intensive fossil fuels like natural gas and embracing renewable energy production would go a long way to mitigate future emissions in this sector.

Agriculture, forestry and land use also account for a very large share of GHG emissions [9]. Deforestation is a big culprit fueling Climate Change as it diminishes the ability of the biosphere to absorb carbon dioxide. Deforestation is often associated to agriculture, for which its GHG emissions have come under scrutiny under recent years, with profound results. Meat, cheese and eggs have the highest carbon footprint ranging from 4.8-39.2 kg $CO_{2,equivalent}$/kg of food [10]. In contrast, fruits, vegetables, whole grains, legumes, nuts and seeds have much lower carbon footprints ranging from 0.9-2.9 kg $CO_{2,equivalent}$/kg of food [10]. Since agriculture is inter-connected and dependent on other sectors e.g. electricity production, the World Bank in 2009 concluded that livestock farming (animal agriculture) accounted for approximately 51% of all GHG emissions [10]. This confirms two things, the importance of looking into the respective efficiencies of each process, and second, the substantial changes that are needed to the Western lifestyle to adequately and effectively combat Climate Change.

The third sector to discuss is industry, which notably has better efficiencies with the heat generated from fossil fuel combustion. The reason being that industry often uses the heat directly as is, rather than producing mechanical work via an engine, turbine, etc. [11]. As such, industry efficiencies in terms of useful energy extracted from the energy of fossil fuels is quite good at approximately 80% compared to 30-40% and 15-25% for electricity production and transportation [12].

Next, emissions associated to the transportation of goods and humans are discussed as they account for 14% of global GHG emissions as seen in Figure 1.1. Again, looking at the process more closely, large inefficiencies arise. For instance, the mass embrace of transport trucks to carry freight instead of trains for long distances [13, 14]. Another case of inefficiency in transportation

is how humans themselves move around; where the average small sedan car weighs approximately 1250 kg [15], the average person only weighs 80 kg [16], thus there is a big energy penalty when you are carrying an excess of 16 times your weight everywhere. Compared to a bicycle weighing 20 kg, or walking, for short trips, the automobile can be a big waste of energy.

Finally, the materialistic and consumer nature that has developed in society over the past decades has also been a great source of energy consumption. For all goods produced and their package, there is a significant carbon debt in its production, such that the more humans consume, the more fossil fuels are burned to accommodate production. The effect is compounded by poor waste management practices relying on landfills and incinerators, both producing further GHGs over the products entire lifecycle. In addition, there is the resource extraction associated to all the consumption that further stresses the limited resources of the planet.

Now consider a growing population, expected to reach 9.7 billion people by year 2050 [17], up from 7.3 billion people in 2015 [17]. The increase in population will further aggravate the emissions associated to each sector as the demand increases for all: electricity, heat, industry, transportation, agriculture and buildings. Although, some would argue an increased population is the last thing needed during these difficult times, it depends. Will the additional 2 billion people be driving cars or bicycles? Will they be eating pork or lentils? Will they drink tap water or use single-use plastic water bottles? One scenario is certainly problematic.

At last, there is also the inability for humans to respect and *love* one another due to religious, political, economical or racial reasons. It doesn't help. Whether it is petty crime amongst

one another, or large scale *war* as has been witnessed in Syria among others [18, 19], it's a waste. A waste of human resources, human energy and energy altogether.

As a result, there are many factors contributing to the rise in global GHG emissions which in turn is fueling Climate Change. However, between science, innovation and common sense, there is hope for humanity as the possibilities to tackle Climate Change are both endless and practical. At an individual level, there is much that can be done. Governments must also take true leadership and lead forward where it is most economical and practical. Framing the issue is also important for governments such that everyone can be aware of the issue, the consequences of inaction and the various possibilities for action. Finally, industry and the private sector must play its part as well, it is a team effort between all three levels.

1.2. Clean Coal Combustion Application

The research conducted for this thesis is part of a grander collective that plans to build an economical zero-emissions coal power plant for heat and power generation. The project is ambitious, but the reward is worthwhile as coal is one of the most carbon-intensive fossil fuels to burn. In order to do so, and to remain economically competitive, the project is being innovative in many different aspects. Currently, low emission coal power plants have found success preventing most emissions including particulate matter, NO_x and SO_2 emissions among others [20, 21]. However, the CO_2 emissions have remained untargeted. Originally this was primarily due to CO_2 being inert and non-toxic, but with the emerging effects of Climate Change, this is no longer the case. Second, unlike other pollutants, CO_2 emissions are being generated in much greater quantities, of which the downstream separation has been traditionally costly (e.g., the use of amine scrubbing [22]). The separation is typically costly because it requires removing gaseous CO_2 from the predominantly gaseous nitrogen (N_2) post-combustion flue gas.

With that said, for the zero-emissions coal power plant being discussed, it is proposed to combust the coal with nearly pure oxygen rather than air, eliminating the majority of inert nitrogen from the flue gas entirely. Therefore, the downstream separation of CO_2 is much more economical as the post-combustion flue gas is mostly composed of CO_2 and water. As a result, the primary separation of CO_2 is physical rather than chemical, as the water vapor is condensed out from the flue gas. Although the upstream cost of operation is increased by using nearly pure oxygen, it is justified by a simpler, more economical downstream separation of CO_2. Worth noting, oxygen is currently the second-largest volume industrial gas [23, 24] and because oxygen is a highly valuable, reactive chemical, used in many industrial, commercial, medical, and scientific

applications [23], there are many parties seeking cost reductions. In turn, this should continuously drive substantial research and development in the area. The end result could be less expensive high grade oxygen in the future, making the zero-emissions coal power plant even more economical. Furthermore, by using nearly pure oxygen, it improves the reaction kinetics and reduces the sizing of equipment. The remaining trace impurities in the flue gas after the condensation of water vapor (O_2, N_2, NO_x, SO_2, CO) would be dealt with sorption technologies. This yields a high purity CO_2 stream that once compressed and liquefied would be ready for sequestration underground. Which is economical if the Oxy-PFBC operates in a jurisdiction with a price on carbon emissions as this cost would be exempted.

Regarding the design of the combustor, it has many innovative and advantageous features. First, the coal is pulverized (20-300 μm in diameter) and injected into a fluidized bed of substantially larger particle size (1000 μm in diameter). The fluidized bed will provide good heat transfer rates as the boiler tubes are submerged in the fluidization media. It will also enable good mixing patterns, reducing concentration and temperature gradients. The large bed material will be dolomite, which has the ability of capturing the bulk of SO_2 emissions. Furthermore, because the bed material is substantially larger, it should disengage from the ash relatively easy, as the ash is carried away (entrained) by the fluidization gas. It is also envisioned to combine this technology with a more efficient power cycle using supercritical CO_2 instead of water as the working fluid. Lastly, the fluidized bed combustor will operate at elevated pressures of 600-1200 kPa which will further increase combustion kinetics and once more, reduce equipment size. A concept vision of the zero emissions oxygen-fired pressurized fluidized bed combustor (Oxy-PFBC) and the surrounding coal power plant is illustrated in Figure 1.2.

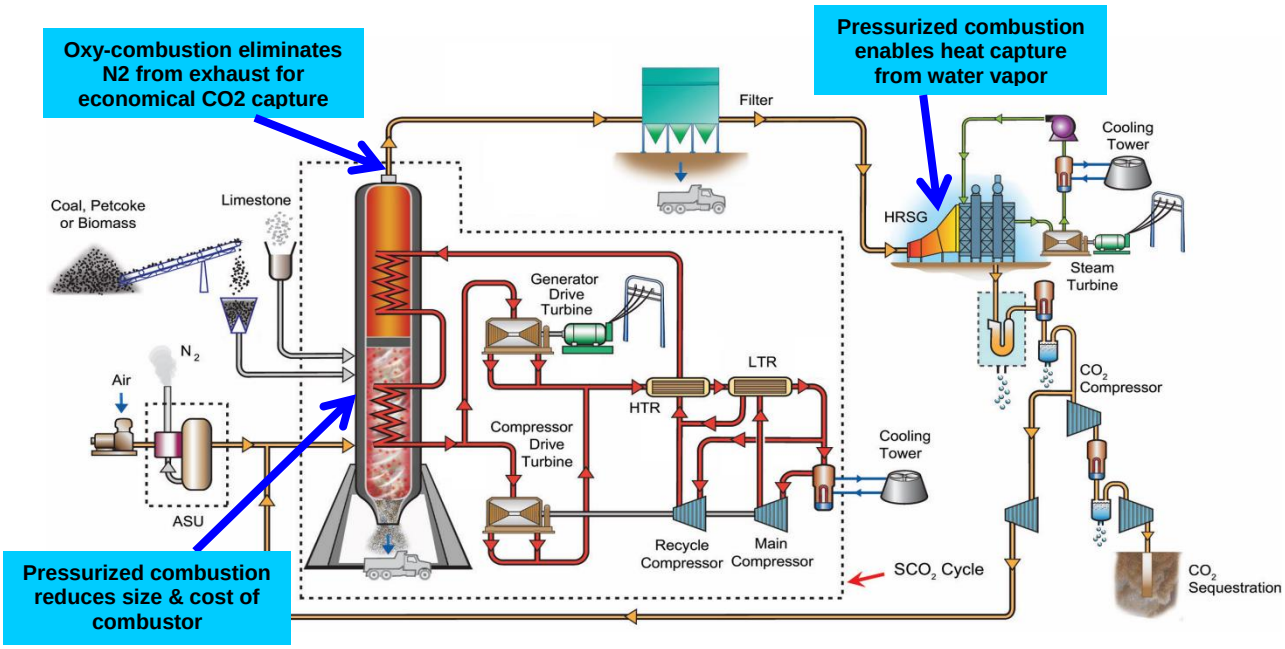

Figure 1.2. Zero emissions Oxy-PFBC power plant concept vision, courtesy of Gas Technology Institute, USA.

It goes without saying, the zero-emissions coal power plant is only possible by sequestering the emitted CO_2 in an underground reservoir. Of which, depleted, old oil wells and saline aquifers offer potential geological storages. Thankfully, research and development in the area of carbon sequestration is also being driven by many additional outside parties which could be of future benefit. This would make the application nearly carbon neutral which has large appeal in a world trying to mitigate the effects of Climate Change and carbon pollution. Furthermore, by introducing a low amount of biomass (5-10 wt%) in the coal feedstock, it has the possibility of even being carbon negative, which is exceptional for a fossil fuel application, and again of great value. This technology could also be applied to other carbon-intensive solid fuels such as petroleum coke.

Also of interest, is the possibility of having a lower carbon debt in the construction and operation of the zero-emissions coal power plant for heat and power generation in comparison to equivalent carbon neutral renewable energies. Renewable energy such as solar, wind,

hydroelectricity or geothermal, may be more appealing than coal, however could entitle a larger use of fossil fuels, GHG emissions and carbon debt in their respective construction. One reason may lie in the fact that for a zero emissions coal power plant, the process is only being upgraded, rather than started from anew such as in the case of a large concrete hydro dam, solar or wind farm, etc. Thus, the application could be a very effective, appealing, less-disruptive and economical way of fighting Climate Change and carbon pollution at home and abroad.

Finally, it is worth mentioning that this is a diverse collaborative research partnership between academia, governments and the private sector. It includes the United-States Department of Energy (DOE), Canada's CanmetENERGY branch in the Department of Natural Resources Canada (NRCan), the Gas Technology Institute (GTI) and Linde among others. During the time of this research, a 1 MW^{th} pilot plant facility was being designed and built at NRCan CanmetENERGY in Ottawa over the past 2 years. For which, the goal of this research was to provide design and operational data for the pilot plant. More specifically, to provide experimental data concerning the residence time of fuel particles in the fluidized bed when operating at elevated pressure and with boiler tubes submerged in the fluidized bed.

1.3. Research Objectives

The fuel residence time in the zero-emissions oxygen-fired pressurized fluidized bed combustor is of great interest as it is a key parameter determining the reaction conversion. Therefore, this research was tasked with determining the average fuel residence time under cold flow, unreactive conditions. To simulate the fuel (coal) particles, fine glass beads (fines) with an equivalent range of terminal velocities were used. Similarly, for the large dolomite bed material, glass beads were used with a mean size of 1 mm. This effectively yielded a binary particle mixture upon which the fine glass beads would be entrained, and as a result would have a given average residence time in the fluidized bed.

Specific objectives were to evaluate the effect of pressure, gas velocity, fuel feed rate and presence of a tube bank on the fines average residence time. The effect of pressure was evaluated at pressures of 101, 600 and 1200 kPa. Gas velocity was varied between 1.5 and 3.2 U_{mf} (factors of the minimum fluidization velocity) depending on the operating pressure. Two particle sizes for the fine glass beads were used with Sauter mean diameters of 64 and 83 μm (um). The effect of having a tube bank in the fluidized bed (simulating the in-bed heat exchange tubes in the combustor) was compared to that of a free bed (no tube bank present). Finally, the effect of fuel feed rate was investigated at 5.9 and 8.9 kg/h.

1.4. Thesis Outline

In addition to the introduction found in Chapter 1, there are 5 additional chapters in this thesis. Following the introduction, Chapter 2 presents the pertinent literature review associated to the entrainment and average residence time of fines in a gas-solid fluidized bed. Chapter 3 presents the experimental methods used to conduct the measurements and its originality. Chapter 4 then focuses on the fluidized bed hydrodynamic results as it provides additional information and insights relating to the analysis of the average residence time of fines. In accordance, Chapter 5 presents the effects of the 4 operating variables – pressure, gas velocity, fines feed rate and presence of tube bank – on the average residence time of fines. Finally, Chapter 6 presents the conclusion, recommendations and future work. The thesis also includes 5 Appendices, providing detailed pictures of the fluidization apparatus (A), the schematic of the tube bank (B), supplementary information on the fines particle size distribution (C), fines terminal velocity (D), and operating gas velocities and minimum fluidization velocities (E).

Chapter 2. Literature Review

Chapter 2 provides a literature review on the following topics: fluidization regimes and classifications of powders, entrainment principles, measurement techniques for the entrainment rate, effects of pressure on entrainment, fluidized bed bubble dynamics measurement techniques, effect of tube bank on bed hydrodynamics, particle velocity, entrainment correlations and fines particle residence time in a continuously fed fluidized bed.

2.1. Fluidization Flow Regimes and Classification of Powders

In future sections within Chapter 2, references are often made to specific fluidization flow regimes or specific types of powders/particles. Both are key, and provide the basic knowledge for understanding the various fluidization behaviour. Various fluidization regimes are illustrated in Figure 2.1. First the bed of particle begins in a fixed static position; upon increases in the gas velocity, it will eventually overcome the minimum fluidization velocity upon which the bed becomes fluidized. The onset of fluidization is either distinguished by particulate fluidization, where no discrete bubbles are found as the gas flow remains in between inter-particle channels. The other more common case is gas bubbles forming with the onset of minimum fluidization. If gas bubbles remain small in size (gas bubble diameter smaller than 40% of the column diameter [25]), which is initially the case, then this corresponds to the bubbling regime. As gas bubbles grow larger than 40% of the column diameter with increased gas velocity, they are referred to as slugs – large rising pockets of gas with minimal solids content. When the formation of slugs occurs, it is defined as the slugging regime. Increasing the gas velocity furthermore results in turbulent fluidization where no discrete repetitive flow patterns are observed. Following, with even greater gas velocity, the drag on the particles becomes increasingly strong where particles are entrained

entirely from the fluidization bed. If particles are being recirculated back to the bottom of the fluidized with a cyclone for example, this is coined as fast fluidization. If particles being entrained are carried off, this now becomes pneumatic transport.

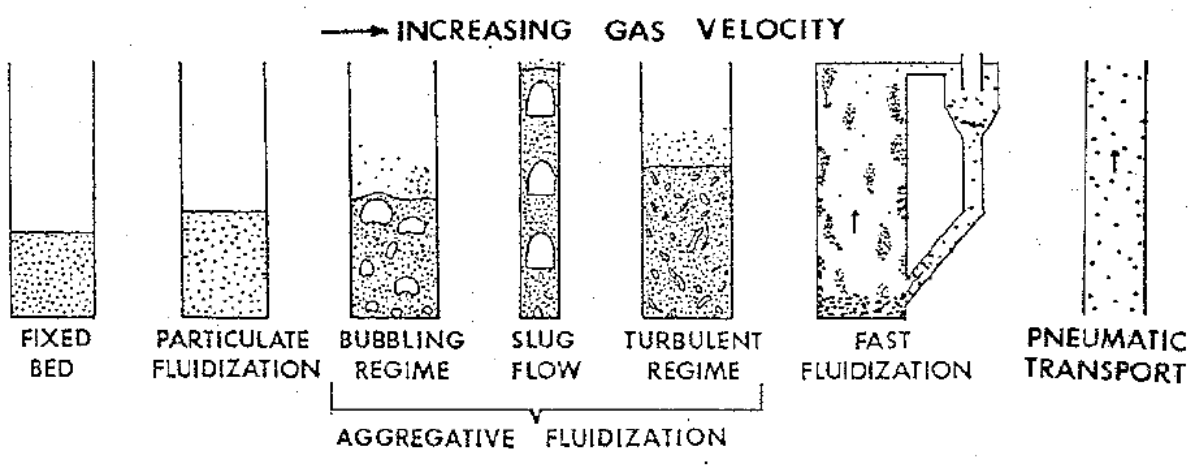

Figure 2.1. Fluidization flow regimes [25].

Another foundational pillar of fluidization was the work of Geldart in 1973 [26] who classified the various powders and particles being fluidized into four different functional groups based on shared fluidization properties. The four "Geldart" groups [26] are presented in Figure 2.2. They are based on the mean particle diameter (d_p) and relative density of the fluidization media (ρ_p-ρ_f). First, are the smallest "Cohesive" group C powders which are less commonly used due to the cohesive nature of these small light powders [25, 26, 27]. Fluidization is more difficult and less predictable due to strong inter-particle forces, and channeling of the gas occurs resulting in a poor fluidization quality [27]. Group A particles are called "Aeratable", as they experience a large bed expansion prior to the formation of gas bubbles [25, 27]. The gas backmixing is high [27], and these powders are typically used in catalytic reactions with a mean particle diameter of 30-100 μm [25, 26, 27]. Also common, are "Sand-Like" group B particles, which experience the bubbling

regime at the onset of fluidization [25, 26, 27]. The gas bubbles can grow to a large size and the particle diameters in this group are of a wider range from 100-1000 μm usually [27]. Similar to group B particles, are the larger and denser group D particles, which have more profound deviations from the group A particles in comparison [25, 27]. Like group B particles, they form gas bubbles at the onset of minimum fluidization, but the gas bubbles coalesce more rapidly, and commonly into slugs [25, 26, 27].

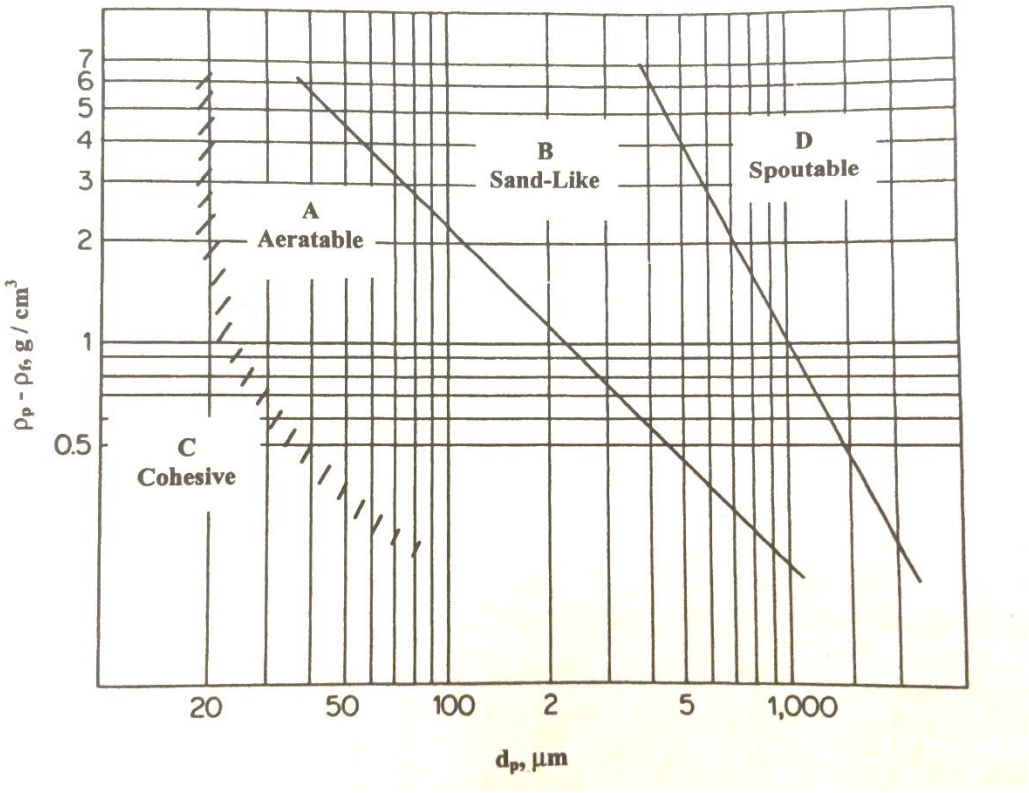

Figure 2.2. Geldart's classification of powders used in fluidization [26].

2.2. Entrainment/Elutriation Principles

Entrainment or elutriation of particles from a fluidized bed is a common phenomenon. Particle entrainment occurs when the gas velocity is greater than the particle terminal velocity in said gas. Elutriation occurs when only a given size range of particles is entrained from the bed rather than the entire particle size distribution. This occurs when the particles in the bed are non-uniform in size and mass. Particles with smaller diameters or which are less dense will have smaller terminal velocities. In contrast, particles with a greater diameter or greater density achieve their terminal velocity at greater speeds. Thus, if the gas velocity is found to be lower than the highest terminal velocity, particle elutriation will occur for the particles with a terminal velocity lower than said gas velocity. For the particles where this is not the case, they remain in the bed and are not entrained at the outlet of the fluidized bed.

The terminal velocity (U_t) as a function of the drag coefficient for a single spherical particle is given as [28, 29]:

$$U_t = \sqrt{\frac{4d_p(\rho_p - \rho_g)g}{3\rho_g C_D}} \quad \text{(eq. 2.1)}$$

d_p represents the particle diameter, ρ_p is the particle density, ρ_g is the particle density, g is standard gravity of Earth, and finally C_D is the drag coefficient. The drag coefficient C_D was correlated for various Re_p numbers in a table by Cliff et al. [30], but more recently Turton and Levenspiel [31] have proposed an equation applicable to the entire range of particle Reynold's number. The equation is as follows:

$$C_D = \frac{24}{Re_p}\left[1 + 0.173\left(Re_p\right)^{0.657}\right] + \frac{0.413}{1 + 16.300\left(Re_p\right)^{-1.09}} \qquad \text{(eq. 2.2)}$$

As mentioned, entrainment of particles is highly dependent on the gas velocity. Such that the *rate* of entrainment ($\dot{E}$, mass flow rate of particles being carried away from the fluidized bed at the freeboard outlet) is found to be a function of the gas velocity to the power of 4.0, and up to 7.0 [32, 33, 34]. Also, the gas pressure is of importance when discussing entrainment of particles. An increase in pressure will increase entrainment because the more dense gas will increase the drag force on the particles and therefore decrease the particle terminal velocity.

The entrainment of particles follows many mechanisms, of which they all begin by gas bubbles bursting at the bed surface thereby ejecting particles into the freeboard [35]. One proposed mechanism is ejection of particles from the roof of the bubbles reaching the surface of the bed [25]. However, it has been found that mostly fine particles in Geldart's group A particles are ejected this way [25]. The other mechanism is ejection from the wake of the rising bubble. As the bubble reaches the bed surface, the particles in its wake are propelled upwards and into the freeboard. Particle ejection from the wake can also occur for two coalescing bubbles at the surface [25]. Particles ejected by these last two mechanisms have nearly the same size distribution as the bed [25]. A visual representation of the proposed mechanisms for particle ejection is presented in Figure 2.3. Whether one mechanism dominates over the other is dependent on the particle size and the fluidization velocity [25].

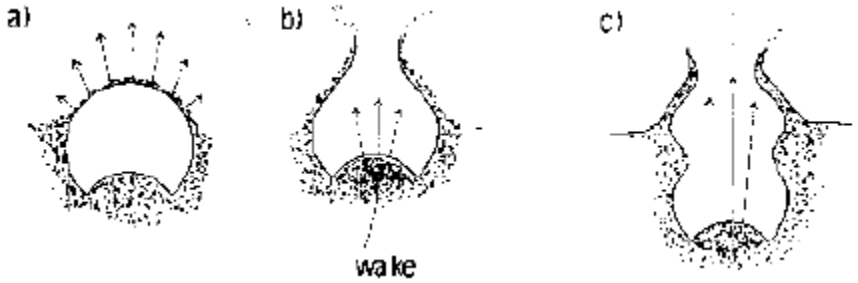

Figure 2.3. Bubbles bursting at the bed surface, which are ejecting solids into the freeboard (a) from the roof, (b) from the wake of a single bubble, and (c) from the wake of two coalescing bubbles. Taken from Handbook of Fluidization and Fluid-Particle Systems [25].

Fluidized beds operating with a large particle size distribution can exhibit forms of particle agglomeration. Agglomeration is common for fine particles <60 μm [36] where Van der Waal forces and other inter-particle cohesive forces are in greater effect [36, 37]. These fine particles tend not to agglomerate with each other but rather with larger particles. One study with fluid cracking catalyst (FCC) and a particle size range between 0 – 420 μm, found that particles up to 60 μm agglomerated the most forming larger clusters [36]. Most of the newly formed clusters were found in the range between 80-120 μm [36]. In the same study, a small fraction of particles between 140 and 190 μm were also found to agglomerate; combined with the fines agglomeration, it concluded that agglomerations reached a maximum size of 420 μm, equal to the upper bound of the original particle size distribution [36].

Agglomeration affects the entrainment of particles by increasing the particle size. Whereby a specific gas velocity would elutriate all particles below 60 μm, this is no longer the reality as many will agglomerate to form larger particles or cohesive clusters, and will then remain inside the dense bed rather than be carried off by the fluidization gas. Therefore, agglomeration has the potential to lower the rate of entrainment with a greater effect on fine particles. In an instance

where a fraction of the bed material is being elutriated, agglomeration will lower the rate of elutriation.

A critical diameter has also been found where the rate of entrainment no longer increases with decreasing particle size [38]. The critical diameter is found to be around 35-40 μm [37] but depends on the density of the solid material being fluidized. Below the critical diameter, particles are not entrained faster because inter-particle cohesion forces become very strong. Rather, under the critical diameter, the entrainment rate levels off [38]. Baeyens et al. offered a correlation to calculate the critical diameter ($d_{crit.}$) of a powder based on its density (ρ_p) [37].

$$d_{crit.} = 10325/{\rho_p}^{0.725} \qquad \text{(eq. 2.3)}$$

Where the critical diameter is in micrometers, and the density in kg/m^3.

The bed geometry influences the entrainment of particles as well. Depending on the bed diameter, wall effects may be present. For small columns with a diameter less than 0.10 m, wall effects are non-negligible [39]. For this reason, for smaller columns the gas velocity in the center of the fluidization column and in the freeboard is greater than the superficial gas velocity, resulting in greater entrainment rates [36]. However, for a bed diameter greater than 0.10 m, the entrainment does not vary significantly in the radial direction with maximum deviations of only 5% detected [39].

The other important geometry in a fluidized bed that effects the entrainment is the freeboard height. In a fluidized bed, the particle flux above the bed surface and into the freeboard is not constant. It is at a maximum near the bed surface and gradually diminishes up until it reaches a

steady value [36]. The height in the freeboard above the bed surface where the solid flux becomes constant is called the transport disengagement height (TDH). At this point, the solids are being conveyed by the gas and particles no longer interact with each other, rather they become part of the fluid. Since the solid flux reaches a minimum at the TDH, it is also here where the entrainment rate is at a minimum [25]. A higher freeboard than the TDH will not reduce the rate of entrainment, rather it will remain at the same minimum value. Alternatively, operating a fluidized bed with a freeboard height less than the TDH will increase the rate of entrainment. Further reductions in the freeboard height will only amplify the particle entrainment. In addition, the TDH is found to increase with superficial gas velocity [35].

2.3. Measurement Techniques for Entrainment Rate

Measuring the rate of entrainment is primarily based on measuring the mass of particles over time leaving the fluidized bed. Multiple studies have opted for batch tests [32, 37, 39, 40] where the column is loaded with the desired mass to entrain or elutriate. In the experiments where fine particles are being elutriated, their mass content is never greater than 10% [37, 39]. To begin a batch experiment, the gas velocity is increased to provide good mixing of the particles. However, the mixing stage is done quickly and not carried on for a long period of time to reduce the chances of entraining particles prior to the test run. Once the particles are sufficiently mixed, the gas velocity is suddenly increased to the desired superficial gas velocity and the measurement begins [36]. To capture the particles, a cyclone is often used [32, 36, 37, 38, 39, 40] as it provides high collection efficiency, good recovery of the particles, low attrition and low pressure drops at atmospheric conditions [41]. However, at high pressure, the pressure drop through the cyclone increases heavily [41] and filter bags may be opted for [41].

For continuous operation, there is a continuous recirculation of the solids captured by the cyclone back into the fluidized bed; usually by means of a dipleg [36, 38]. These are called circulating fluidized beds [25, 36, 38]. In order to take entrainment measurements, a sampling valve is usually attached below the bottom outlet of the cyclone [36]. In relation to the entrainment rate is the particle residence time in the fluidized bed as described in section 2.9, for that measurement typically tracers have been utilized [25, 42].

2.4. Effects of Pressure on Entrainment

The primary effect of pressure inside a fluidized bed is its effect on the gas density. From a modified form of the ideal gas law, it is clear that there is a proportional relationship between pressure and gas density as can be seen from equation 2.4.

$$\rho_g = \frac{P \cdot MW}{R \cdot T} \qquad (eq. 2.4)$$

Such that, under ideal conditions (low temperature and pressure) the gas density linearly increases with pressure. As a result, an increase in gas pressure will have a significant effect on the terminal velocity of particles inside the bed. Based on the terminal velocity equation 2.1, and assuming that the solid density is much greater than the gas density; the terminal velocity is then found to be proportional to the inverse square root of gas density. Meaning, an increase in the gas density by a factor of 4 would reduce the particle terminal velocity by a factor of 2, greatly augmenting the driving force for entrainment. However, the terminal velocity in equation 2.1 is also proportional to the inverse square root of the drag coefficient, which is also function of the gas density. Thus, the relationship between the terminal velocity and the gas density becomes non-

linear [30]. For a better understanding, the effect of pressure on the particle terminal velocity is described in terms of particle Reynolds number.

2.4.1. Effect of pressure on the particle terminal velocity

The first case to consider is with low particle Reynolds number, where $Re_p < 0.25$ [25, 29], also known as the Stokes regime. The particle Reynolds number is defined as follows:

$$Re_p = \frac{\rho_g . U_g . d_p}{\mu} \quad \text{(eq. 2.5)}$$

Where U_g is the superficial gas velocity and μ is the gas viscosity. In this laminar flow regime [25], the gas density is found to have no effect on the particles terminal velocity both theoretically and experimentally [29]. Beginning with the theory, by assuming a particle density much greater than the gas density, which is often the case by 2-4 orders of magnitude. The general formula for the terminal velocity of a single particle – equation 2.1 – can be rewritten as follows:

$$U_t = \sqrt{\frac{4 d_p \cdot \rho_p \cdot g}{3 \rho_g C_D}} \quad \text{(eq. 2.6)}$$

Upon which, the drag coefficient C_D in the Stokes regime is theoretically known and expressed as follows [29]:

$$\mathrm{C_D} = \frac{24}{Re_p} = \frac{24 \cdot \mu}{\rho_g \cdot d_p \cdot U_g} \propto \frac{1}{\rho_g} \quad \text{(eq. 2.7)}$$

Substituting equation 2.7 into equation 2.6, theoretically it stands that the terminal velocity of a particle is independent of gas density for low particle Reynolds number. Experimentally, Hoekstra and Sookai [29] conducted entrainment batch tests at atmospheric pressure using air and

helium as both gases share similar viscosities while air is 7 times denser than helium. This assured no confounding effects with the gas viscosity as it is an important parameter effecting entrainment in the laminar regime [35]. The particles used had a density of 2000 kg/m^3 and a Sauter mean diameter of 90 μm. In conclusion, the entrainment rate was found equal for both fluidization gases up to the maximum gas velocity test condition of 0.4 m/s. At a gas velocity of 0.4 m/s, the particle Reynolds numbers were 0.48 and 3.56 for helium and air, respectively [29]. Thus, it has been shown experimentally that entrainment can be independent of gas density for low particle Reynolds number. More so, the phenomenon is not restricted to Stokes regime of $Re_p < 0.25$ but was also apparent in the early transition regime up to values of $Re_p \sim 4$ [29].

For greater particle Reynolds number, the drag coefficient is no longer strictly inversely proportional to gas density, and the relationship between both becomes more complex as illustrated in Table 2.1. Subsequently, the gas density terms from equation 2.6 and 2.7 no longer eliminate each other.

Table 2.1. Recommended empirical drag coefficient correlations, $w = log_{10}(Re)_p$. Taken from Clift et al. [30]

Range	Correlation
(A) $\mathrm{Re} < 0.01$	$C_D = 3/16 + 24/\mathrm{Re}$
(B) $0.01 < \mathrm{Re} \leq 20$	$\log_{10}\left[\frac{C_D\,\mathrm{Re}}{24} - 1\right] = -0.881 + 0.82w - 0.05w^2$
	i.e., $C_D = \frac{24}{\mathrm{Re}}\left[1 + 0.1315\,\mathrm{Re}^{(0.82-0.05w)}\right]$
(C) $20 < \mathrm{Re} \leq 260$	$\log_{10}\left[\frac{C_D\,\mathrm{Re}}{24} - 1\right] = -0.7133 + 0.6305w$
	i.e., $C_D = \frac{24}{\mathrm{Re}}\left[1 + 0.1935\,\mathrm{Re}^{0.6305}\right]$
(D) $260 \leq \mathrm{Re} \leq 1500$	$\log_{10} C_D = 1.6435 - 1.1242w + 0.1558w^2$
(E) $1.5 \times 10^3 \leq \mathrm{Re} \leq 1.2 \times 10^4$	$\log_{10} C_D = -2.4571 + 2.5558w - 0.9295w^2 + 0.1049w^2$
(F) $1.2 \times 10^4 < \mathrm{Re} < 4.4 \times 10^4$	$\log_{10} C_D = -1.9181 + 0.6370w - 0.0636w^2$

For example, for group B and D particles, the particle terminal velocity is greatly reduced with pressure [25, 35]. In this instance, the particles terminal velocity is found to be proportional to the inverse square root of the gas density raised to a given power. The gas density power increases in a non-linear fashion as a function of the particle Reynolds number and would have a value of approximately 0.27 when $(Re)_p$ equals 260, and 0.39 when $(Re)_p$ equals 1500 [30].

2.4.2. Effect of pressure on the minimum fluidization velocity

The effect of pressure on the minimum fluidization velocity is similar to that of the particle terminal velocity since both measurements are an indicator of the velocity required for the force balance on the particles to reach a certain equilibrium. For instance, the minimum fluidization

velocity for small particles (Group A, low particle Reynolds number) is also independent of pressure [25, 35, 43]. Flow around those small particles of <100 μm, is laminar and so the fluid-particle interaction force is dominated by the gas viscosity which is essentially independent of pressure [35, 43].

For large particles of Group B and D, inertial forces dominate over the viscous forces. The inertial forces for large particles can be simplified to the following three: gravity, buoyancy and drag. When increasing pressure, the force associated to buoyancy and drag both increase while the one associated to gravity remains constant. As a result, the minimum fluidization velocity also decreases with increased pressure [25, 35]. The minimum fluidization velocity decreases sharply at first and begins to plateau past 2000 kPa. This is because the percent of increase in pressure for a given pressure increment is much less at high pressure than it is at low pressure.

2.4.3. Effect of pressure on gas bubble dynamics

Increasing pressure does have significant effects on the fluidization regime for all powders. Group A particles are the only to experience particulate fluidization (also called homogeneous fluidization) prior to the bubbling regime [31]. For these types of particles, an increase in pressure delays the bubbling regime [35]. This is such that a uniform expansion of the bed will occur over a larger range of gas velocities, and a larger range of bed voidages [35]. This is due to group A particles not having a reduced minimum fluidization velocity at high pressure [35, 43]. On the other hand, pressure increases the difficulty of bubbles to grow and form which increases the minimum bubbling velocity [35]. Therefore, the net effect of pressure is an increase in the duration of particulate fluidization, enabling smoother behavior at elevated pressures [35, 43].

In addition, bubble break up was found to increase with pressure for group A particles. The theory developed by Upson and Pyle (1973) and Clift et al. (1974) suggests this is due to the instability in the bubble roof and that particles rain down upon it [44, 45]. The bubble stability decreases because the emulsion phase viscosity decreases due to an increased bed voidage with pressure. King and Harrison (1980) performed experimental tests up to 2500 kPa with X-ray imaging and concluded that for all types of Group A particles, bubble break up occurred from particles falling in from the bubble roof [46]. The effect was found to be more pronounced at elevated pressures which also leads to smaller bubble size.

As for Group B particles, Hoffman and Yates (1986) found the bubble size to increase slightly with a maximum bubble size between 500-2000 kPa depending on the excess gas velocity used [43]. The excess gas velocity is defined as U_g - U_{mf}, and represents the additional gas velocity above the minimum fluidization velocity. It is a better parameter to hold constant for comparing the effects of pressure than U_g/U_{mf}; simply because it approaches more the actual independent variable U_g than the former. At constant U_g/U_{mf} the gas velocity would always be much greater at lower pressures due to its increased value of U_{mf}, and therefore would not provide a fair basis for comparison. With that said, passed 2000 kPa, the bubble diameter was found to decrease with pressure at constant excess gas velocity [43]. Initially, as bubbles grow their rise velocity decreases, on the other hand, at high pressure when bubbles become smaller their rise velocity increases [35]. Olowson and Almstedt (1990) corroborated the results from Hoffman and Yates and found the mean bubble frequency, mean bubble rise velocity, mean bubble volume fraction and visible bubble flow to increase with increasing pressure and excess gas velocity [47]. Other

findings include a decrease in the mean pierce length of bubbles with pressure after an initial increase. This also suggests a maximum bubble size occurring between 500-2000 kPa [47].

At high pressures up to 2000 kPa, the uniformity of bubbles in the radial direction is found to be reduced [43]. As a result, it is suggested that bubbles are more concentrated in the center of the bed [43] which leads to higher local gas velocities in comparison to the actual superficial gas velocity passing through the bed. Undoubtedly, this would increase local entrainment as the driving force for it is increased locally. This may result in greater entrainment rates than originally expected, especially if operating in a dual-particle system with fines in addition to Group B particles. The smaller bubbles produced at high pressure can also be the cause for increased entrainment rate of fine particles. This was confirmed by Pemberton and Davidson (1986) for the case of fines ejection within a Group A & B mixture [25].

2.5. Bubble Dynamics Measurement Techniques

Bubble dynamics are an important measure used to characterize the hydrodynamics of gas-solid fluidized beds. More importantly, bubbles have a profound effect on entrainment [25], thus it is imperative to have information regarding the in-bed bubble dynamics. They are often characterized by analyzing the time-series of in-bed pressure measurements in the fluidized bed. An in depth review paper on in-bed pressure measurements by van Ommen et al., was conducted in 2011 [48] and forms the basis of this literature review section. The type of equipment used, analysis in the time domain and frequency domain are presented [48].

2.5.1. Measurement techniques

Measurement techniques employed for bubble dynamic measurements including bubble size, rise velocity and frequency can be divided into two categories: intrusive methods including fiber optic and capacitance probes [48]; and non-intrusive techniques including visual observation, pressure signal analysis and X-ray and capacitance tomography [48]. Visual observations are primarily used in gas-liquid beds or 2-D gas-solid beds with transparent column walls. X-ray photography can be applied in 3-D gas-solid beds but the fluidization column has to have a relatively thin or transparent column wall in order to detect the bubble movement inside, and thus cannot be applied in large industrial units [48].

Differential pressure drop signal analysis is amongst the most economical and robust non-intrusive method used avoiding any distortions in the flow behavior [48, 49]. Secondly, measuring pressure is relatively easy, even under harsh, industrial conditions such as high pressure and temperature [48]. The biggest disadvantage of using such method is the interpretation of the signal

obtained which can be difficult. However, extensive work has been carried on the issue, with literature presenting conclusive corroborated results and analyses [48, 49].

2.5.2. Time domain

Analysis in the time domain is often the simplest approach, and can be used for most fluidized bed systems, as the dominant frequencies typically range from 1-5 Hz [48]. The most common approach involves using the standard deviation of the differential pressure signal which is a measure of the signals amplitude. As a result, it is often used to determine a regime change. Whether it be the minimum fluidization, or the transition velocity from bubbling to slugging to turbulent fluidization [48].

Another critical piece of information that can be extracted from the standard deviation of the differential pressure signal is the average bubble size. Liu et al. (2010) [49, 50] proposed a correlation (equation 2.8) for estimating the average bubble size in a gas-solid fluidized bed via the standard deviation of a differential pressure signal across two ports vertically separated by a distance greater than half the maximum bubble diameter.

$$d_{B,\Delta P} \propto \frac{\sigma_{\Delta P}}{\rho_p g\left(1-\varepsilon_{mf}\right)} \qquad \text{(eq. 2.8)}$$

The estimated average bubble size using pressure drop measurements ($d_{B,\Delta P}$) is calculated with the standard deviation of the differential pressure fluctuations ($\sigma_{\Delta P}$), particle density and voidage at minimum fluidization. The equation requires a proportionality constant, for which the authors used a value of 1 [49]. Worth noting, the estimated bubble size using equation 2.8 is only applicable to the region between the two vertical pressure ports. As a result, comparisons of bubble

size at different operating conditions must be done at the same elevation and over the same vertical distance because bubbles grow as they rise through the fluidized bed. The disadvantage of using the standard deviation of the pressure signal for the respective analysis methods is that all the information on the time scale is lost e.g. signal consistency and reproducibility.

Another method proposed in the time domain to analyze bubble dynamics is the probability density function of pressure increments. Pioneered by Gheorghiu et al. (2003) [48], the proposed statistical analysis uses pressure increments defined as follows:

$$\Delta P = P(t + \Delta t) - P(t) \qquad \text{(eq 2.9)}$$

The pressure increments are taken over a variable time delay Δt where $P(t)$ denotes the value for pressure at time t. The method is inspired from turbulence research and the advantage with this method is the conservation of the time scale and dynamics of pressure. Generally, it seems to be a promising method, but further research is needed to see if this method has significant added value [48].

In addition, looking at the average cycle time, which is determined by how many times the signal crosses the average value in a given time stamp can provide qualitative information [48, 51]. For instance, a single bubble of constant size periodically bursting at the bed surface is represented by a singular sine wave for the differential pressure signal over time. Such that the magnitude of the sine wave for the differential pressure signal over time provides qualitative information on the bubble sizes. Large deviations from the average differential pressure as seen by the large sine peaks on the time scale represent larger bubbles. Similarly, a qualitative bubble frequency can be obtained (average period of sine wave). Also, depending on the clarity of the

sine wave, and or the presence of other sine waves at different frequencies, it can be an indicator of the bubble distribution within the fluidized bed. For instance, if a clear, singular sine wave is observed, it represents only one single mechanical oscillator present [48] and therefore a relatively narrow bubble size distribution; a range of different bubble sizes would produce multiple sine waves in parallel occurring at different frequencies. In the example shown in Figure 2, the bubble size appears to be singular with an approximate bubble frequency of 1.0 Hz.

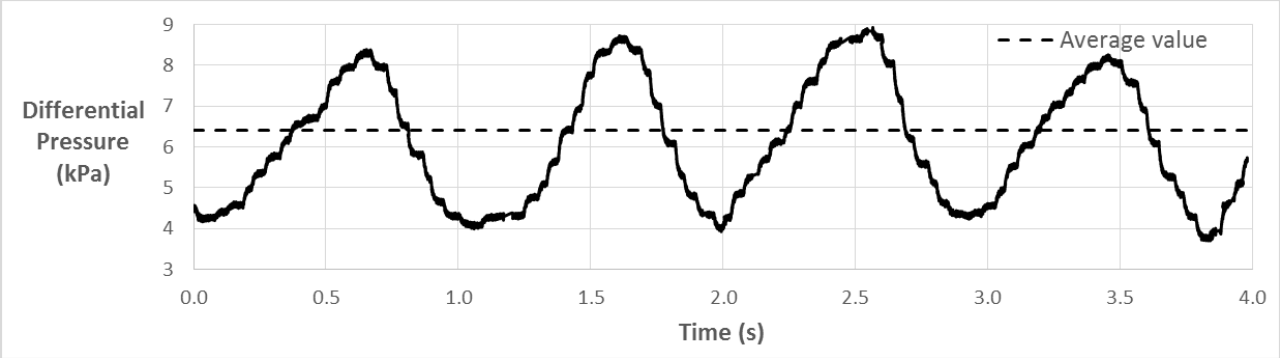

Figure 2.4. Example of a differential pressure time series.

The average cycle time can also be used as an indicator of regime change. The reason being, that the average cycle time was found to decrease for all regimes until transport conditions were reached.

The last method of analysis explored in the time domain were the autoregressive models (AR). They are most useful when long data records are not available or when the quality of the recorded signal is poor [48]. It breaks down the fluidized bed dynamics as a set of well-defined mechanical systems. The system is described by a lower order model if the low frequencies are dominating the system. Which means the differential pressure series is oscillating slowly. Contrary, if a higher order model is obtained, it implies the series is oscillating rapidly and that the

pressure signal is of fairly stochastic nature (random but with statistically significant trends; difficult to calculate precisely at a given time).

In summary, both the standard deviation of the differential pressure signal and its time series are the most easy and readily available method to determine bubble dynamics in the time domain.

2.5.3. Frequency domain

Analysis in the frequency domain is mostly limited to the use of the power spectrum aimed at determining the dominant frequencies in the time domain [48, 51]. Later associating those with physical properties of the system e.g. bubble frequency and bubble rise velocity. It is used when there is a distribution of bubble sizes, as the power spectrum yields a probability density function of all the relevant frequencies (each associated to a different bubble size). In turn, an approximation of the bubble size power spectrum can be obtained. A sample frequency of 20 Hz is assumed satisfactory for most bubble dynamics in the fluidized bed [48]. Finally, if the data record was taken short or is of poor quality, once more autoregressive models can be used to generate and estimate the power spectrum [48].

2.6. Effect of Horizontal Tube Bank on Bed Hydrodynamics

The presence of reactor internals such as horizontal tubes can play a significant role on the gas flow within a fluidized bed and similarly on its hydrodynamics [25, 52]. Specifically, a horizontal tube bank whether inline or staggered is found to increase the local gas velocity at certain points in the bed, e.g. between horizontal tubes, and more importantly to promoted gas bubble break up [52, 53, 54, 55] pending the tube packing is dense enough [52, 54, 55]. Promotion of bubble break up is desired when dealing with large bubbles or slugs in gas-solid reactions. Smaller, more frequent bubbles have a greater collective surface area which enhances the gas-solid contacting and mass transfer from one phase to the other [25, 52]. If the presence of tubes is minimal, either by having very few tubes present or by having very large horizontal and vertical tube pitches, the fluidized bed will behave similar to that of a freely bubbling bed, i.e. no tubes present [52, 53, 54, 55]. Although much work is reported for fluidized bed with internals, there are very few articles discussing the effect of a tube bank on entrainment and its impact on the residence time of elutriating particles [56]. Rather, most of the work reported in the literature has focused on the hydrodynamics within the bed [52, 54, 55]. This information is still crucial as the hydrodynamics of the fluidized bed are known to impact the entrainment and residence time of fines.

2.6.1. Effect of tube bank on gas bubble break up

One of the first phenomena investigated and reported in literature is the effect of horizontal tubes on bubble break up. At first, a simplistic approach was taken by Yates and Ruiz-Martinez (1987) which looked at injecting individual gas bubbles in an atmospheric fluidized bed operating at minimum fluidization. Using X-ray imaging they were able to capture and record the bubble

break up that would ensue [52]. The fluidized bed was rectangular (0.185 m by 0.36 m), with a static bed height of 0.50 m. Two sizes of tubes were used: 10 and 20 mm. The bed material was an alumina powder with a mean particle diameter of 290 μm. The particle density was not specified but lesser than glass beads (2500 kg/m^3) [52, 57]. In this case, the bed material approaches Geldart group A particles. Also, the tube bank geometry was varied multiple times throughout the same study, with 1, 2 or 3 rows of horizontal tubes present. The first experiments occurred with only 1 row of horizontal tubes and are described below.

The parent and single bubble being injected in the fluidized bed was kept constant at 45 mm in diameter. With that said, little effect regarding bubble break up was observed if the horizontal spacing between tubes exceeded the mother bubble diameter of 45 mm. If the bubble hit the horizontal tube directly at its bottom center, it rarely resulted in bubble splitting with the small tube size and instead the gas split and flowed around the tube passing by unhindered. As the horizontal spacing between tubes was reduced bubble splitting started to occur with the 10 mm tubes.

The authors conducted the same experiment with 20 mm tubes, and upon direct contact bubbles would always break up with the larger tubes. Similarly, reducing the horizontal pitch increased bubble splitting even more so than for the smaller 10 mm tubes. The mechanism for splitting was thought to lie in the attraction of the bubbles to the tube surface such that if a bubble passes in a narrow channel between two tubes it can divide on both sides due to the attraction [52]. Furthermore, the authors suggested that bubbles are generally attracted towards the surface of the tubes such that a larger amount of surface area with larger tubes, or more dense packing causes

greater disturbances in the gas flow, e.g. bubble break up [52]. As a result, Yate and Ruiz-Martinez concluded that keeping the ratio of tube diameter to bubble diameter high and the horizontal tube pitch low were important factors controlling bubble break up.

These results were observed for a single row of tubes present, as such the authors then conducted experiments using 2 and 3 rows of tubes in a triangular pitch formation (staggered). Adding a second row of tubes increased the bubble break up for both cases of tube diameter pending the vertical pitch was of a sufficient distance. If the vertical separation between the two rows of horizontal tubes was too short, the bubbles were found to bridge the gap and only split among the second row of tubes. Later, with the 10 mm tubes, experiments with 3 rows of tubes were conducted of which the main findings were a continuous and complete cycle of splitting and coalescence for the bubbles. The bubbles would split upon hitting their first row of tubes but would then re-coalesce at the next row of tubes. This effectively impeded the bubbles from growing larger than their original size prior to contact with the tubes. This confirms the belief from other authors that tube banks can be used to effectively control and reduce the bubble size in a freely bubbling bed [25, 52, 53].

Yates and Ruiz-Martinez also looked at the gas balance before and after bubble break up and what was found is that during break up, the combined volume of the daughter bubbles is always lower than the mother bubble [52]. The missing gas is anticipated to have leaked in the emulsion phase of the bed causing an increase in the local voidage [52]. More so, if the bubble splits in more than 2 daughter bubbles, the leakage of gas to the emulsion phase is expected to be even greater. Such that bubble break up increases the overall voidage and better distributes the gas throughout

the fluidized bed, effectively increasing the gas-solid contact in the bed [52]. This is key for many processes, including coal combustion.

In continuation with their work, Yates and Ruiz-Martinez (1990) did experiments with the same fluidization apparatus except now the tube bank contained 4 staggered rows and the natural bubbling bed was used to originate the mother bubbles such that the fluidization velocity was varied from 2 to 3 U_g/U_{mf}. It was found that bubble flow after passing a row of tubes is mostly concentrated in said channel, with minimal flow touching the top of the tubes [53]. As with the past study, the gas velocity in between the tubes was found to be much greater than the overall superficial gas velocity. According to Yates and Ruiz-Martinez, this increases the amount of bubble-bubble interaction and potential coalescence at said location. Such that, there is a limit to the minimum bubble size that can be achieved with the presence of a tube bank as was found in their original study [52, 53]. This is dependent on gas flow conditions and tube bank geometry [53].

2.6.2. Effect of tube bank on pressurized fluidized bed hydrodynamics

Olsson, Wiman and Almstedt [54] took an in depth look at the hydrodynamics inside a fluidized bed with a tube bank present. It included the effect of pressure with operating pressures varying from 100 to 1600 kPa. The work is presented in two studies [54, 55], the first looked at the effect of 3 relatively sparse tube banks on the bed hydrodynamics in comparison to that of a freely bubbling bed which was studied in the past for the same fluidization apparatus [58]. The second study by Wiman and Almstedt [55] conducted experiments with a denser tube bank as it was believed to increase the onset of turbulent fluidization, which was not adequately observed in

the past study [54, 55]. Both studies were directly conducted to enhance the interpretation and operation of pressurized fluidized bed combustors [54, 55]. The bed material was silica sand with a mean diameter of 0.7 mm and a fairly wide size distribution, the particle density was 2600 kg/m^3 with a shape factor of 0.8. The fluidized bed had a rectangular cross-section of 0.2 m by 0.3 m and the authors used a minimum fluidization height of 0.86 m. Experiments were conducted for two excess gas velocities; U_g - U_{mf} = 0.2 m/s and 0.6 m/s which corresponds to values of 2-4 times U_g/U_{mf} for the corresponding pressure range. The 3 tube configurations used in the first study are presented in Figure 2.5.

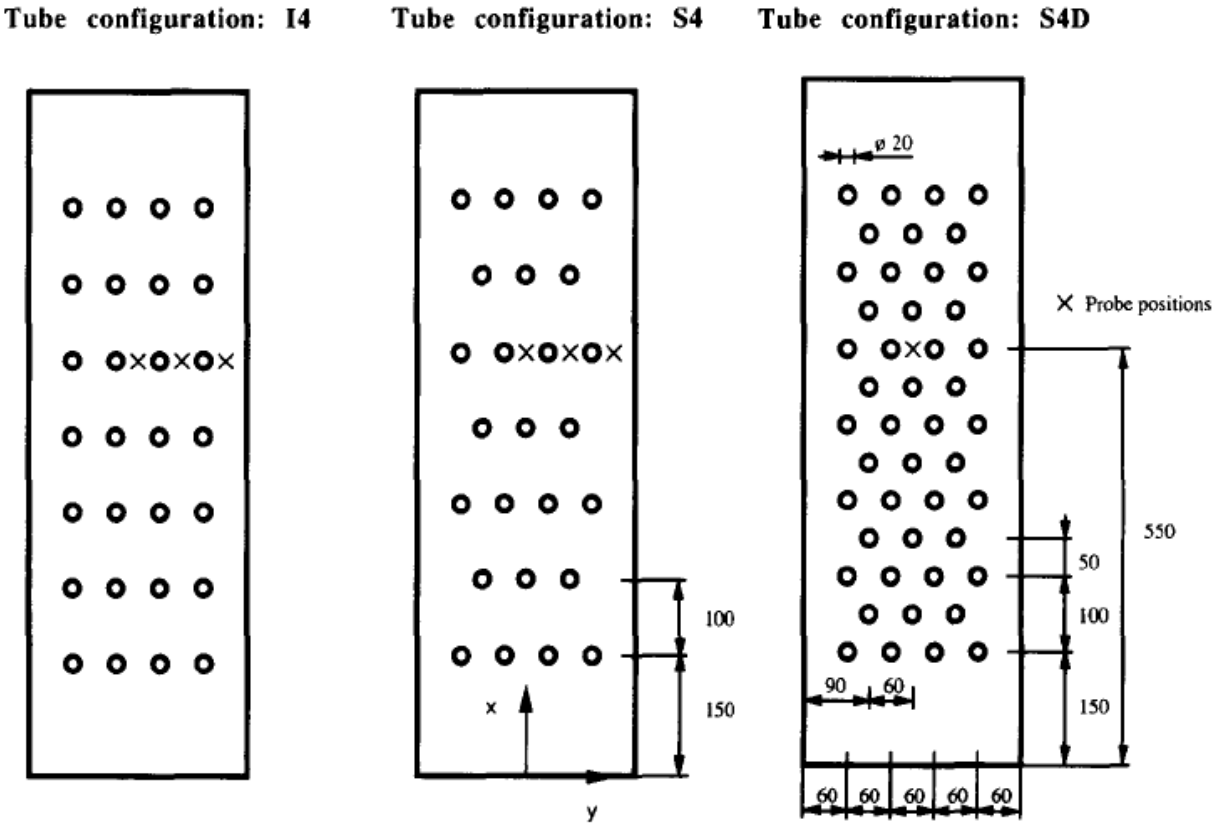

Figure 2.5. Tube configurations and probe positions in work by Olsson et al. The tubes were made of aluminum and had a diameter of 20 mm. Dimensions are reported in millimeters [54].

As can be seen from Figure 2.5, tube banks I4 and S4 were quite similar except the tubes in S4 are in a staggered arrangement, while the tubes in I4 were all inline. Meanwhile, the tube bank S4D had the same horizontal pitch as S4 except double the amount of tubes in the vertical axis. Such that S4D had the densest tube packing and therefore should have the results which differ the most from the freely bubbling bed [54, 58]. For greater clarity, it is worth noting the tubes were parallel to the 0.2 m dimension of the bed (and therefore 0.2 m in length). In their work, Olsson et al [54] measured the hydrodynamic parameters approximately at 2/3 of the tube bank height as seen in Figure 2.5 by the "X" marker. Therefore, it is important to remember their results hold true for such elevation, upon which the bubble regime was fairly established. The following hydrodynamic parameters of interest were investigated: bed expansion, mean pierced length of bubbles (statistically related to bubble size), mean bubble frequency and proportion of the local bubble volume fraction in the radial direction.

Starting with the bed expansion, it was found to increase with gas velocity and pressure. They observed that at low gas velocity, with and without a tube bank present, the increase in bed expansion is modest passed a pressure of 400 kPa. However, with the tube banks present and at high gas velocity, the bed expansion continued to increase up to its maximum tested pressure of 1600 kPa [54]. All three tube banks had a similar bed expansions at 1600 kPa, which suggests that tube banks do enhance bubble break up and as a result increase the bed voidage well passed what is measured in a free bubbling bed [54]. Therefore, it seems the vertical pitch (comparing tube banks S4 and S4D) does not have a profound impact on the bed expansion, or at least within the margin that was tested.

The next parameter investigated by Olsson et al. was the mean pierce length of the bubbles [54]. At the highest excess gas velocity, with and without a tube bank, a maximum pierce length was attained at 200 kPa, upon which the dense staggered tube bank (S4D) had the largest mean pierce length of bubbles as shown in Figure 2.6. The pierce length was reported greater in a staggered arrangement because bubbles elongated themselves as they bridged from one row to the other [54]. For all bed geometries, the mean pierce length of bubbles was found to lose stability at high pressure because passed their maxima at 200 kPa, the mean pierced length of bubbles continuously decreased. In addition, at the lower excess gas velocity of 0.2 m/s, the elongated bubbles present in the tube bank held their stability and growth to a greater pressure of 400 kPa. Such that, increased gas velocity and increased pressure reduces the bubble stability and bubble size with a tube bank present.

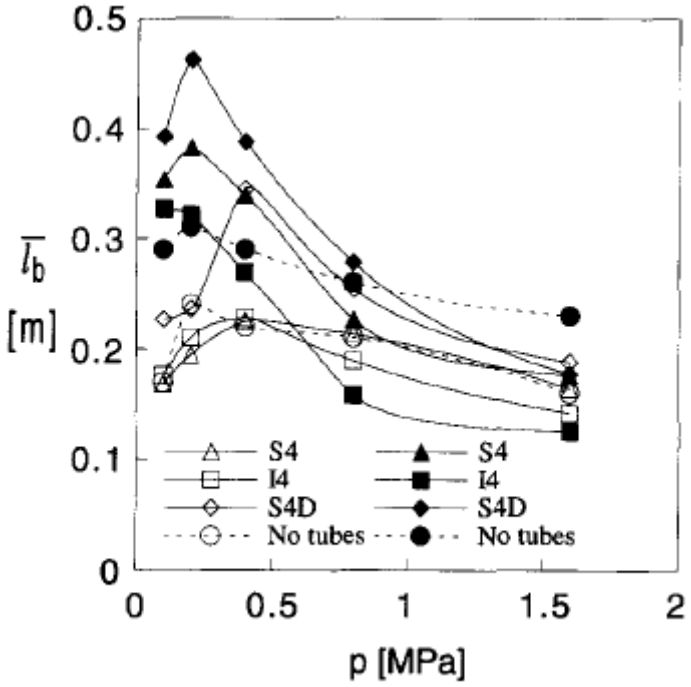

Figure 2.6. Variation of the mean pierce length of bubbles ($\bar{l}_b$) in the centre of the bed cross-section with excess gas velocity, pressure and tube geometry. Unfilled markers are for U_g - U_{mf} = 0.2 m/s; filled markers are for U_g - U_{mf} = 0.6 m/s. The results without tubes were obtained in the same bed by Olowson and Almstedt (1990). Taken from Olsson et al. [54].

Following the bubble frequency as a function of tube bank, pressure and excess gas velocity was reported. The bubble frequency increased to a greater value when the tube bank was present, and the trend was more pronounced at higher gas velocities and elevated pressure where increased bubble break up was found [54].

Equally interesting are the results of the local visible bubble flow rate measured as a function of its horizontal positioning between the tubes. As seen in Figure 2.5, the staggered tube bank S4 had 3 local measurements on the horizontal axis demonstrated by the three "X" markers and it was the tube bank chosen for the study. At atmospheric pressure and at low gas velocity, the visible bubble flow rate was fairly constant at the 3 horizontal positions of the measure. Upon

increasing the gas velocity, there was a substantial difference in the bubble flow rate at the center compared to the measure nearest to the wall. At higher gas velocities, the visible bubble flow rate heavily prefers flowing through the middle of the column decreasing gas-solid contacting [54]. The same was found for elevated pressures, with the visible bubble flow rate through the center being greatest at 400 kPa. Afterwards, there was better gas distribution in the radial direction with increased pressure but the visible bubble flow rate still favored the center of the column up to 1600 kPa [54].

In summary, it was found that the tube bank heavily influences the fluidization behaviour, beginning with an elongation of bubbles at low pressures, transitioning to substantial bubble break up at higher pressures, which leads to dispersed bubbling and potentially a turbulent behavior inside the tube bank [54]. Although, for these particular tube bank configurations, the density of packing was not sufficient enough to observe the turbulent behavior [54]. Nonetheless, Olsson et al. concluded that the transition to turbulent behavior is expected to be facilitated by the presence of a tube bank.

2.6.3. Faster transition to turbulent fluidization

In response, Wiman and Almstedt [55] continued their work by conducting the same experiments except with a denser tube bank inside the fluidization column. The amount of tubes per staggered row increased from 3 and 4 tubes (S4D), to 6 and 7 tubes per row (S6D, see Figure 2.7); practically double the amount of tubes in the horizontal axis. In addition, the bed hydrodynamics were examined for an additional bed material of mean particle size 0.45 mm; again sand with a density of 2600 kg/m^3 was used. The authors remained with the same fluidization

apparatus. For this new study, the new denser tube bank (S6D) was used in conjunction with the previously most dense tube bank, S4D. The following Figure 2.7 illustrates the two tube banks used.

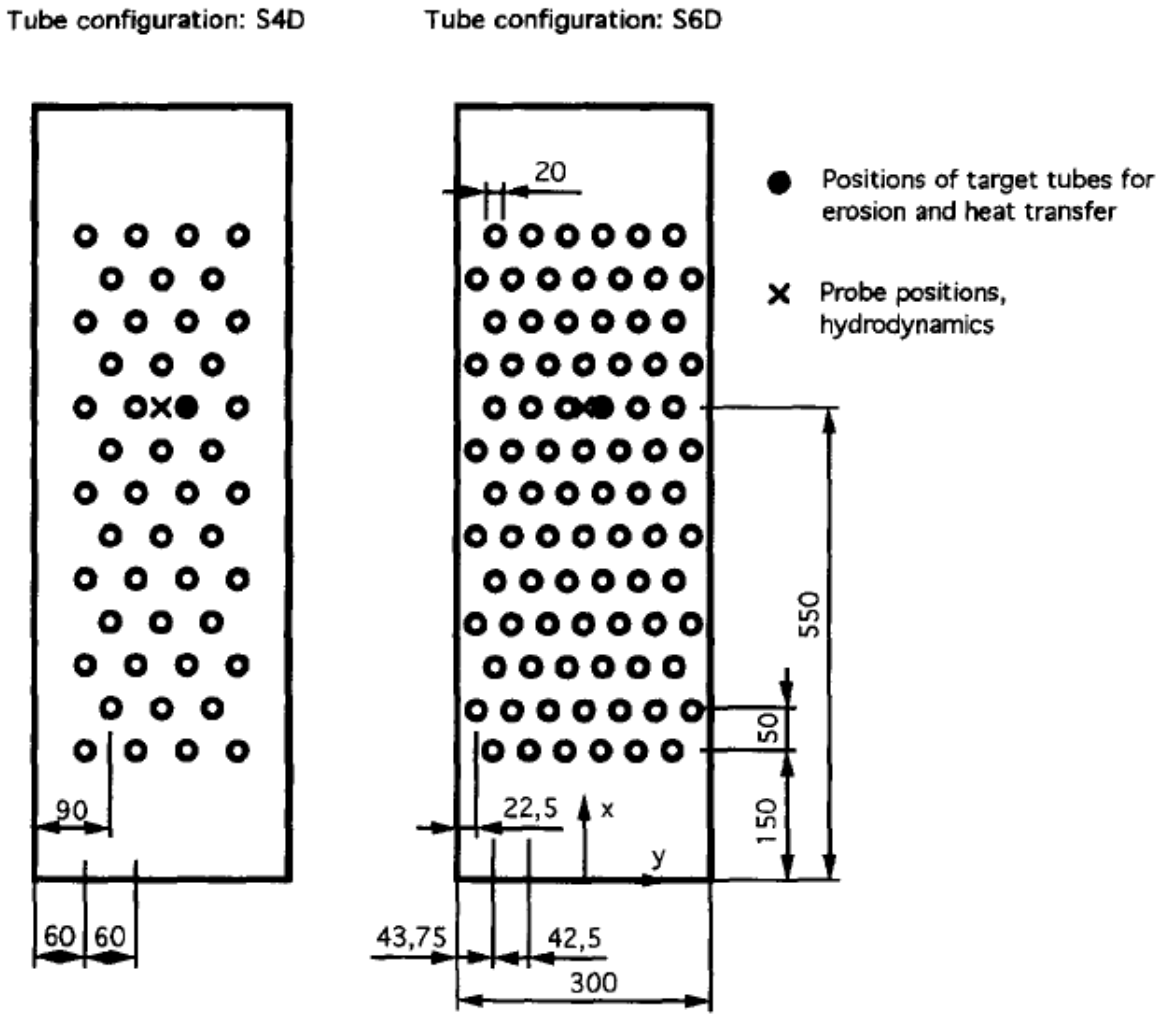

Figure 2.7. Tube configurations and target tube positions taken from Wiman et al [55]. The probe positions used for the hydrodynamic measurements are also shown. All dimensions are in millimeters.

Tube bank S6D had a much greater packing density in the horizontal axis and therefore it was anticipated to see turbulent behavior at high pressure and high excess gas velocity; despite the

excess gas velocities being modest at 0.2 and 0.6 m/s [55]. Turbulent behavior is defined as a more evenly distributed flow pattern over the bed cross-section with no distinct bubble pattern existing.

General results from Wiman et al. were that for both particle sizes (0.45 and 0.70 mm), the hydrodynamic results were similar for a given combination of pressure and excess gas velocity [55]. The dense tube bank S6D caused greater bed expansion and voidage inside the fluidized bed. It was indicated that for most pressures, tube bank S6D had better radial distribution of the gas [5]. In addition, less of the visible bubble flow rate was concentrated in the center channel. Finally, it was also found that the denser tube bank S6D gave way to a faster transition to turbulent fluidization. This is in accordance with their past work presented by Olsson et al. [54] and of other authors, notably that of Löfstrand et al. [59] who also found that the horizontal tube pitch is more crucial than the vertical pitch when it comes to fastening the transition to a turbulent regime.

2.6.4. Simulation studies

To conclude the literature review on the effect of tube bank, the results from two simulation papers were examined. The first study was conducted by Rong and Horio [60], they were also interested in the hydrodynamics concerning pressurized fluidized bed combustion (PFBC). The pressures investigated were 100, 500 and 1200 kPa respectively at an elevated temperature of 850°C [60]. The bed material was taken to be spherical, with a diameter of 1 mm and a density of 2650 kg/m^3. The gas used was that of air while taking into account the change in gas density with increased temperature. The fluidized bed was simulated in 2D with a height of 0.99 m and width of 0.33 m. The method of simulation was the discrete element method (DEM), of which the authors suggest DEM simulation to be well representative of the reality [60]. The only shortcoming

compared to PFBC processes was the range of velocities investigated, only one was selected, of which they kept U_g/U_{mf} constant at a value of 1.5.

The simulation was run for 4.64 s of which the last 3.00 s was used for the time averaged results [60]. The tube bank used was of dense packing, slightly more so than the past work of Wiman et al. [55] with tube bank S6D. The tube horizontal and vertical pitch were taken at an equal, but lesser value of 2 compared to 2.1 for S6D used by Wiman et al. [55, 60]. The tube diameter was 30 mm (horizontal tube pitch is 60 mm), and the tube bank itself was composed of 5 staggered rows of tubes; with 4 to 5 tubes per row. On a last note, the center of the first row of tubes was 0.24 m above the distributor plate.

First and foremost, it was found that the existence of tubes in a staggered arrangement enhanced the bubble splitting which is consistent with past authors [25, 52, 54, 55, 60]. It was also found that the bubble size decreased with pressure, while the bubble frequency increased. In addition, the simulation calculated time averaged values for the bed voidage and found that in the tube bank region the voidage was greater than that of the wall. Typical voidages, irrespective of pressure, ranged from 0.5 to 0.6 within the tube bank to lower values of 0.4 to 0.5 for the voidage nearest to the vertical wall. The bubble volume fraction was also found to continuously increase with pressure, which is consistent with past work for dense tube banks [54, 55].

The next simulation was 2D as well, using Eulerian-Eulerian two-phase models and conducted at atmospheric pressure [61]. Concerning the effect of tube bank, the study only looked at the effect of having only one row of horizontal tubes. Results were presented for a horizontal row having 1, 3 and 4 tubes respectively. The gas velocity U_g, was equal to 2.25 U_{mf} and the bed

material was selected to be 1 mm in size with a density of 1600 kg/m^3. The bed width was taken to be 0.315 m with a tube diameter of 51 mm.

With only one tube along the center line, as seen in Figure 2.8, most gas bubbles steer clear of the immersed tube, and their shape was elongated – the blue coloring represented areas of increasingly high gas voidage (e.g. gas bubbles) and yellow to red colors were areas of high particle density. The average visual bubble size was found to be smaller suggesting increased bubble break up despite the presence of only one tube. Finally, the simulation showed that as gas bubbles passed by, they were not found to completely encase the tube as the tube diameter was sufficiently large at 51 mm.

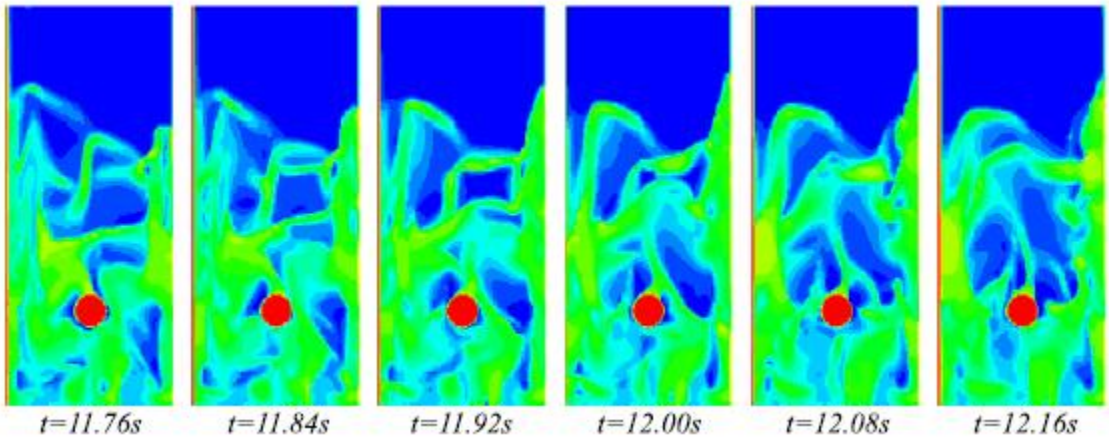

Figure 2.8. Instantaneous particle concentration distributions with one immersed tube at the superficial gas velocity of 1.2 m/s. Taken from Yurong et al. [61].

With 3 tubes present in the single, horizontal tube row, the shape of the gas bubbles became more elongated when compared to 1 tube present as seen in Figure 2.9. The gas bubbles had a greater difficulty rising through the bed due to the obstructive nature of tubes. For which, the 3 tube row at its center approximately occupied half of the cross sectional area of the free bed. As the gas bubbles rose and reached the tube surface, they were seen to accumulate on the foreside of

the tubes as large pockets of gas until all of the gas had penetrated through the reduced channel between tubes.

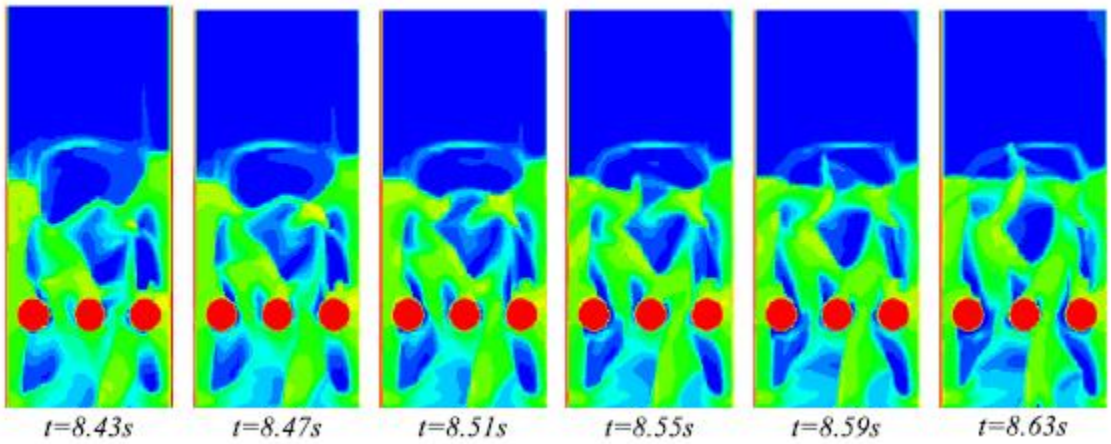

Figure 2.9. Instantaneous particle concentration distributions with three immersed tube at the superficial gas velocity of 1.2 m/s. Taken from Yurong et al. [61].

Lastly, the influence of having 4 tubes was examined and the results were similar but more pronounced than those obtained with 3 tubes. The results of the simulation with 4 tubes are shown in Figure 2.10. Once more, there was a large accumulation of gas on the foreside of tubes as the bubble made its way across the horizontal row of tubes. Bubbles were found to elongate even more, and at this point there was also jetting between the immersed tubes; at the limit the tube bank will begin to act as a perforated distributor.

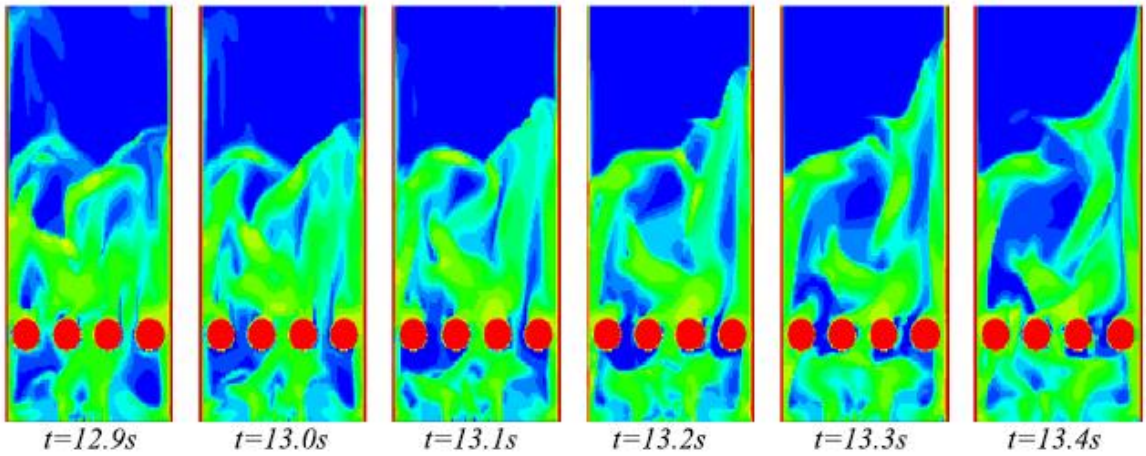

Figure 2.10. Instantaneous particle concentration distributions with four immersed tubes at the superficial gas velocity of 1.2 m/s. Taken from Yurong et al. [61].

From the particle velocity distributions, it was clear that an increase in the amount of tubes increased the amount of particle-wall interactions [61]. The back mixing of particles also became more chaotic. Furthermore, the bubble frequency was found to increase with the amount of tubes present, with a bubble frequency twice that of the free bed for 4 tubes present (from 1.0 Hz to 2.2 Hz). This suggested bubble break up when tubes were immersed in the fluidized bed. As a final point, the bed experienced a larger expansion with more tubes present.

2.7. Particle Velocity

The particle velocity of powders is an important parameter in regards to entrainment. It provides an estimate of the available driving force to carry out fines from the fluidized bed. Although its use may be limited as fines may be interfered and unable to flow in a rectilinear direction within a fluidized bed of larger particles not susceptible to entrainment. The particle velocity is defined as follows:

$$U_p = \frac{U_g}{\varepsilon} - U_{slip} \qquad (\text{eq. } 2.10)$$

Where U_p is the particle velocity and U_{slip} being the particle slip velocity (slip velocity for short). Studies of the fast fluidization regime were undertaken by Yerushalmi and Cankurt [62]. The particle velocity at pneumatic transport conditions was explored for several Geldart group A particles as well as for Geldart group B sand particles having a size range of 80-670 μm. The group A particles of interest with experimental trials on its particle velocity was fluid cracking catalyst (FCC) of size range 0-130 um, and density of 1070 kg/m^3. The particle velocity was investigated at atmospheric pressure in a 0.15 m I.D. fluidized bed. For large coarse particles, the particle velocity upon which pneumatic conveying is initialized lies close to the terminal velocity of the median particle size [62]. Similarly results were obtained for group A particles [62]. They also found for vertical dilute flow of group A particles, the particles are conveyed in a relatively straight path [62].

Also it was demonstrated by Yerushalmi and Cankurt that group A particles are sensitive to clustering in the fluidized bed and in the freeboard [62]. As a result, the particle velocity takes

the behavior of the cluster [62], this would increase the slip velocity of an individual particle even more. The observation of clustering for fine particles was also observed by Kunii and Levenspiel [63].

Li and Tomita [64] conducted experiments investigating the particle velocity and concentration in a horizontal dilute flow for pneumatic conveying. The experiments were conducted in a 13 m length of pipe of 0.080 m inside diameter. Particle velocity and concentration measurements were done at 4 m and 9 m in the 13 m pipe, photographic imaging was the technique used to determine particle velocities. The measurements were done at atmospheric pressure while the gas velocity ranged from 8-25 m/s. The materials tested were coarse plastics found in the region of Geldarts group D particles. Polyethylene of cylindrical shape with an average diameter of 3.13 mm was used in parallel with polyvinyl discal particles of 4.26 mm in average size. The respective densities are 946 and 1419 kg/m^3 for polyethylene and polyvinyl. The authors also investigated the effects of inducing a swirling motion in the pneumatic conveying. It was found that despite high gas velocities, particles were more concentrated on the bottom during horizontal flow without swirling [64]. When swirling was induced, the particles were much better distributed and are almost symmetrical relative to the pipe axis [64].

For both large particles investigated, without swirling the average particle velocity was found to be equal to 50-60% of the gas velocity between 8-24 m/s [64]. Meanwhile the particle velocity which was measured at a location of 4 and 9 m into the length of the pipe, was found to be equal at both locations, suggesting the entire acceleration of particles occurred rapidly and in

the first 4 m section [64]. The flux of particles used for conveying was fairly high as well at a value of 39.7 kg/m^{2}s which corresponds to a particle convey rate of 0.2 kg/s.

In summary, large coarse particles were found to travel at 50-60% of the gas velocity between the range of 8-24 m/s [64]. Therefore, for fine particles (<200 um) it is not unreasonable to suspect particle velocities exceeding 80% of the gas velocity for high gas velocities (>8 m/s) as their terminal velocity is much lower. This is even more valid for dilute flow conditions where the particles are found to follow a relatively straight path, although clustering may occur [62]. Finally, it was suggested that the slip velocity of fines is in the proximity of their median particle terminal velocity [62].

2.8. Entrainment Correlations

Entrainment correlations are a good indicator of the effect of operating conditions on the particles average residence time as it is proportional to the entrainment rate as shown in section 2.9. Most correlations proposed in literature for predicting entrainment rates are given for vertical distances above the TDH. This is largely a result of the general interest to minimize entrainment which reaches its minimum flux above the TDH. The correlations are in terms of the elutriation rate constant (K) where the entrainment rate ($\dot{E}$) is equal to the elutriation rate constant multiplied by the cross sectional area of the bed (A_c) and the mass fraction of entrained particles inside the dense bed (x_{FB}) [25].

$$\dot{E}_{ih} = K_{ih} * A_c * x_{FB,i} \qquad (\text{eq. } 2.11)$$

Equation 2.11 is written in terms of a given particle size "i" at a certain height "h" in the freeboard. When discussing the entrainment rate above the TDH, the height "h" is referred to the infinite height "∞". Each correlation proposed for the elutriation rate constant has its range of applicability for the superficial gas velocity (U_g), bed diameter (D_c) and particle diameter (d_p) used as shown in Table 2.2.

Table 2.2. Correlations for the elutriation rate constant Ki_∞ [25]. All parameters are in SI units.

Correlation	U_g (m/s)	D_c (m)	d_p (mm)	Reference
$\frac{K_{i\infty} \cdot g \cdot d_{pi}^2}{\mu(U - U_{ti})} = 0.0015 \cdot {Re_t}^{0.6} + 0.01 \cdot {Re_t}^{1.2}$	0.3-1.0	0.07-1.0	0.1-1.6	Yagi and Aochi (1955) as cited by Wen and Chen [65]
$\frac{K_{i\infty}}{\rho_f \cdot U} = \begin{cases} 1.26 \cdot 10^7 \cdot B^{1.88} \text{ for } B < 3.10 \\ 1.31 \cdot 10^4 \cdot B^{1.18} \text{ for } B > 3.10 \end{cases}$ $where\ B = \frac{U^2}{g \cdot d_{pi} \cdot \rho_p^2}$	0.3-0.7	0.05 × 0.53	0.04-0.2	Zenz and Weil [66]
$K_{i\infty}\left[\frac{kg}{m^2 s}\right] = 5.410 \cdot 10^{-5} \rho_p \left(\frac{U}{0.2}\right)^{3.4} \left(1 - \frac{U_{ti}}{U}\right)^2$ $for\ d_{pi}(\mu m) \leq \frac{10325}{{\rho_p}^{0.725}}$	0.2-0.7	not specified	0.03-0.78	Bayens et al [37] Note: only meant to calculate entrainment rate constant of fines
$K_{i\infty}\left[\frac{kg}{m^2 s}\right] = 0.35 \rho_p U (1 - \varepsilon)_H\ with$ $(1 - \varepsilon)_H = 7.41 \cdot 10^{-3} R^{1.87} A^{0.55} H^{-0.64}$ $and\ R = \sum x_{B,i} \left(\frac{U - U_{ti}}{U_{ti}}\right)\ for\ U_{ti} < U$	0.1-0.6	0.071 0.08 × 0.08 0.15 × 0.15	0.03-0.2	Nakagawa et al. [67]
$\frac{K_{i\infty} d_{pi}}{\mu} = Ar^{0.5} \exp\left(6.92 - 2.11 F_g^{0.303} - \frac{13.1}{F_d^{0.902}}\right)$ $with\ F_g = g \cdot d_{pi}(\rho_p - \rho_g)$ $F_d = C_d \frac{\rho_g U^2}{2}$	0.3-7.0	0.06-1.0	0.05-1.0	Choi et al. [68]

2.8.1. Entrainment correlation as a function of gas density and gas velocity

A generalized, and more simplified entrainment correlation has also been proposed by many [25, 29, 32, 33, 35, 69, 70] as shown in equation 2.12:

$$E = \beta * \rho_g * U_g^x \qquad \text{(eq. 2.12)}$$

Where β is a systems constant which groups together all constants that increase the entrainment rate in a linear fashion such as the cross sectional area of the fluidized bed. The gas density term encompasses one of the effects of pressure on entrainment. The other portion comes in the exponent variable *x* which is also a system constant and dictates to which power the gas velocity increases the entrainment rate. It is reported that for higher gas pressures, the entrainment rate becomes proportional to the gas velocity to a higher power [32, 33, 35, 69]. For which, the *x* exponent has been reported to vary between values of 3.0-8.0 [25, 32, 33, 35, 69]. As a result, increased gas velocity has a more profound effect on the rate of entrainment at high pressure. In the end, *x* is expected to be near the minimum value of 3.0 at atmospheric pressure and to steadily increase with pressure.

2.9. Particle Residence Time

The particle residence time in fluidized beds is of great interest as it is a key parameter determining the reaction conversion. Whether the application is drying or combustion, an appropriate residence time based on the reaction kinetics is key to the entire process optimization. Assuming well mixed conditions in the fluidized bed, the average residence time of particles is equal to the mass of particles inside the bed susceptible to entrainment (m_{FB}) divided by the rate of entrainment [71]. This yields the following equation:

$$\theta_{FB} = m_{FB}/\dot{E} \qquad \text{(eq. 2.13)}$$

However, the residence time is not homogeneous for a fluidized bed. There exists a distribution of residence times surrounding the average. Furthermore, there exists a particle size distribution in the fluidized bed. As a result, each particle varying in size will have a different rate of entrainment, mass fraction in the bed and therefore average residence time. In turn, a residence time distribution (RTD) will emerge in the fluidized bed. To characterize the RTD, the average residence time for each particle size must be determined. The average residence time for a given particle size ($\theta_{FB,i}$) is quite similar to the overall average residence time and is presented here:

$$\theta_{FB,i} = \frac{m_{FB} * x_{FB,i}}{\dot{E} * x_{E,i}} \qquad \text{(eq. 2.14)}$$

In this case, the average residence time of a given particle size is equal to its mass in the fluidized bed ($m_{FB} * x_{FB,i}$) divided by its respective entrainment rate ($\dot{E} * x_{E,i}$) [71].

Chapter 3. Experimental Equipment, Methods and Procedures

3.1. Experimental Apparatus

The fluidization system used in this work is shown schematically in Figure 3.1. It consists of a 0.152 m (6 inch) inside diameter stainless steel fluidization column having a height of 2.94 m. Pictures of the system are provided in Appendix A. The distributor plate was made of two perforated stainless steel plates, a total of 61 holes was used with a 6 mm hole diameter on top and a 4 mm hole diameter on the bottom plate. Furthermore, a 45 μm mesh was inserted in between the two stainless steel plates to prevent the static bed particles from falling through. Fluidizing gas flowrate was measured by an orifice plate meter (Rosemount model 3095) for atmospheric pressure and a vortex meter (Rosemount model 8800D) for operation at elevated pressure. The operating pressure was measured by a gauge pressure transducer (ABB model 266HSH). Furthermore, the pressure drop was measured across the fluidized bed and in the column freeboard by two differential pressure transducers (Yokogawa model EJX110A and ABB model 266DSH) which are also depicted in Figure 3.1.

A tube bank was constructed in-house to simulate the heat exchanger boiler tubes that will be present in the real combustor. Images of the tube bank are provided in Appendix B, however for confidentiality reasons, full dimensions of the tube bank could not be provided. The tube bank contained 5 rows of staggered tubes housed in a stainless cylindrical sleeve with a total height of 0.50 m and an inner diameter slightly smaller than the column I.D. The tube bank was lowered into the fluidization column so that it would sit on the distributor plate. The first row of tubes started at 0.22 m above the distributor plate. An opening on the side of the tube bank allowed for

the fines convey line to access the center of the column at a height of 0.16 m above the distributor plate.

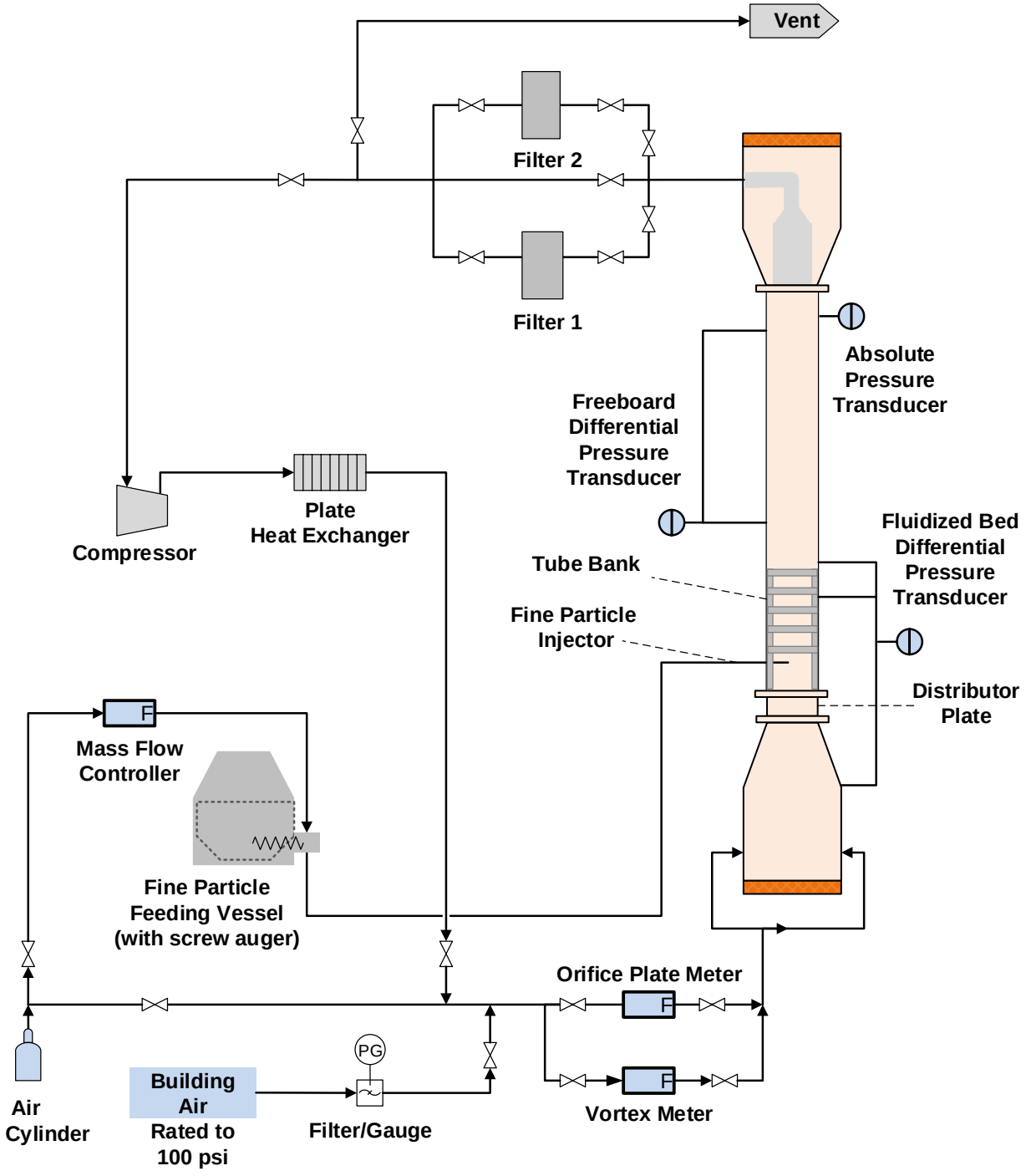

Figure 3.1. Schematic of Fluidization Apparatus.

A feeder (schenckprocess, AccuRate Volumetric Series model 10A) with a 0.019 m (3/4 in.) auger was placed inside a pressure vessel and used for the continuous feeding of the fines. The process flow diagram of this unit is shown in Figure 3.1; for visual representation consult Figure A.2 in Appendix A. The feeder discharge (via auger) was connected to the fluidization column via a 6.35 mm (1/4 inch) stainless steel tube pneumatic convey line (Figure A.3 and A.4). The conveying line was arranged such that the fines were injected horizontally from the sidewall of the column. The outlet of the fines injector was located 0.16 m above the distributor plate (Figure A.5) with the tip of the injector located at the center of the fluidization column. The pneumatic conveying of the fines was conducted by using air from a cylinder with its flow rate being controlled by a mass flow controller (Sierra instruments, model 840H-4-OV1-SV1-D-V4-S4).

The fines feed rate must be known accurately in order to have a good prediction of the entrainment rate once steady state is reached. Figure 3.2 presents the calibration conducted for the two fines feed rate used (5.9 and 8.9 kg/h). The feed rate decreases with the content of fines in the hopper, but no more than 2.7 % over the span of the entire solids inventory. Moreover, the feed rate variability reported by the coefficient of variation was less than 1.4%. As such, the feed rate is considered constant when there is more than 1.0 kg of fines remaining in the hopper.

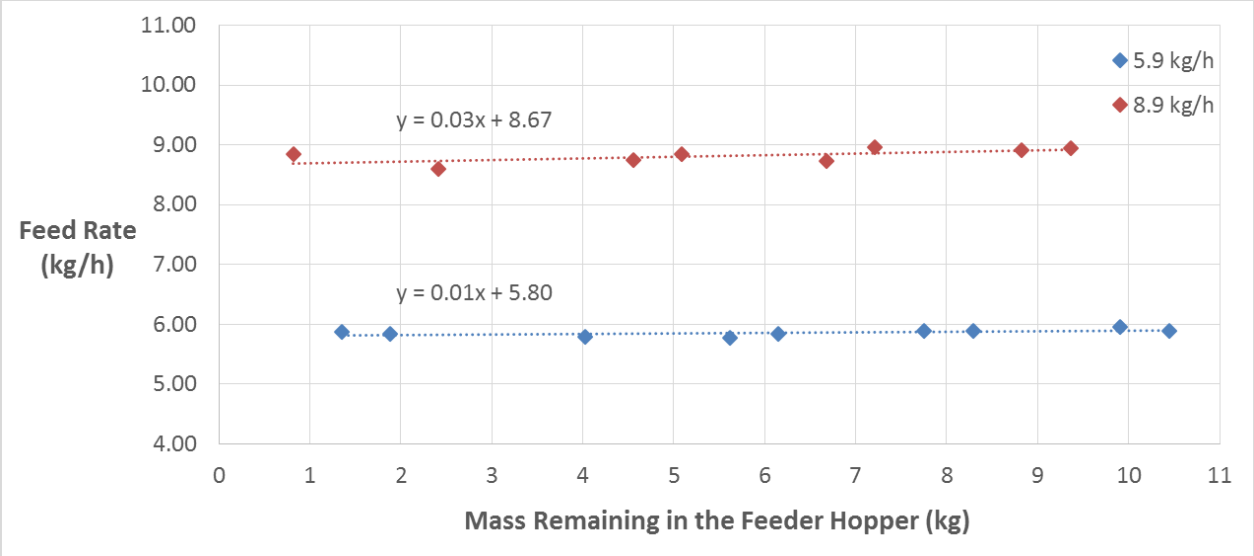

Figure 3.2. Feeder calibration; fines feed rate as a function of the mass of fines remaining in the hopper (0.8 to 10.5 kg).

The particles residence time measurements were conducted by capturing the entrained fines downstream with two parallel filters (Rosedale Products, model 6-18-2F-2-300-S316-C; Figure A.6) using filter bags as the filtration media. The filter bags were made of nylon monofilament mesh and had a 95% capture efficiency for 10 µm particles (Rosedale model NMO-10-P-8-RPO). The flow of entrained fines from one filter to another was controlled using a 3-way outlet valve as illustrated in Figures A.7 and A.8. This valve enabled the redirection of the flow instantaneously from one filter to the other with minimal solids accumulation in the piping during the change of flow.

3.2. Materials and Operating Conditions

The large bed material used was glass beads with a Sauter mean diameter of 1 mm, and particle density of 2500 kg/m^3. A mass of 13.5 kg was inserted for the large bed material which yielded a static bed height of 0.50 m without the tube bank and 0.62 m with the tube bank present. Fine glass beads were selected as the coal surrogate with a particle density of 2500 kg/m^3. Two sizes of fines were used with Sauter mean diameters of 64 and 83 µm respectively. The relevant particle size distribution (PSD) varied from 40-138 µm (for particle sizes greater than 1 wt%). The PSD for the two sizes of fines is illustrated in Appendix C. The terminal velocities of each individual particle size within the PSDs as a function of pressure are tabulated in Appendix D.

The fines average residence time in the fluidized bed was determined as a function of fluidization velocity, pressure, fines mean particle size, fines feed rate and with or without the tube bank present. The operating conditions are summarized in Table 3.1.

Table 3.1. Experimental matrix.

Pressure (kPa)	**Gas Velocity (U_g/U_{mf})**	**Fines Feed Rate (kg/h)**	**Presence of Tube Bank (Yes/No)**	**Fines Sauter Mean Diameter (um)**
101	1.5, 1.9	5.9	No	64
600	1.9	5.9	No	64
1200	1.9, 2.5, 3.2	5.9	No	64
101	1.5, 1.9	5.9	No	83
600	1.9	5.9	No	83
1200	2.5, 3.0	5.9	No	83
101	1.9	5.9	Yes	64
600	1.9	5.9	Yes	64
1200	1.9, 2.5, 3.2	5.9	Yes	64
101	1.5, 1.9	5.9	Yes	83
101	1.9	8.9	Yes	83
600	1.9	5.9	Yes	83
1200	2.5, 3.0	5.9	Yes	83
1200	2.5, 3.0	8.9	Yes	83

For the interpretation of results, when referring to the operating conditions of a specific experiment they are listed in the following order: "101 kPa – 1.9 U_{mf} – 5.9 kg/h – No TB – 64 um" where the following corresponds to the operating pressure, gas velocity, fines feed rate, the state of the tube bank, and Sauter mean diameter of fines. The precise minimum fluidization velocities, and operating gas velocities (U_g and U_{ex}) are tabulated in Appendix E. For all experiments, the temperature of the fluidization gas was kept constant at 24 ± 1°C. Each operating condition was repeated at least two times. The error bars presented in the results section of Chapter 5 are based on the reproducibility of experimental results representing a confidence interval of 95%.

3.3. Experimental Procedure

For atmospheric operations, the bed was fluidized with compressed building air. The building air pressure was set at 600 kPa (gauge) which enabled superficial gas velocities up to 1.08 m/s for the static bed height selected (13.5 kg of particles). For operation at elevated pressure, the system was operated in a closed loop where it was first pressurized with air cylinders to the desired pressure. Afterwards, the fluidization gas was recirculated via a centrifugal compressor with a variable speed drive to the desired fluidization gas flow rate. Temperature control of the heated gas at the outlet of the compressor was maintained with a plate heat exchanger using chilled water.

Table 3.2 demonstrates the gas velocity and Reynolds number used to convey fines for the pressures tested. Also an estimate for the terminal velocity of the largest relevant particle size being conveyed (greater than 1 wt%) based on the correlation by Haider and Levenspiel is provided [28]. LabVIEW program was used for data logging and control.

Table 3.2. Convey gas parameters for different operating pressures

Pressure (kPa)	Gas velocity to convey fines (m/s)	Piping Reynolds number (-)	Terminal velocity (d_p = 138 µm) (m/s)
101	25.0	10 239	0.86
600	12.4	30 000	0.54
1200	6.2	30 000	0.44

3.3.1. Measurement of fines average residence time in the fluidized bed

In order to accurately determine the average residence time of fines in the fluidized bed, the experiments were conducted with continuous injection of fines rather than by batch testing. It consisted of capturing the fines in 4 consecutive filter bags. The first mass measurement captured fines from 0-8 min, from start-up until steady-state was reached. The second mass measurement

captured the fines from 8-18 min (cumulative time) and acted as the first measure of the entrainment rate at steady-state. The third measurement was taken from 18-28 min and was the second measure of the entrainment rate at steady-state. Two measurement were taken to confirm the steady-state (i.e., both masses captured should similar). Afterwards the feeder was shut off while simultaneously switching to a new and fourth filter bag, upon which the final measurement was carried out. The final measurement consisted of entraining the mass of fines at steady-state inside the bed for a period of 15 min (the longer time period was to ensure complete elutriation of the fines from the large bed material); from 28-43 min cumulative time. This last measure quantifies the average mass of fines at steady state and subsequently the fines average residence time in the entire fluidization system.

The measured experimental residence time described above is for the entire fluidization apparatus (i.e., from the feeder to the filters) and not for the fluidized bed only. In order to obtain the average residence time in the fluidized bed itself, it must be isolated from the total residence time obtained by experiment. This requires determining and subtracting the residence time of fines in the external piping, both upstream and downstream. Here are the associated residence times to account for; in order, from the feeder to the filters:

1. From the feeder discharge, immediately into the ¼ inch (0.005 m) tubing convey line, to the end of the injector inside the fluidized bed. (θ_{convey}; upstream)
2. In the fluidized bed of large particles. (θ_{FB}; measure of interest)
3. In the freeboard above the fluidized bed ($\theta_{Freeboard}$; downstream)

4. In the large elbow. (θ_{Elbow}; downstream) The elbow is located at the top of the 6 inch (0.15 m) fluidization column and connects to the 1.5 inch (0.038 m) piping to reach the filters. See Figure A.9.
5. Finally from the outlet of the large elbow to the filter. ($\theta_{to\ Filter}$; downstream)

Altogether, the 5 aforementioned residence times equal the fines residence time within the entire system (θ_{total}) which is measured experimentally. Therefore, the θ_{FB} which is desired, is found by the following equation:

$$\theta_{FB} = \theta_{total} - (\theta_{convey} + \theta_{Freeboard} + \theta_{Elbow} + \theta_{to\ Filter}) \qquad \text{(eq. 3.1)}$$

To determine the residence time of fines in the external piping of the fluidized bed, it could be obtained using the particle velocity and distance of travel. However, for this experimental apparatus the particle velocity was only measured in the freeboard. This was acceptable as it will be shown later that the other piping residence times were deemed negligible. To note, the shorter the length of the piping is, and the greater the superficial gas velocity inside, the more likely the residence time of fines was to be short and negligible.

3.3.2. Measurement of fines average residence time in the freeboard

The largest residence time outside the fluidized bed was suspected to be in the freeboard; compared to all other sections of piping, it has a much lower superficial gas velocity (1.09 m/s) with a distance to travel of 1.87 m. Both the average particle velocity and average residence time of fines in the freeboard were obtained by measuring the pressure drop and mass flow rate of fines in the freeboard.

The freeboard pressure drop ($\Delta P_{Freeboard}$) was measured continuously during each experiment using a differential pressure transducer. For the experiments conducted, the $\Delta P_{Freeboard}$ was measured along a 1.05 m axial section of the fluidization column in the freeboard (for average $\theta_{Freeboard}$). The heights and distances of importance concerning the measure of the average freeboard residence time are summarized in Table 3.3.

Table 3.3. Heights of importance along the fluidization column for average $\Delta P_{Freeboard}$ measurements

	Distance (m)
Total fluidization column height from the distributor plate to the large elbow	2.94
Location of 1st $\Delta P_{Freeboard}$ port above the distributor plate	1.07
Location of 2nd freeboard $\Delta P_{Freeboard}$ port above the distributor plate	2.12
Total freeboard above 1st $\Delta P_{Freeboard}$ port	1.87
Length of freeboard excluded in $\Delta P_{Freeboard}$ measure	0.82
Static bed height without the tube bank	0.50
Static bed height with the tube bank present	0.62

The differential pressure transducer measures the dynamic pressure drop. As a result, the $\Delta P_{Freeboard}$ measures the following, slightly adjusted value of the total freeboard pressure drop, displayed in equation 3.2. It is a Bernoulli energy balance that omits the frictional losses against the wall, and the possible vertical acceleration of the two phases as they were found to be negligible. Evidently, there was no mechanical work being conducted in the freeboard.

$$\Delta P_{Freeboard} = \left[\rho_{solid} g h_{\Delta P}(1 - \varepsilon_{Freeboard}) + \rho_{gas} g h_{\Delta P,Freeboard}(\varepsilon_{Freeboard})\right] - \rho_{gas} g h_{\Delta P} \quad \text{(eq. 3.2a)}$$

$$\Delta P_{Freeboard} = (\rho_{solid} - \rho_{gas})(1 - \varepsilon_{Freeboard}) g h_{\Delta P,Freeboard} \quad \text{(eq. 3.2b)}$$

$$\varepsilon_{Freeboard} = 1 - \frac{\Delta P_{Freeboard}}{(\rho_{solid} - \rho_{gas}) g h_{\Delta P,Freeboard}} \quad \text{(eq. 3.2c)}$$

The only unknown in the previous equation is the average gas voidage in the freeboard ($\varepsilon_{Freeboard}$). After isolating and solving for the average gas voidage in equation 3.2c, the average mass of fines in the freeboard volume where $\Delta P_{Freeboard}$ is taken ($m_{Freeboard,\Delta P}$) across can be determined with the following equation:

$$m_{Freeboard,\Delta P} = \rho_{solid} \cdot A_C \cdot h_{\Delta P,Freeboard}(1 - \varepsilon_{Freeboard}) \qquad \text{(eq. 3.3)}$$

As seen from equation 3.3, the $\Delta P_{Freeboard}$ signal corresponds to the average mass of fines along its measurement height of 1.05 m ($m_{Freeboard,\Delta P}$) and not quite the entire average mass of fines in the freeboard ($m_{Freeboard}$). To determine the later requires extrapolating the results obtained for the 1.05 m of freeboard to its total height of 1.87 m. This was scaled linearly meaning the estimated average mass in the total freeboard and corresponding average residence time would be 1.78 times greater as displayed in equation 3.4.

$$m_{Freeboard} = \frac{1.87}{1.05} * m_{Freeboard,\Delta P} \qquad \text{(eq. 3.4)}$$

The corresponding average residence time of fines in the freeboard was then obtained from the mass of fines in the freeboard divided by the entrainment rate at steady state as seen in the following equation:

$$\theta_{Freeboard} = \frac{m_{Freeboard}}{\dot{E}} \qquad \text{(eq. 3.5)}$$

It is based on the same entrainment rate at steady state (average of 2nd and 3rd filter capture) than the one used to determine the experimental residence time in the entire system (θ_{total}) from equation 2.13.

Finally, the average residence time in the freeboard had values ranging from 4.0-12.7 s, between all operating conditions. As a percentage of the total experimental residence time, it represents 8-31% of its total value, with a median value of 15% (5 of 24 operating conditions had values greater than 20%). Therefore, the average residence time in the freeboard was non negligible when isolating for the average residence time in the fluidized bed (equation 3.1). In foresight, since the average residence time in the freeboard was below 20% of the total experimental residence time for most cases and on the order of seconds, the three other residence times in the external piping: θ_{convey}, θ_{Elbow} and $\theta_{to\ Filter}$ were deemed negligible. For starters, θ_{convey} and $\theta_{to\ Filter}$ had superficial gas velocities approximately 25 and 15 times greater than that in the freeboard, which would undoubtedly reduce the residence time significantly. Meanwhile, for θ_{Elbow} the travel distance in the large elbow was smaller at 0.26 m and also had a greater gas velocity flowing through. In the end, equation 3.1 can be simplified to the following equation:

$$\theta_{FB} \approx \theta_{total} - \theta_{Freeboard} \qquad \text{(eq. 3.6)}$$

3.4. Differential Pressure Measurement Technique used for Gas Bubble Dynamics

In this work, two types of differential pressure measurements – local and global – were conducted to study gas bubble dynamics within. Both measurements were taken when fines entrainment had reached steady state. For experiments without the tube bank, the differential pressure was measured across a 0.15 m vertical distance, at two axial locations of 0.16-0.31 m (referred to as low pressure port - LPP) and 0.31-0.46 m (referred to as medium pressure port - MPP) above the distributor plate, providing local information about the bubble dynamics at various heights along the bed. However, when the tube bank was present, the metal sleeve housing the horizontal tubes blocks the pressure ports along the fluidization column, preventing the local measurements of differential pressure. Instead, the differential pressure was measured across the entire static bed height, providing a global measurement of the bubble dynamics for the entire fluidized bed. In order to have an adequate comparison between experiments conducted with and without the tube bank, a global measurement across the entire static bed height was also taken without the tube bank. For both global measurements, the bottom pressure port was located below the distributor plate while the top port was located just below the static bed height (Table 3.4). As seen from Table 3.4, for the same mass of large inert bed material, the tube bank increases the static bed height due to the occupied volume of the tube bank and metal sleeve.

Table 3.4. Location of the differential pressure ports and the static bed height.

Tube Bank	Height Relative to Distributor Plate			
	Bottom Port (m)	**Top Port (m)**	**Static Bed Height (m)**	**Tube Bank Height (m)**
No – Local (1)	0.159	0.311	0.500	0.50
No – Local (2)	0.311	0.464		
No - Global	Below Distributor	0.464		
Yes - Global	Below Distributor	0.616	0.625	

Prior to demonstrating results, it was important to validate the differential pressure measurement equipment. In order to have valid data collection, it is necessary to choose equipment which will not distort or dampen the pressure signal [72]. Starting with the probe diameter, an optimum of 2 to 5 mm was reported in literature for pressure measurements [72], of which a probe diameter of 5 mm was used. In addition, it is best to keep the distance between the transducer and measurement port to a minimum, however probe lengths up to 2.5 m are acceptable for data analysis methods that focus on the lower frequencies (20 Hz or smaller [72]). This criteria was also satisfied.

For global measurements, the bottom pressure port was taken below the distributor plate, thus it was important to ensure the distributor plate was not distorting the total differential pressure signal. More specifically, the distortion of the standard deviation of the global pressure drop signal could be problematic since it is used directly to estimate the average bubble size in equation 2.8. Therefore, to have accuracy in the estimated average bubble size, it is imperative that the distributor plate pressure fluctuations are marginal relative to the pressure fluctuations of the bed. The verification results are presented in Table 3.5 for all operating conditions where the pressure drop across the distributor plate was at its greatest. It is shown for the three operating pressures of 101, 600 and 1200 kPa and is compared with the global differential pressure measurement of the

fluidized bed. From Table 3.5, it is clear that the pressure drop associated to the distributor plate is not negligible and should be subtracted from the global pressure drop in order to obtain the mean pressure drop across the bed of particles. However, the standard deviation associated to the distributor plate pressure drop is negligible compared to that of the global measurement (15 times smaller or more). Such that, there is confidence in the standard deviation of the global pressure drop measurement not being dampened or exuberated by the distributor plate.

Table 3.5. Distributor plate pressure drop and its standard deviation relative to the global measurement across the fluidized bed

Operating Condition	**ΔP (kPa)**	**Standard Deviation of ΔP (kPa)**	**Experimental Trial**
101 kPa - 1.9 U_{mf} - No TB	6.24	1.703	Global - Trial 1
	6.23	1.776	Global -Trial 2
	0.60	0.038	Distributor plate only
101 kPa - 1.9 U_{mf} - TB present	7.51	1.885	Global -Trial 1
	8.02	1.678	Global -Trial 2
	0.62	0.039	Distributor plate only
600 kPa - 1.9 U_{mf} - No TB	6.38	1.373	Global -Trial 1
	6.35	1.375	Global -Trial 2
	0.84	0.043	Distributor plate only
600 kPa - 1.9 U_{mf} - TB present	7.60	0.980	Global - Trial 1
	N/A	N/A	Global -Trial 2
	0.87	0.044	Distributor plate only
1200 kPa - 3.2 U_{mf} - No TB	7.83	1.583	Global -Trial 1
	7.96	1.572	Global - Trial 2
	2.08	0.043	Distributor plate only
1200 kPa - 3.2 U_{mf} - TB present	7.21	0.636	Global -Trial 1
	7.25	0.632	Global - Trial 2
	2.15	0.044	Distributor plate only

Lastly, for the estimated average gas bubble size reported with equation 2.8, errors bars are provided based on the reproducibility of experimental results and represent a confidence interval of 95% for the average bubble size reported.

Chapter 4. Results and Discussion – Fluidized Bed Hydrodynamics

The fluidized bed hydrodynamics, namely gas bubble dynamics, were first investigated by differential pressure signal analysis at various axial locations along the bed. The bubble dynamics were studied as it is believed to be an important parameter influencing the entrainment of fines from the fluidized bed [25]. Quantifying the bed hydrodynamics should also provide physical insights into the particle movement of the large bed material for the various conditions tested; which inevitably affect the movement of fines. For instance, it is important to determine the impact of smaller versus larger gas bubbles on the degree of particle entrainment. As gas bubble size and rise velocity increase, gas bubbles bursting at the bed surface have more momentum and are more prone to eject particles into the freeboard. As fine particles are ejected into the freeboard in greater quantities, particle entrainment can be increased. Furthermore, the fluidization flow regime, whether it be bubbling, slugging or turbulent could also have a significant impact on the extent of particle entrainment.

First, local measurements without the tube bank are presented to show the effect of axial position in the bed on the estimated average bubble size and the early onset of the slugging regime with bed elevation. The second set of results are global measurements presented for the entire static bed height, and were used to investigate the effects of gas velocity, tube bank and pressure on the estimated average bubble size. To note, the average bubble size calculated using equation 2.8 is most accurate for a monistic differential pressure signal (i.e., resembling a singular sine wave function; also having a maximum amplitude that is constant and frequent). The reason being that under a distribution of bubble sizes, the estimated average bubble size calculated from equation 2.8 is skewed to the larger size. Thus, the average bubble size is only reported for operating

conditions that produced monistic differential pressure signals. As a result, more emphasis is put on the time series of the differential pressure signal, which also contains information in the time domain. The time series are presented for a duration of 4 s at steady state, with a generic time stamp of 0-4 s. In some cases, supplementary information is also provided with the use of the frequency power spectrum on the global differential pressure signal.

4.1. Local Differential Pressure Measurements

The local differential pressure measurements conducted provide valuable information on the behavior of gas bubbles as they rise through the bed. The expected trend from literature is an increase in bubble size at higher axial positions in the bed [25]. Results are shown here for the two operating conditions listed in Table 4.1.

Table 4.1. Local differential pressure measurements experimental matrix. No tube bank present.

Operating Condition	Differential Pressure Location
101 kPa - 1.9 U_{mf} - No TB	LPP
	MPP
1200 kPa – 2.5 U_{mf} - No TB	LPP
	MPP

The first comparison is shown at 101 kPa - 1.9 U_{mf} for the LPP and MPP locations (Figure 4.1). The differential pressure measurement using the MPP configuration is at a higher elevation than LPP and therefore larger bubbles were expected. The slugs appear less stable and less consistent at the lower elevation LPP. This is interpreted by the fact that the signal in Figure 4.1a is less consistent itself. The bubble size distribution is more multi-modal at the LPP elevation compared to MPP. This could be the result of the bubbles further coalescing as they rise through the bed and therefore the bubble size distribution would be reduced. Also from Figure 4.1a there are higher frequencies present in addition to the dominating frequency equally observed at the

higher elevation MPP in Figure 4.1b. Such that smaller bubbles are present at the LPP axial location but not for MPP. The monistic differential pressure signal in Figure 4.1b corresponds to an estimated average bubble size of 8.6 cm. The minimum bubble size to be considered in the slugging regime was 6.1 cm for the column used, which corresponds to the 40% column diameter criteria for slugging from section 2.1. Thus slugs were obtained relatively quickly at 101 kPa and 1.9 U_{mf}; that is 0.31 m above the distributor plate.

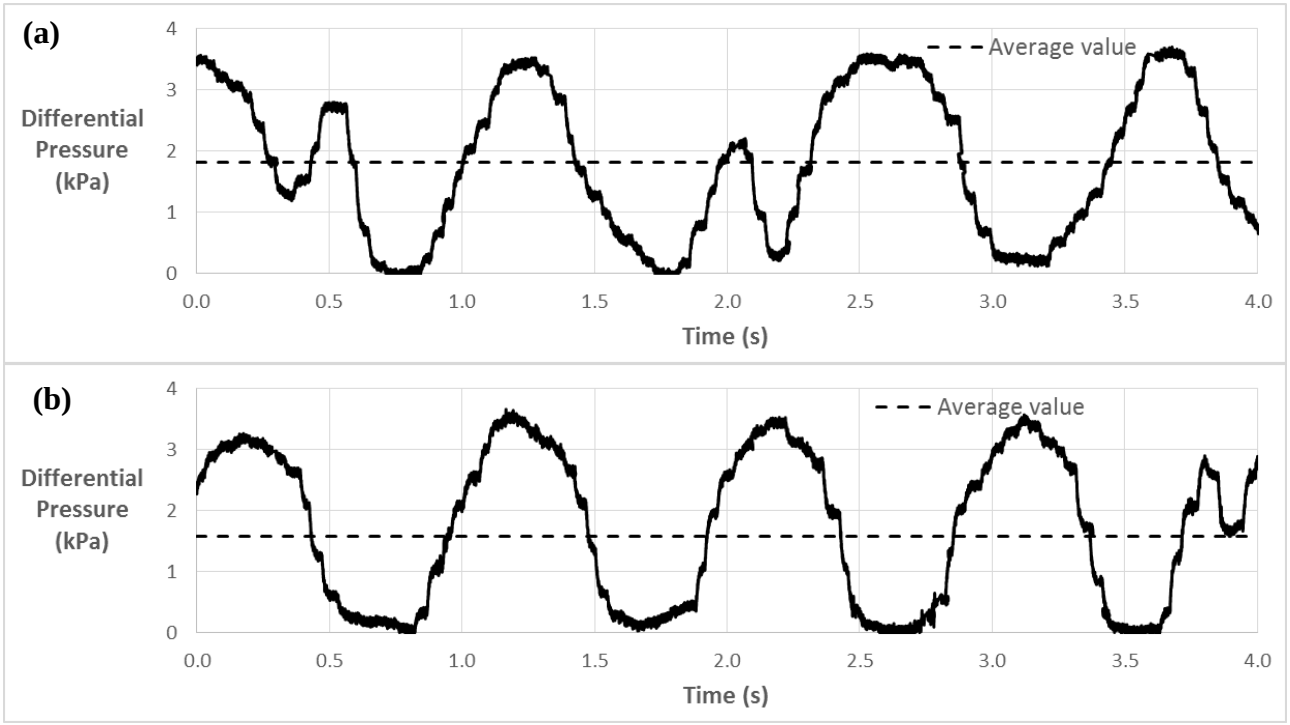

Figure 4.1. Differential pressure signal time series for (a) 101 kPa - 1.9 U_{mf} – LPP, (b) 101 kPa - 1.9 U_{mf} - MPP.

Similar to the results observed for the slugging regime at 101 kPa, there appears to be a dominant frequency at elevated pressure (1200 kPa) of the same order (near 1.0 Hz) as that observed at 101 kPa for the MPP location (Figure 4.2). However, the signal in Figure 4.2b is no longer a singular sine wave although the signal remains periodic. This implies that the large slugs are not as stable at 1200 kPa compared to 101 kPa, with multiple sine peaks broken in two

indicating bubble break up or instability. In addition, the differential pressure signal time series is demonstrated for the lower axial position LPP in Figure 4.2a. At a lower axial position in the fluidized bed, the bubble frequency is augmented while the bubble size is reduced significantly (proportional to the amplitude of the differential pressure signal). Such that at a lower axial position, smaller bubbles are obtained at 1200 kPa compared to 101 kPa, which indicates bubbles coalescing at a lesser rate with axial position at 1200 kPa. The results are in agreement with literature [25, 54, 55], and from a material balance, as bubbles are broken down, they must have a greater frequency such that the volumetric flow rate remains constant throughout the bed.

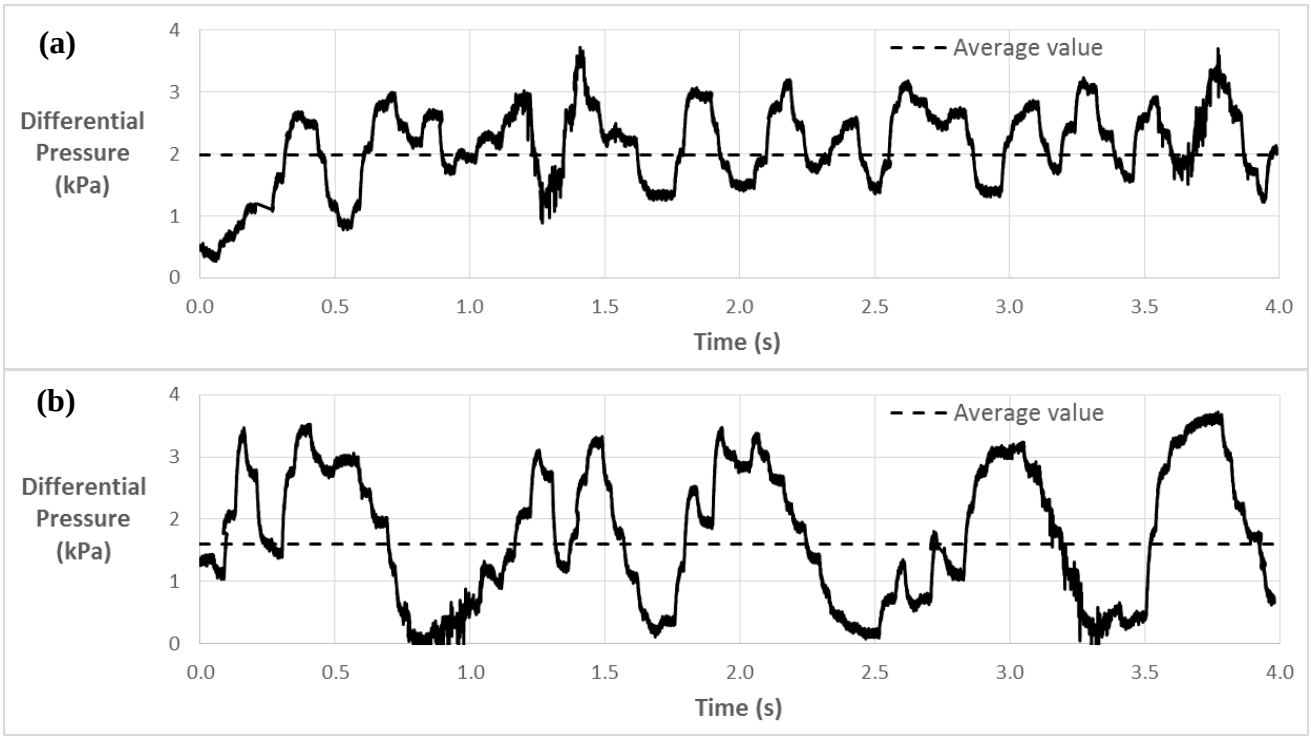

Figure 4.2. Differential pressure signal time series for (a) 1200 kPa – 2.5 Umf – LPP, (b) 1200 kPa – 2.5 Umf – MPP.

For both operating pressures (and more so at MPP), there are instances where the local differential pressure measurement practically attains a value of 0 kPa. This would indicate the passage of slugs

actually taking up almost the entire measurement volume (0.152 m in length and diameter). This is an additional confirmation of the large slugs present in the free bed. Furthermore, it would seem equation 2.8 in this case is underestimating the average bubble size, as it estimated an average bubble size of 8.6 cm at 101 kPa - 1.9 U_{mf} – MPP.

4.2. Global Differential Pressure Measurements

By measuring the gas bubble dynamics across the entire static bed height, information regarding the effect of gas velocity, pressure and tube bank was obtained.

4.2.1. Effect of gas velocity and tube bank at atmospheric pressure

Figure 4.3 compares the differential pressure signal time series and the average bubble size for gas velocities ranging from 1.5 to 1.9 U_{mf} without the presence of tube bank. The time series of the differential pressure measurement show that the bubble size distribution appears to be quite narrow for both gas velocities with each signal having a clear, dominant frequency in the order 1-1.2 Hz. Results also show periodic slugs obtained at both velocities. Without a tube bank present, the average bubble size increased significantly with increased gas velocity. For instance, from 1.5 to 1.9 U_{mf}, the relative estimated bubble size increased by 87% from 6.4 to 12.0 cm.

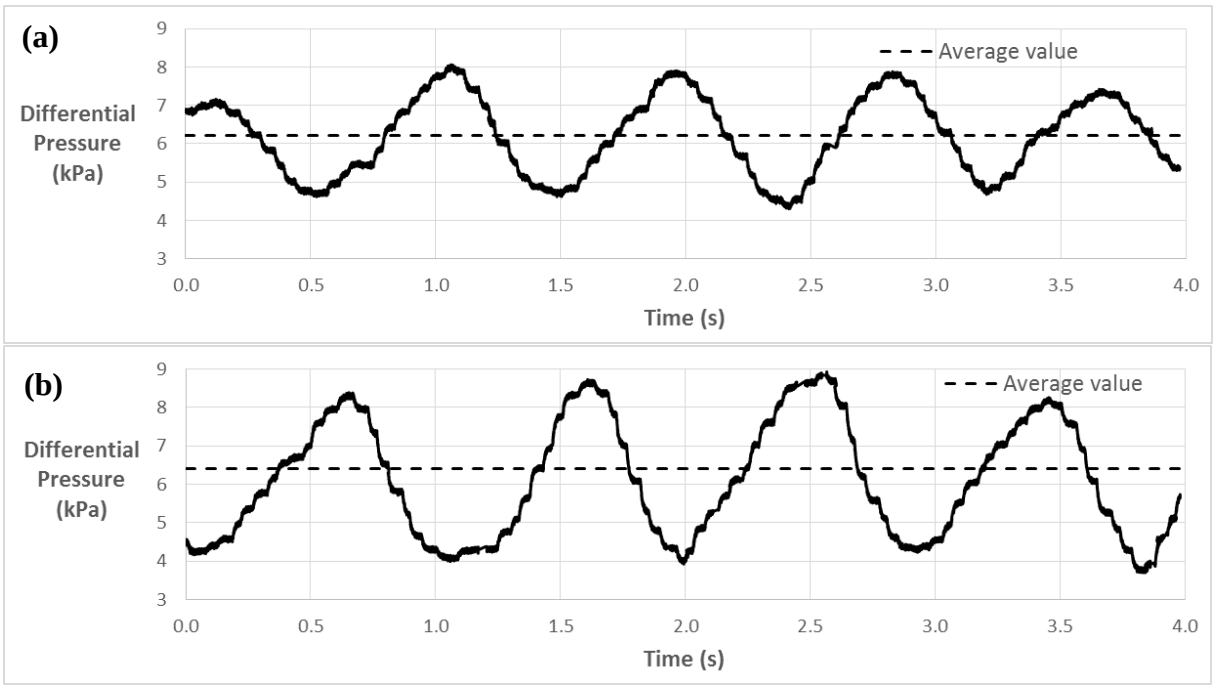

Figure 4.3. Global differential pressure signal time series for (a) 101 kPa - 1.5 U_{mf} - No TB, (b) 101 kPa - 1.9 U_{mf} - No TB.

Meanwhile, when the tube bank was present, the gas velocity seemed to have mixed results concerning the impact on the bubble size (Figure 4.4). For the most part, bubbles were found to be smaller at 1.5 U_{mf}, however, occasionally similarly large slugs were also present. Evaluating the differential pressure time series at 1.5 U_{mf} (Figure 4.4a) there are instances of periodic slugs with the tube bank present, however the bubble size distribution was widened compared to without a tube bank. In some instances, the bubbles were larger and in others they were smaller compared to the previous estimated average bubble size of 6.4 cm without a tube bank. As a result, the bubble frequency is no longer constant with the tube bank present, having its own distribution widened. This indicates the ability of the tube bank to break up the bubbles although slugs were still periodically obtained in the end. This could be due to the ability of bubbles coalescing in the free bed above the tube bank.

The results were similar at 1.9 U_{mf}, the bubble size was changed to a multimodal distribution with the presence of the tube bank and large slugs are seen but not in a consistent pattern. Mostly, the bubble size appears to be reduced, this is deduced from comparing the amplitude of the differential pressure signal in Figure 4.3b and Figure 4.4b. Although, the maximum bubble size appears to be greater with the tube bank present. Once more, the large bubbles with the tube bank present were believed to occur due to the fact that bubbles had time to coalesce in the free bed above the tube bank. Otherwise, where the horizontal tubes are present, the bubble size is believed to be smaller than in the free bed. Previous research also indicates the ability of a tube bank to break up bubbles and impede bubble growth at 101 kPa with increased gas velocity compared to a free bed [54, 55]. Such that it can be concluded that the presence of a tube bank at 101 kPa, due to its obstruction of flow, causes a multimodal distribution of bubble sizes with larger bubbles present but more so resulting in smaller bubbles.

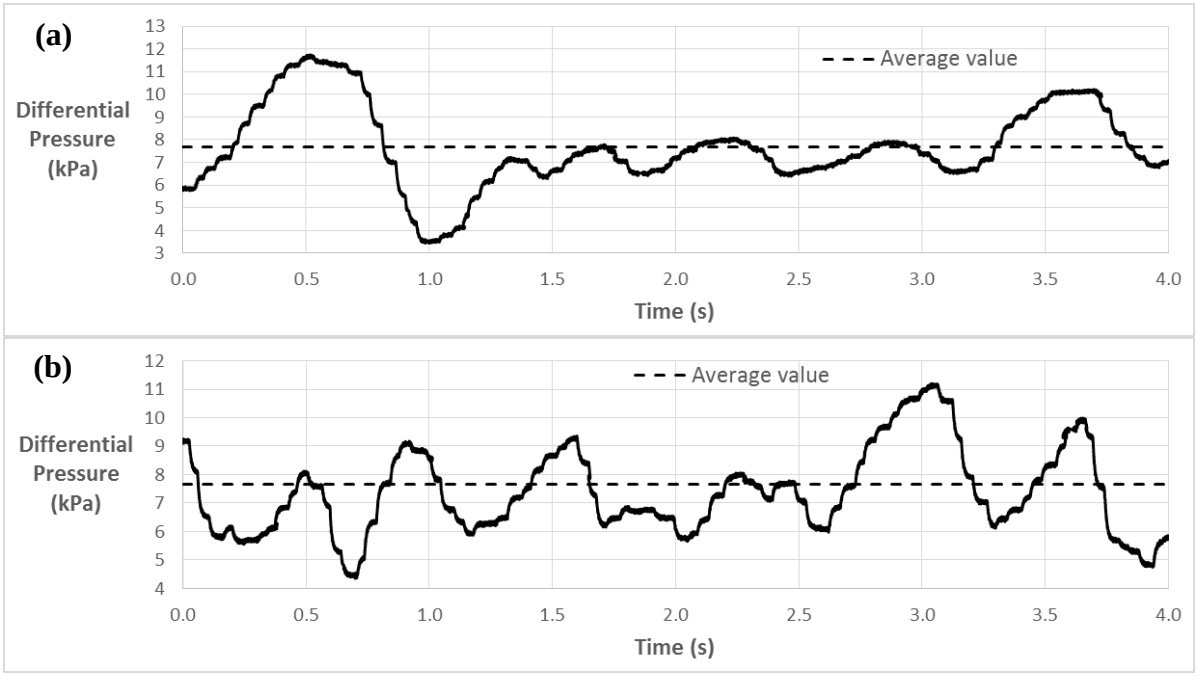

Figure 4.4. Global differential pressure signal time series for (a) 101 kPa - 1.5 U_{mf} - TB present, (b) 101 kPa - 1.9 U_{mf} - TB present.

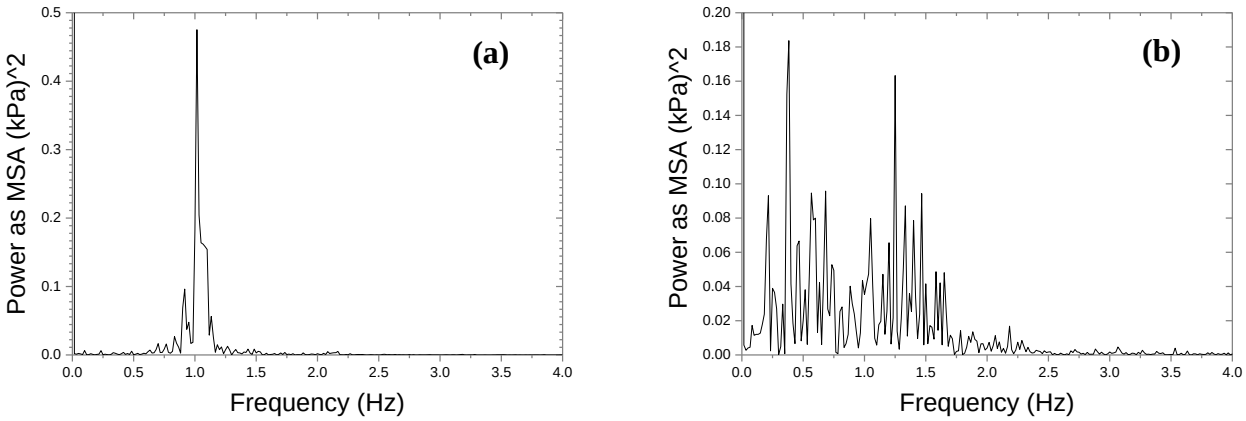

Figure 4.5. Power spectrum of the global differential pressure time series for (a) 101 kPa - 1.9 U_{mf} - No TB, (b) 101 kPa - 1.9 U_{mf} - TB present.

In addition, the frequency power spectrum is shown in Figure 4.5 at 101 kPa - 1.9 U_{mf} for both conditions with and without a tube bank present. This is further indication of the conclusions made beforehand. As can be seen from the power spectrum in Figure 4.5a, without the tube bank present, there is a dominating frequency near 1.0 Hz with very few others present. Conversely, when the tube bank was inserted, some of the large slugs were broken down, but not all and this can be seen in the broadened frequency distribution. Frequencies smaller than 1.0 Hz would indicate larger slugs still present with frequencies above 1.0 Hz indicating the resulting smaller bubbles.

4.2.2. Effect of gas velocity and tube bank at elevated pressures

Subsequently, bed hydrodynamics were evaluated at 600 and 1200 kPa. At 600 kPa and a gas velocity of 1.9 U_{mf} the average bubble size still reports a slugging regime without a tube bank. The bubble size was estimated to be 9.5 cm, despite the differential pressure signal not being entirely monistic (Figure 4.6a). Even if the average bubble size was overestimated, it would remain well above the 6.1 cm bubble size criteria for the slugging regime with the column used. Compared to 101 kPa, the tube bank was more effective at 600 kPa in reducing the bubble size. For greater

detail on the bubble dynamics, the differential pressure signal time series for both cases is shown in Figure 4.6.

Unlike at 101 kPa and without the tube bank present, the signal peaks at 600 kPa shown in Figure 4.6a were less consistent indicating a greater distribution of bubble size; although the signal remained periodic at an approximate frequency of 1.2 Hz. For 600 kPa with the tube bank present (Figure 4.6b), not only was the average bubble size smaller (magnitude of peaks were lesser), but the distribution around the average was increased. Such that, both pressure and tube bank are effective at reducing the average bubble size and increasing the distribution of smaller bubbles.

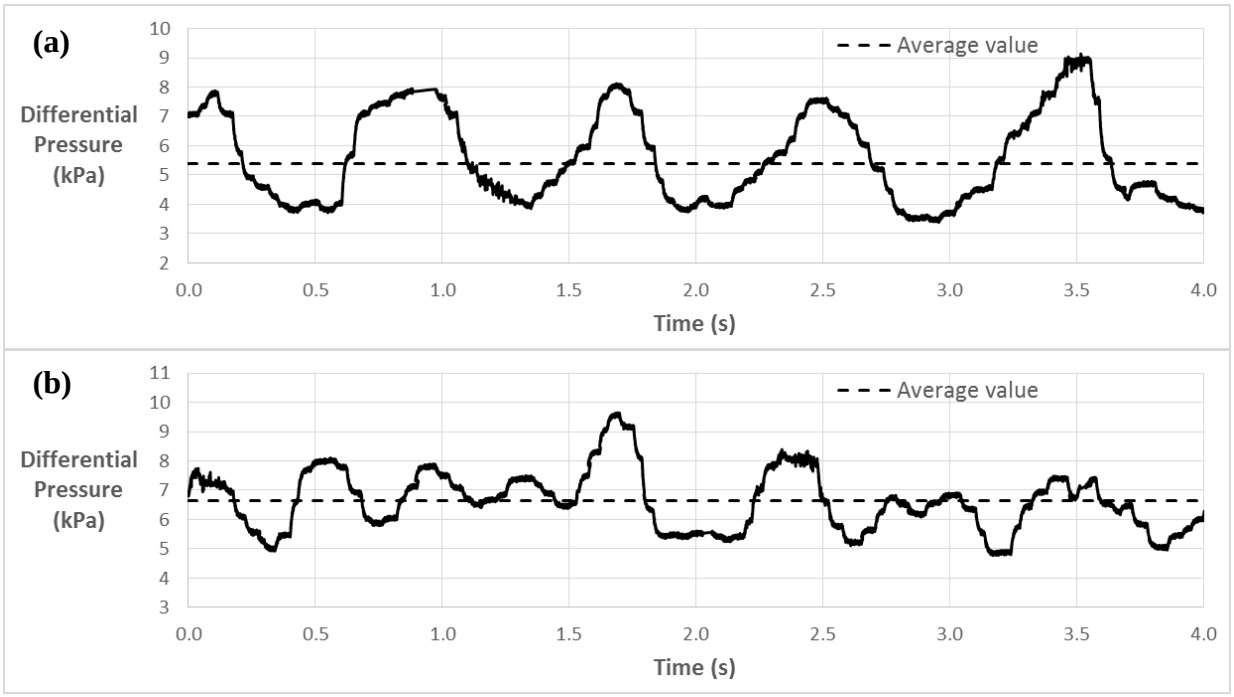

Figure 4.6. Global differential pressure signal time series for (a) 600 kPa – 1.9 U_{mf} – No TB, (b) 600 kPa – 1.9 U_{mf} – TB present.

Continuing with the impact of gas velocity and tube bank, experiments were conducted at 1200 kPa. Results were obtained for multiple velocities: 1.9, 2.5 and 3.2 U_{mf}. However, most of the individual average bubble sizes were not reported as the differential pressure signals were not

monistic as seen in Figure 4.7. Differential pressure signal time series at 1200 kPa are only shown for three conditions where the differences in bubble dynamics were greatest: 1.9 U_{mf} – No TB; 3.2 U_{mf} – No TB; and 3.2 U_{mf} – TB present.

As can be seen in Figure 4.7a and b, the maximum bubble size increased with gas velocity at 1200 kPa when the tube bank was not present. This is indicated by the larger amplitude of peaks in the differential pressure time series signal at 3.2 U_{mf} compared to those observed at 1.9 U_{mf}. Also, as the gas velocity was increased, the distribution of bubble size also broadened. At constant excess gas velocity, the bubbles were generally smaller at 1200 kPa (3.2 U_{mf}) compared to their 101 kPa (1.9 U_{mf}) counterpart. Similarly the distribution around the average bubble size was found greater at 1200 kPa when the tube bank was not present.

Lastly, the differential pressure signal time series is presented at 3.2 U_{mf} with the tube bank present in Figure 4.7c. The difference is quite profound when the tube bank is present at high gas velocity and pressure as seen by comparing it to Figure 4.7b (without tube bank). The bubble size is heavily reduced, the distribution around the average bubble size is actually reduced as most bubbles are smaller, and most importantly, the slugging regime was mitigated as the estimated average bubble size was found to be 4.4 cm. Here the use of equation 14 was deemed applicable as the signal was fairly monistic in amplitude (Figure 4.7c). In the end, it was found that the highest pressure of 1200 kPa with the presence of the tube bank was most effective at breaking up the bubbles – which will enhance mass transfer in the combustor. This is in agreement with one of the few groups of researchers who studied the hydrodynamics of fluidized beds as a function of pressure and tube bank [54, 55].

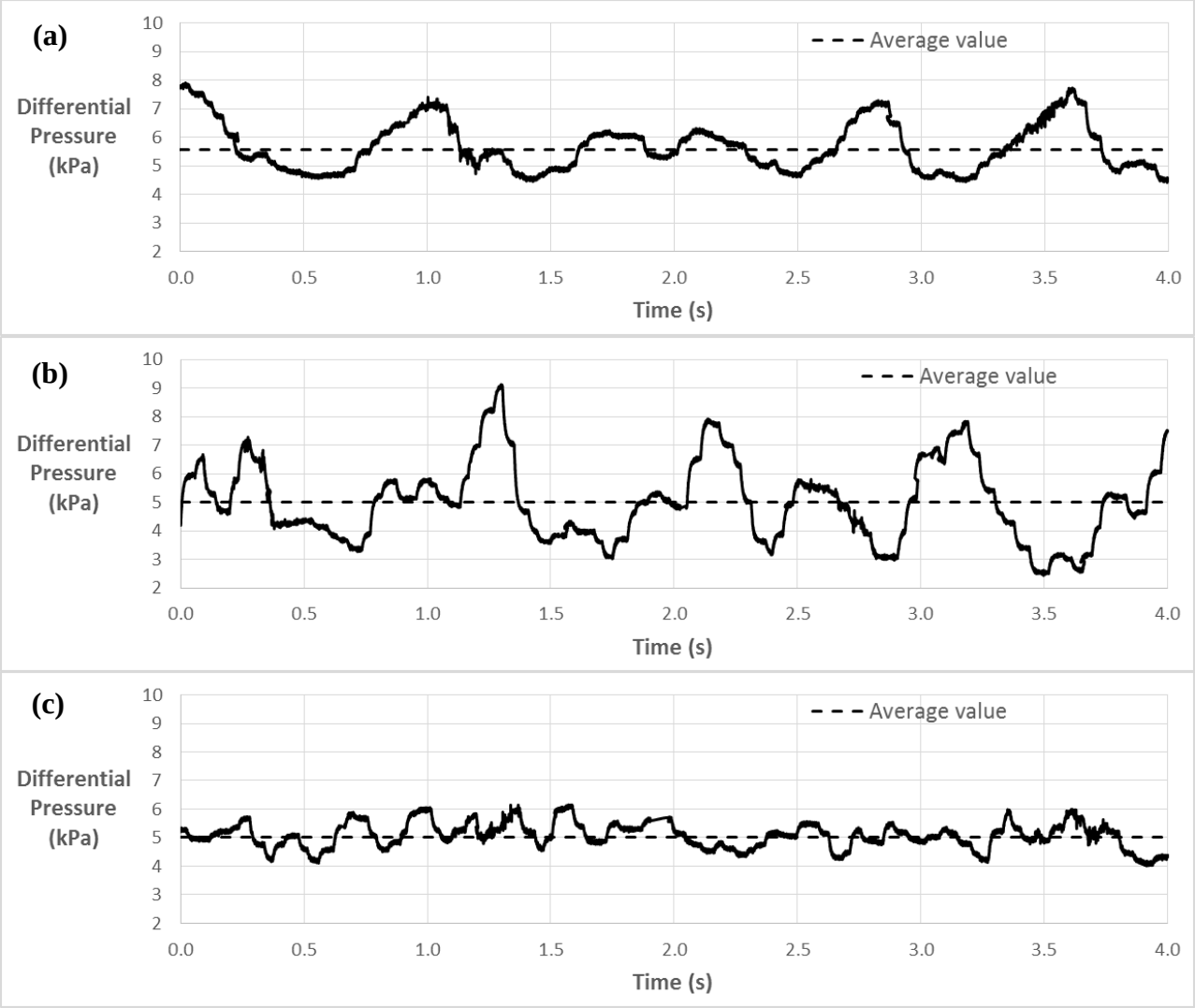

Figure 4.7. Global differential pressure signal time series for (a) 1200 kPa - 1.9 U_{mf} - No TB, (b) 1200 kPa - 3.2 U_{mf} - No TB (c) 1200 kPa - 3.2 U_{mf} - TB present.

For further evidence of the discussed trends, the frequency power spectrum is provided in Figure 4.8 for the operating conditions of 1200 kPa - 3.2 U_{mf} with and without the tube bank present. As said, when the tube bank was not present, increased pressure (1200 kPa) at constant excess gas velocity was found to broaden the bubble size distribution based on the broadened frequency distribution as seen in Figure 4.8a in comparison to Figure 4.5a.

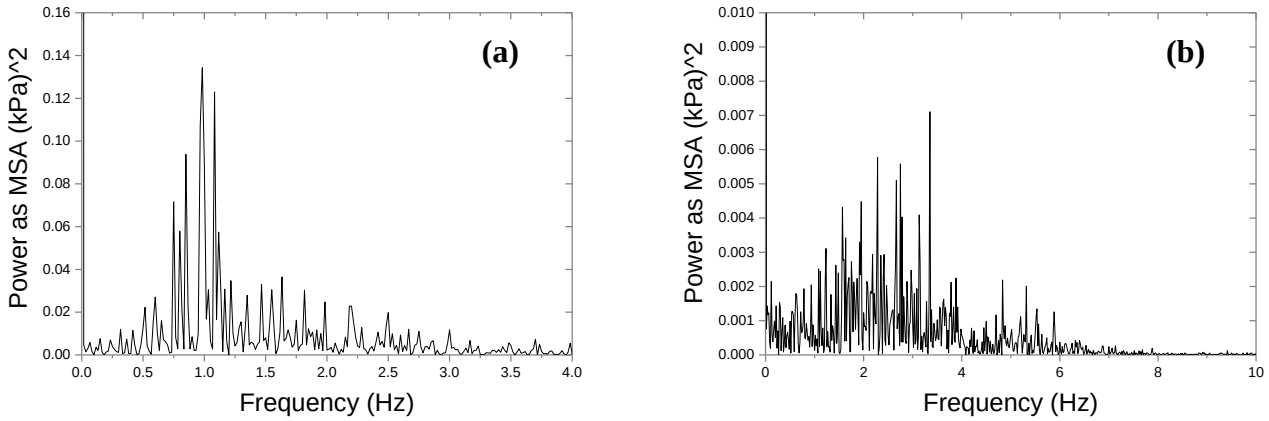

Figure 4.8. Power spectrum of the global differential pressure time series for (a) 1200 kPa - 3.2 U_{mf} - No TB, (b) 1200 kPa - 3.2 U_{mf} - TB present.

Similarly, when the tube bank was present, at 3.2 U_{mf}, the bubble size was heavily reduced, as shown in Figure 4.8b from the higher range of frequencies compared to Figure 4.8a.

4.2.3. Gas bubble dynamics summary

The gas bubble characteristics, namely bubble size and the distribution around the average, were studied as a function of axial location in the bed, gas velocity, pressure and tube bank. The effect of axial location was investigated without a tube bank and it was found that at 101 kPa, slugs were formed rapidly, within the first 0.31 m of the fluidized bed. Meanwhile at 1200 kPa, slugs were only confirmed at a higher axial location of 0.46 m in the fluidized bed. For its part, the effect of gas velocity was generally found to increase the average and maximum bubble size. At elevated pressures, increased gas velocity rendered the size distribution more multimodal. Regarding the presence of a tube bank, it was successful in breaking the bubbles, but not all of them and as a result broadened the bubble size distribution at 101 kPa. The tube bank in combination with elevated pressures of 600 and 1200 kPa significantly reduced the average bubble size, and actually narrowed the bubble size distribution as only smaller bubbles were formed.

These trends can be visualized in the final Figure 4.9 which showcases all 4 combinations of pressure and tube bank at a constant excess gas velocity of 0.51 m/s. This corresponds to a U_g/U_{mf} ratio of 1.9 at 101 kPa and 3.2 at 1200 kPa. From Figure 4.9, it is clear the operating conditions of 1200 kPa - 3.2 U_{mf} - TB present, were best at mitigating the slugging regime.

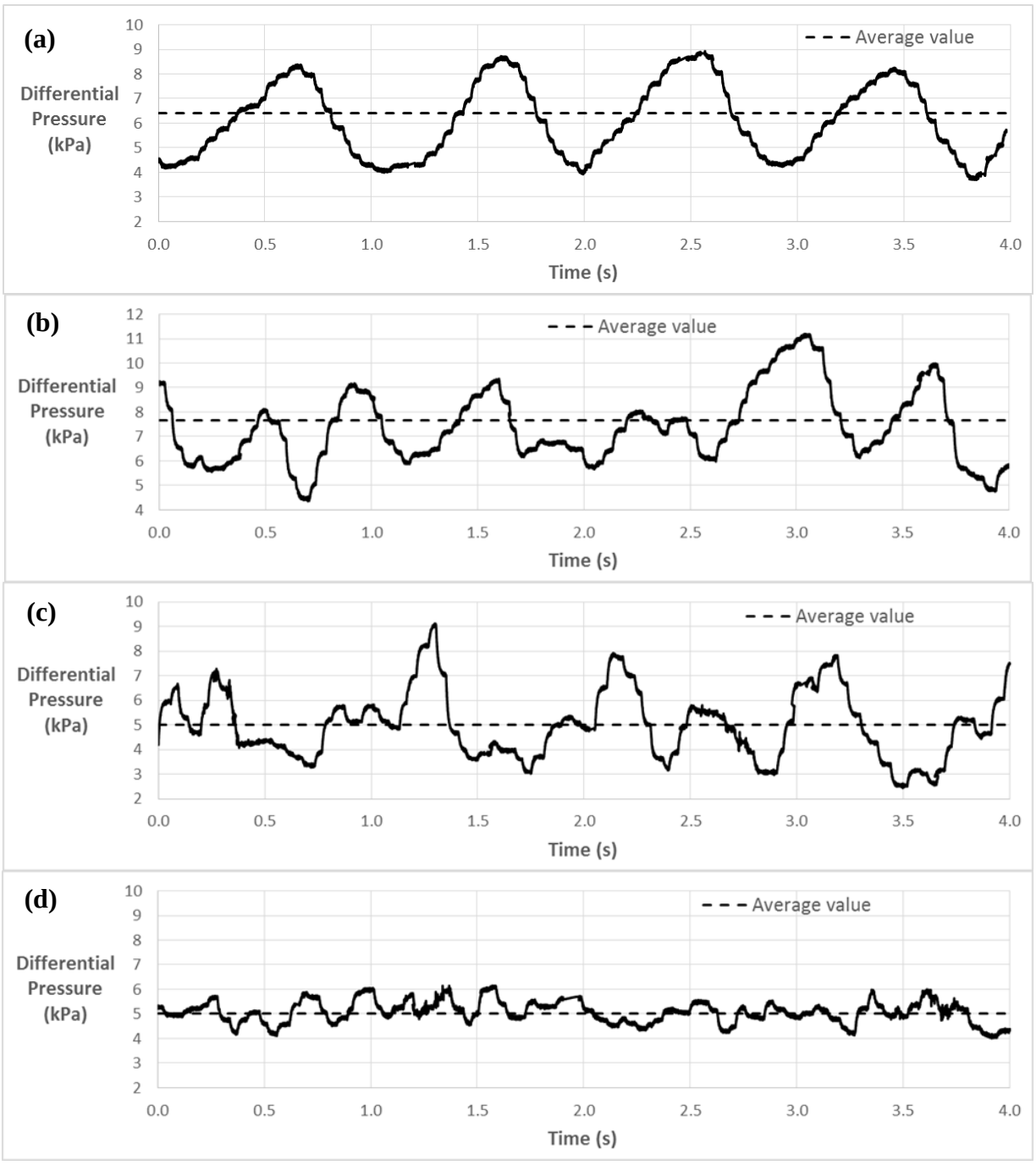

Figure 4.9. Global differential pressure signal time series for (a) 101 kPa - 1.9 U_{mf} - No TB, (b) 101 kPa - 1.9 U_{mf} - TB present, (c) 1200 kPa - 3.2 U_{mf} - No TB, and (d) 1200 kPa - 3.2 U_{mf} - TB present. The excess gas velocity was constant at 0.51 m/s.

Chapter 5. Results and Discussion – Fines Average Residence Time

This chapter examines the average residence time of fines in the fluidized bed as a function of gas velocity, operating pressure, fines mean particle size, fines feed rate as well as the presence of a tube bank. In order to determine the average residence time of fines, equation 2.13 must be solved for. It consists of quantifying the average mass of fines at steady-state (m_{FB}) that remains within the large bed material during fluidization, and dividing it by the entrainment rate ($\dot{E}$). The entrainment rate at steady state ($\dot{E}$) should equal the feed rate, but as demonstrated in section 3.1, there is natural variance for the feed rate such that the proposed feed rate calibration does not always yield what is measured experimentally. Rather, it has been found more accurate to base the value of $\dot{E}$ on the mass measurements obtained at steady state for each experiment, which was the average of two measures, each time-averaged for 10 min.

5.1. Validating Steady State

Equally important, is to be assured the entrainment flux has reached a steady-state before the 4th captured mass is taken in order to yield the proper mass of fines at equilibrium. This is to effectively determine the fines residence time at steady-state. To validate the steady state, the 2nd and 3rd captured masses are compared, both of which are mass measurements of the steady-state entrainment flux. Therefore, they should have similar masses. Table 5.1 compares the first and second steady-state measurements for various experiments conducted throughout the experimental matrix. From Table 5.1, the percentage difference between both captured masses is very close, and the average absolute deviation is approximately 1.7%. Such that it is reasonable to assume steady state was reached after 8 min.

Table 5.1. Comparison between the first and second steady-state captured mass.

Pressure (kPa)	U_g/U_{mf}	Particle size (um)	Feed rate (kg/h)	Tube bank (Yes/No)	Steady-state entrained mass (kg)		
					First capture	Second capture	Percentage difference (%)
101	1.9	64	5.9	Yes	0.941	1.026	9.0%
101	1.9	64	5.9	No	0.907	0.921	1.5%
101	1.9	64	5.9	No	0.976	0.983	0.7%
101	1.9	64	5.9	Yes	0.971	0.985	1.4%
101	1.9	64	8.9	Yes	1.464	1.465	0.1%
101	1.5	64	5.9	No	0.983	0.999	1.6%
101	1.9	64	8.9	No	1.457	1.482	1.7%
101	1.5	64	5.9	No	0.975	1.021	4.6%
101	1.5	64	5.9	Yes	0.989	0.986	-0.3%
101	1.9	64	5.9	No	0.921	0.902	-2.0%
600	1.9	64	5.9	Yes	0.912	0.889	-2.6%
600	1.9	64	5.9	Yes	0.895	0.893	-0.2%
1200	2.5	64	5.9	Yes	0.955	0.946	-1.0%
1200	1.9	64	5.9	Yes	0.915	0.907	-0.9%
600	1.9	64	5.9	No	0.903	0.918	+1.6%
101	1.9	83	5.9	No	1.038	1.032	-0.6%
1200	2.5	83	5.9	Yes	0.993	1.004	+1.1%
1200	3.0	83	5.9	No	1.003	1.029	+2.6%
101	1.9	83	8.9	Yes	1.494	1.488	-0.5%
1200	2.5	83	8.9	Yes	1.585	1.514	-4.5%
1200	3.0	83	5.9	Yes	0.986	0.984	-0.2%
101	1.5	83	5.9	Yes	1.030	1.027	-0.3%
101	1.9	64	5.9	No	1.037	1.038	+0.1%

5.2. Average Residence Time – Effect of Operating Conditions

The residence time is averaged for the entire particle size distribution (PSD) and presented as a function of the fines Sauter mean diameter. Despite the residence time presented as an average, it is important to remember that there is a residence time distribution associated to the PSD of fines and also due to the dynamics of the residence time in a fluidized bed (it is rarely constant for a given particle susceptible to entrainment). Nonetheless, valuable information is still obtained with the average residence time. Overall results presented show the effects of gas velocity, operating pressure, the presence of a tube bank, and fines mean particle size. The effects of the fines feed rate on the average residence time of fines within the fluidized bed is also presented.

5.2.1. Effect of gas velocity, pressure, tube bank and fines mean particle size

The effect of gas velocity was examined at atmospheric pressure (101 kPa), and at elevated pressures of 1200 kPa. The effect of gas velocity was also investigated as a function of the mean particle size of fines, as well as a function of whether or not the tube bank was present. The results are presented in Figure 5.1 and Figure 5.2. In all cases, the effect of gas velocity was not statistically significant for the range investigated. Although for both mean particle sizes a trend would have been expected such that when the gas velocity was increased a decrease in residence time would have been anticipated.

In parallel it is important to evaluate the bed hydrodynamics and how its relation to entrainment could change with increased gas velocity. Starting with the pressure of 101 kPa and without the tube bank present, it was confirmed by Figure 4.3 that the fluidized bed was slugging in both instances at 1.5 and 1.9 U_{mf}. However, the estimated average bubble size was significantly

different at approximately 6.4 and 12.0 cm respectively. Large bubbles are known to increase entrainment for larger group B particles and above, but not necessarily for smaller group A particles [25]. For the fines in question, with a density of 2500 kg/m^3, the delimitation from Geldart group A to group B, is approximately at 80 µm.Thus, it is not unreasonable to see no effect of gas velocity despite the larger average bubble size at 1.9 U_{mf} as a portion of the fines would be independent of the bubble size for their entrainment [25].

In contrast, at 101 kPa, with the tube bank present, the bed hydrodynamics results showed similar bubble dynamics as a function of increased gas velocity with an increased bubble breakage and widened bubble size distribution for both gas velocities (Figure 4.4). As bubbling characteristics did not change as much with increased gas velocity when the tube bank present, no differences in the fines average fluidized bed residence time would have been anticipated, and none were found.

Regarding the effect of gas velocity on bubble dynamics at elevated pressure, without a tube bank present, the impact was significant with the estimated average bubble size increasing substantially. However, there was little impact on bubble dynamics when the tube bank was present. This was illustrated in Figure 4.7. Since there was no effect of gas velocity at elevated pressure, it further supports the possibility of the fines average residence time in the fluidized bed being independent to the change in bubble dynamics caused by the increased gas velocity.

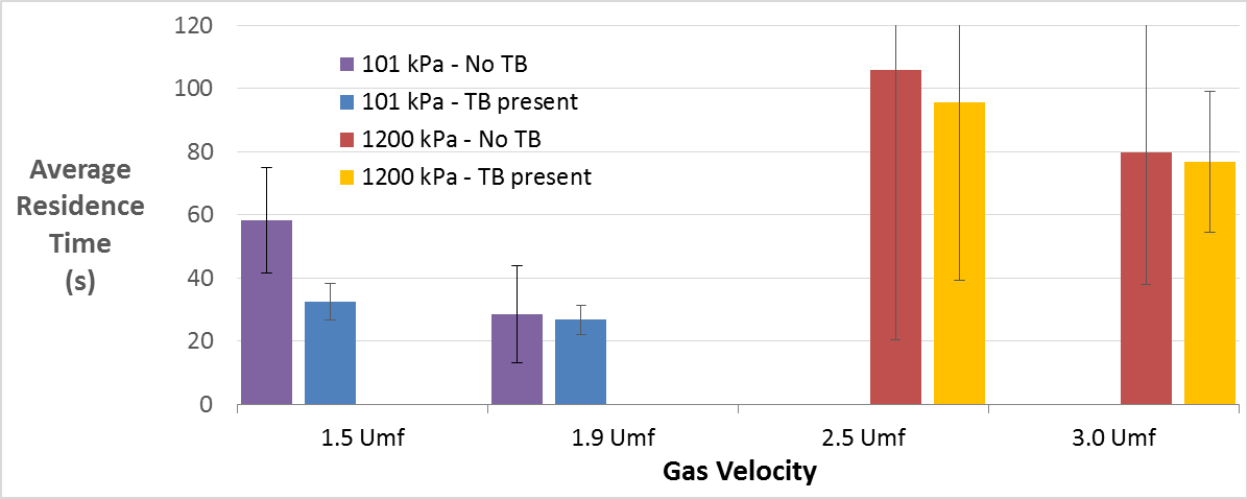

Figure 5.1. Fines average residence time as a function of gas velocity for pressures of 101 and 1200 kPa, with and without the tube bank present, and for the mean particle size of 83 µm.

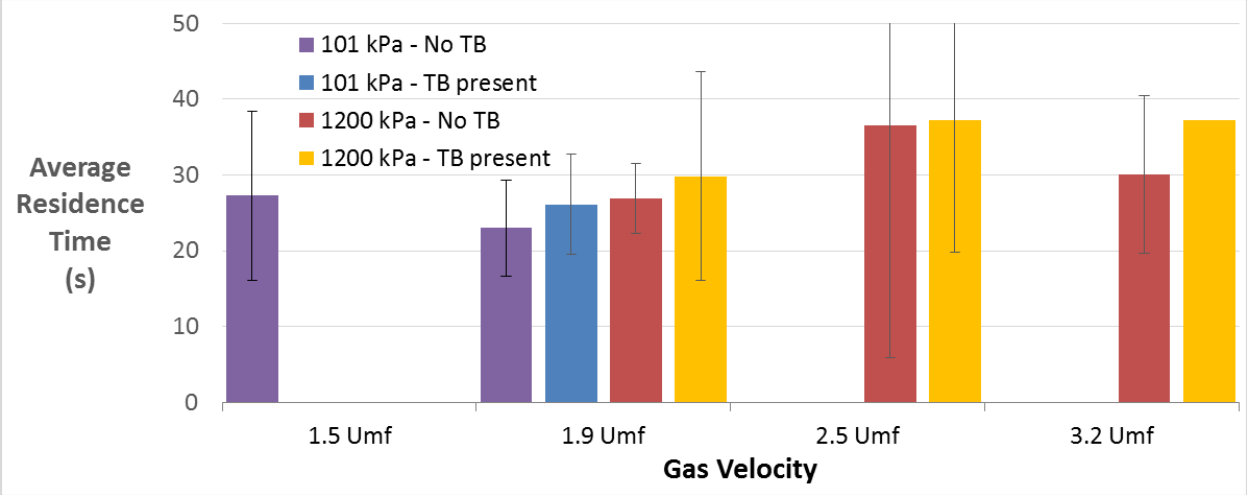

Figure 5.2. Fines average residence time as a function of gas velocity for pressures of 101 and 1200 kPa, with and without the tube bank present, and for the mean particle size of 64 µm.

The effect of operating pressure on the average residence time was investigated for pressures of 101, 600 and 1200 kPa. The effect of pressure was not statistically significant for 64 µm particles but was for 83 µm particles when the tube bank was present (Figure 5.1 and Figure 5.2).

Concerning the 64 µm fines, the average residence time of fines in the fluidized bed remained unaffected despite the changes in bubble dynamics caused by pressure. For instance,

when the tube bank was present, some slugs were still observed at 101 kPa, but at 1200 kPa the bubbles were completely broken down (see Figure 4.9b, and d). This is in agreement with the previous findings that the bubble characteristics, and more specifically large bubbles, were not as pronounced in reducing the average residence time for 64 µm fines.

As for 83 µm fines, the Sauter mean diameter and a greater percentage of its PSD (52% compared to 32% for the 64 µm fines) fall within Group B particles. Such that their entrainment and subsequent average residence time should be more influenced by bubble characteristics as discussed earlier. Thus, it is reasonable to see increased pressure increasing the average residence time in the fluidized bed at 1200 kPa when the tube bank was present. This could only be observed at constant excess gas velocity (101 kPa – 1.9 U_{mf} vs 1200 kPa – 3.2 U_{mf}) for which the average bubble size was significantly reduced at 1200 kPa. Recall the slugging regime was even mitigated at 1200 kPa as displayed in Figure 4.9. Without a tube bank present, the bubble dynamics were more similar between 101 and 1200 kPa (see Figure 4.9a, and c) which could be the reason why the effect of pressure under those conditions was not statistically significant.

Similar results to those observed at 1200 kPa were obtained at 600 kPa. Here as well, increased pressure with the tube bank present at a constant excess gas velocity was found to have an increased fines average residence time in the fluidized bed. This was limited to the 83 µm fines, which between 101 kPa – 1.5 U_{mf} and 600 kPa – 1.9 U_{mf}, the fines average residence time in the fluidized bed increased from 32 ±6 to 83 ±27 s. As with the pressure of 1200 kPa, the bubbles are broken substantially with the tube bank present at 600 kPa (Figure 4.6) compared to 101 kPa.

Regarding the impact of the tube bank itself, for 64 µm fines, there was not a statistically significant difference between results with and without a tube bank as demonstrated in Figure 5.2. Once more, this is despite the changed hydrodynamic behavior with the tube bank present. The same was observed for the 83 µm fines at the exception of 1 of 4 conditions which was statistically significant (Figure 5.1). Upon which the presence of a tube bank was found to reduce the average residence time of fines in the fluidized bed at 101 kPa – 1.5 U_{mf}.

One possible reason to explain the reduced average residence time with the presence of the tube bank could be the increased local gas velocities with the tube bank present. The gas velocity is increased locally with the presence of a tube bank, such that it could improve entrainment and therefore reduce the fines average residence time. Although fines in the fluidized bed do not follow a rectilinear pathway to the surface, it is hypothesized that entrainment at low gas velocities and with larger particles would be most difficult as the particle velocities are at their lowest. Thus, at this stage, any increase in gas velocity by presence of the tube bank, should have the most benefits, and perhaps this is why the effect was only statistically significant at low gas velocity. In addition, it may be that the increased gas velocity with the tube bank present was less beneficial to the entrainment of 83 µm fines at higher gas velocity and higher pressure due to competing effects with a reduced bubble size. The reduced bubble size with the tube bank present was less pronounced at 101 kPa and 1.5 U_{mf}.

5.2.2. Fines average residence time distribution

Also of interest is the distribution of residence times associated to the average value. Ideally, the smaller the fines average residence time distribution is, as seen from its coefficient of

variation, the better, as it makes for easier operation and process control. Unlike other processes at steady state, the fines average residence time in the fluidized bed is an oscillating process due to the bubble dynamics within. Such that, despite statistically closing the mass balance during the 20 minutes sampling period, the mass of fines in the fluidized bed is constantly oscillating due to cycles of bubble ejection. For instance, after the bursting of a large bubble at the bed surface carrying fines in its nose or wake, it would result in an instantaneous drop in the mass of fines in the fluidized bed. This is a small scale phenomenon for which it makes it difficult (and practically impossible) to obtain the same mass of fines in the fluidized bed at steady state over limited repeated tests e.g. 2 to 3 trials. This is due to the methodology used for which the 4^{th} filter bag capture was a snapshot of the mass of fines in the fluidized bed at that precise instant. This could be a contributing reason for the large error bars observed on the average residence time of fines in Figures 5.1 and 5.2. However, it is worth mentioning the number of trials conducted for most conditions was at its lowest for statistical significance i.e. 2 trials. The number of trials per condition is indicated in the summary table at the end of this chapter (Table 5.2).

The oscillating nature of the fines average residence time in the fluidized bed would also be observed in the standard deviation of the average freeboard residence time, which was measured continuously. By being directly downstream of the fluidized bed, the freeboard pressure drop measurements should detect the oscillating nature of bubbles carrying and ejecting fines as well. Thus, by looking at the standard deviation of the freeboard pressure drop, it can validate and support the variance observed on the fines average residence time in the fluidized bed as a real phenomenon. Unfortunately, only the effect of fines feed rate obtained conclusive results.

5.2.3. Effect of fines feed rate

The final parameter investigated regarding its influence on the fines average residence time was the fines feed rate. Two feed rates were tested, 5.9 and 8.9 kg/h. All results shown in previous sections were at a fines feed rate of 5.9 kg/h.

At steady state, the fines feed rate equals the entrainment rate for a once through injection of fines. While the average residence time of fines in the fluidized bed (θ_{FB}) is inversely proportional to the entrainment rate at steady state ($\dot{E}$), it is also directly proportional to the average mass of fines in the fluidized bed at steady state (m_{FB}) as shown in equation 2.13. If the increase in m_{FB} is proportional to the increase in the fines feed rate, then the average residence time of fines in the fluidized bed will remain the same. However, to which degree m_{FB} will proportionally increase is unknown. As a result, the increase in m_{FB} remains the experimental uncertainty in order to determine the effect of the fines feed rate.

Three comparisons are provided to evaluate the effect of fines feed rate, they all occurred with the tube bank present and the larger fines of 83 µm (Figure 5.3). Beginning at an operating pressure of 101 kPa and a gas velocity of 1.9 U_{mf}, the fines average residence time in the fluidized bed decreased as the fines feed rate was increased but the result was not statistically significant. In addition, when comparing the coefficient of variation of the average freeboard pressure drop, there was no statistically significant difference. Thus, the fines average residence time distribution is not expected to be improved at a higher feed rate of 8.9 kg/h for the operating condition of 101 kPa - 1.9 U_{mf}.

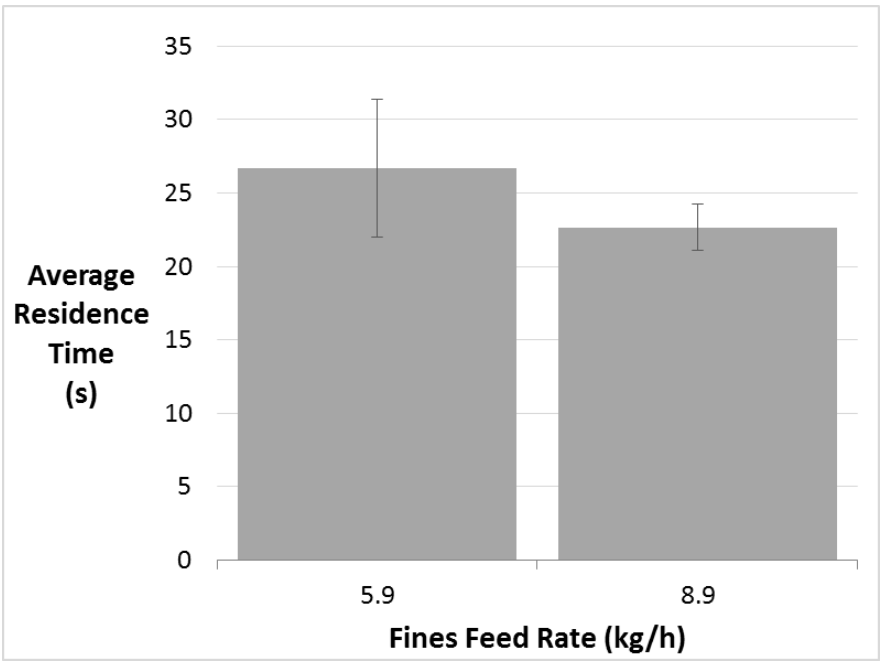

Figure 5.3. Fines average residence time as a function of fines feed rate, 101 kPa - 1.9 U_{mf} - TB present - 83 µm.

The next comparisons are at an elevated pressure of 1200 kPa for gas velocities of 2.5 U_{mf} and 3.0 U_{mf} (Figure 5.4a, b). Again, the fines feed rate was not found to have a statistically significant impact. However, the variance on the average residence time was improved for both velocities unlike what was previously observed at a pressure of 101 kPa. At 1200 kPa - 2.5 U_{mf}, the coefficient of variation on the average freeboard pressure drop improved from approximately 12-17% at 5.9 kg/h to 10% at 8.9 kg/h. Similarly, for 1200 kPa - 3.0 U_{mf}, the coefficient of variation on the average freeboard pressure drop improved from approximately 15-18% at 5.9 kg/h to 12-13% at 8.9 kg/h.

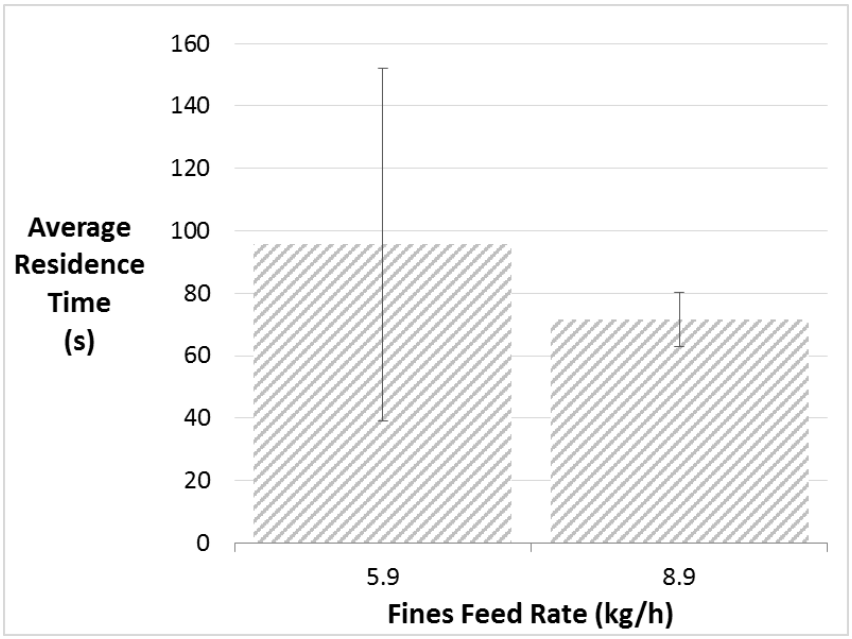

(a)

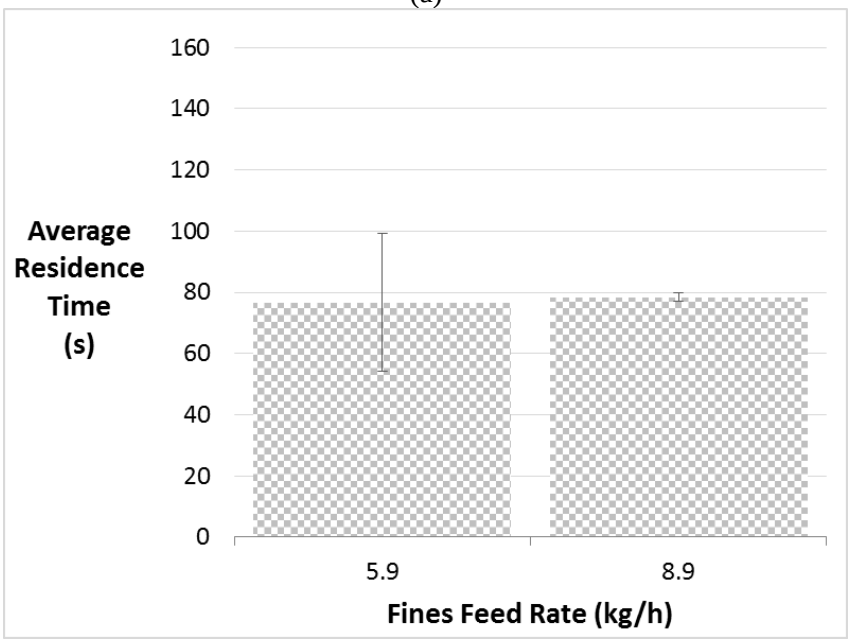

(b)

Figure 5.4. Fines average residence time comparison as a function of fines feed rate, 1200 kPa - TB present - 83 µm and at gas velocities of (a) 2.5 U_{mf} and (b) 3.0 U_{mf}.

In summary, increasing the fines feed rate was found to reduce the variance on the average residence time at elevated pressures, with the tube bank present and with the larger fines of 83 µm. Regarding possible mechanisms for why the average residence time would have a reduced variance

at a higher feed rate, the answer may be found in the oscillating nature of the fluidized bed. The entrainment in a fluidized bed is primarily governed by gas bubbles bursting at the bed surface with gas bubbles being the principal carrier of fines [25]. Hence, at a lower fines feed rate, the availability of fines at a given moment or location is lesser (m_{FB} is smaller), and therefore the amount being carried in the average bubble rising may be subject to greater variation. On the other hand, as the fines feed rate is increased, the fluidized bed becomes more concentrated with fines, and therefore the amount of fines at a given location or moment, should be more consistent. As a result, the average bubble rising and bursting at the surface, could be more consistent in the amount of fines carried. For which, bed hydrodynamics were not found to change as a function of the fines feed rate. Ultimately, it is anticipated that m_{FB} would periodically be more consistent at higher feed rates and therefore so should the fines average residence time in the fluidized bed.

5.3. Fines Average Residence Time Summary

In summary, the relevant findings for the fines average residence time in the fluidized bed as a function of the operating conditions are discussed in relation to the industrial application of a clean coal combustor. First, the effect of gas velocity was not statistically significant for the range tested in this work which could be advantageous to the combustor as it could allow for unforeseen disturbances in the gas velocity without it impacting the average residence time of fuel particles. Regarding operating at elevated pressures of 600-1200 kPa, the fines average residence time in the fluidized bed augmented or stayed constant as pressure was increased. This should help achieve the complete combustion of fuel particles at elevated pressures. For its part, the tube bank was not found to have a statistically significant impact on the fines average residence time in the fluidized bed (at the exception of 1 condition). However, it was successful at breaking the gas bubbles and reducing the average bubble size, such that it should provide better gas-solid contacting between phases in the combustor, which should enhance rates of reaction. In addition, the effect of increased fines feed rate at high pressure was found to improve the variance associated to the fines average residence time in the fluidized bed which should enable easier operation and process control. Finally, the effect of increased fines particle size was associated with greater fines average residence time in the fluidized bed. This is desired as the larger fuel particles will require more time to combust completely.

To conclude this chapter, a summary table (Table 5.2) is presented for all the results obtained for the fines average residence time. Table 5.2 presents the fines average experimental residence time θ_{total} (for the entire system), the fines average freeboard residence time, $\theta_{Freeboard}$, and consequently the fines average fluidized bed residence time, θ_{FB}, for each

operating condition tested. Furthermore, the value of twice the standard deviation for the fines average residence time in the fluidized bed used to construct the 95% confidence intervals is also tabulated (*2x Std. Dev. For* θ_{FB}).

On a last note, it is worth mentioning that the fines average residence time in the fluidized bed was substantially greater than those in the freeboard, despite the freeboard travel distance being greater (1.87 vs 1.07 m). In addition, the interstitial gas velocity was greater in the fluidized bed, even more so when the tube bank was present. Nonetheless, as seen in Table 5.2, the fines average residence time in the fluidized bed still ranged from 20-40 s or even 70-120 s in some cases; well above the average gas residence time of 1-2 s in the fluidized bed. This would suggest a substantial amount of interference by the large bed material for the fines in the fluidized bed, as the fines were spending a much longer time within than the gas on average. With that said, based on the average duration of fines in the fluidized bed it is not unreasonable to assume that the fines were backmixing in the fluidized bed. Finally, based on the greater fines average residence time in the fluidized bed for the 83 μm particles, it would suggest larger particles are more susceptible to being caught in the fluidized bed mixing patterns. Perhaps because they are heavier and therefore less dragged by the wake of passing bubbles.

Table 5.2. Fines average residence time summary table

Operating condition	Average Residence time (s)				
	θ_{total}	$\theta_{Freeboard}$	θ_{FB}	2x Std. Dev. For θ_{FB}	# of Trials
NO TB - 64 um					
101 kPa - 1.5 Umf - 5.9 kg/h	33.7	6.5	27.2	11.1	6
101 kPa - 1.9 Umf - 5.9 kg/h	27.3	4.3	23.0	6.4	7
600 kPa - 1.9 Umf - 5.9 kg/h	43.3	6.5	36.8	9.5	2
1200 kPa - 1.9 Umf - 5.9 kg/h	39.2	12.2	26.9	4.6	2
1200 kPa - 2.5 Umf - 5.9 kg/h	44.7	8.2	36.5	30.5	2
1200 kPa - 3.2 Umf - 5.9 kg/h	35.8	5.7	30.0	10.4	2
NO TB - 83 um					
101 kPa - 1.5 Umf - 5.9 kg/h	69.1	10.9	58.2	16.6	2
101 kPa - 1.9 Umf - 5.9 kg/h	34.8	6.4	28.4	15.3	2
600 kPa - 1.9 Umf - 5.9 kg/h	127.7	11.2	116.5	70.0	2
1200 kPa - 2.5 Umf - 5.9 kg/h	115.3	9.4	105.9	85.6	3
1200 kPa - 3.0 Umf - 5.9 kg/h	91.5	11.9	79.6	41.8	2
TB - 64 um					
101 kPa - 1.9 Umf - 5.9 kg/h	30.2	4.0	26.1	6.6	2
600 kPa - 1.9 Umf - 5.9 kg/h	51.8	6.9	44.8	9.3	2
1200 kPa - 1.9 Umf - 5.9 kg/h	42.5	12.7	29.8	13.8	2
1200 kPa - 2.5 Umf - 5.9 kg/h	46.2	9.0	37.2	17.4	4
1200 kPa - 3.2 Umf - 5.9 kg/h	43.4	6.1	37.3	N/A - 1 trial	1
TB - 83 um					
101 kPa - 1.5 Umf - 5.9 kg/h	44.3	11.9	32.4	5.7	2
101 kPa - 1.9 Umf - 5.9 kg/h	34.6	7.9	26.7	4.7	2
101 kPa - 1.9 Umf - 8.9 kg/h	30.1	7.4	22.7	1.6	2
600 kPa - 1.9 Umf - 5.9 kg/h	94.6	11.4	83.2	27.0	2
1200 kPa - 2.5 Umf - 5.9 kg/h	108.2	12.5	95.7	56.5	2
1200 kPa - 2.5 Umf - 8.9 kg/h	84.2	12.7	71.5	8.7	2
1200 kPa - 3.0 Umf - 5.9 kg/h	88.4	11.7	76.7	22.4	2
1200 kPa - 3.0 Umf - 8.9 kg/h	89.6	11.2	78.4	1.3	2

Chapter 6. Conclusion, Recommendations and Future Work

The oxygen-fired pressurized fluidized bed combustor is expected to have great potential in being an effective technology to help mitigate carbon dioxide emissions. Which is crucially important as the timeline to reduce GHG emissions is urgent with atmospheric CO_2 concentrations having surpassed the dangerous 400 ppm milestone [4]. Furthermore, it was shown that electricity and heat production is a significant source of GHG emissions at approximately 25% of total emissions [9], for which traditional coal combustion occupies a large share. CanmetENERGY and GTI were the leads for evaluating and designing the technology as a whole by building a pilot plant facility. Their efforts were supplemented from this research by providing information and experimental data regarding the system design and operation. In particular the fuel residence time, in relation to the effect of having in-bed heat exchanger tubes and high-pressure operation.

From the literature review, the effect of increased gas velocity and decreased particle size was expected to shorten the average residence time of fines in the fluidized bed. More significant was the combination of increased pressure with the presence of tube bank being able to limit bubble growth and induce the onset of turbulent fluidization at a lesser superficial gas velocity. As a result, gas-solid contacting would be much better under those conditions. While the reduced bubble size could impede entrainment of larger Geldart group B particles, it should be of lesser effect for group A particles. On that note, bed hydrodynamics were studied in parallel with the fines average residence time in the fluidized bed by measuring the differential pressure across the entire static bed height. Individually, the presence of tube bank or increased pressure was found to reduce bubble stability and broadened the bubble size distribution, but some large slugs still remained. It was only the combination of both, especially at 1200 kPa, that mitigated the slugging regime. As

a result, higher frequency, smaller bubbles were present at elevated pressure with the tube bank present with an estimated average bubble size of 4.4 cm.

Regarding results on the fines average residence time in the fluidized bed, the effect of gas velocity was not statistically significant for the range investigated. The effect of pressure was null for 64 µm fines, but for larger 83 µm fines there was an effect. Increased pressure increased the average residence time of fines in the fluidized bed at 1200 kPa when the tube bank was present. This was observed at constant excess gas velocity, while without a tube bank present, the effect of pressure was not statistically significant with 83 µm fines. At 600 kPa, increased pressure also increased the fines average residence time in the fluidized bed when using the 83 µm fines, at constant excess gas velocity and with the tube bank present. The effect of tube bank was not statistically significant for both sizes of fines at the exception of 1 operating conditions: 101 kPa – 1.5 U_{mf} – 83 µm. In addition, the effect of increased fines particle size was generally associated with greater fines average residence time in the fluidized bed.

Finally, increasing the fines feed rate was found to reduce the variance on the average residence time at elevated pressures, with the tube bank present and with the larger fines of 83 µm. It was hypothesized to be a result of the oscillating nature of the fluidized bed. For which, the fines average residence time in the fluidized bed is an oscillating process due to the bubble dynamics within. Such that, despite being at steady state, the mass of fines in the fluidized bed is constantly oscillating due to cycles of bubble ejection. Therefore the amount of fines being carried in the average bubble rising may be subject to greater variations at a lower fines feed rate due to a lower fines concentrations in the bed.

Recommendations for further pursuits concerning research on the average residence time of fines at cold flow conditions are presented next. First, as the effect of both pressure and the presence of tube bank were more unknown and valuable, it would be ideal to study the effect of pressure for a greater range of gas velocities at 600 and 1200 kPa. The excess gas velocity was a more adequate gas velocity parameter to study the effects of pressure compared to a constant U_g/U_{mf}. Nonetheless, the possibility of comparing the effect of pressure as a function of the actual independent variable, superficial gas velocity U_g, remains interesting. Regarding the presence of tube bank, it would be best to have the tube bank present across the entire fluidized bed, to prevent previously broken down bubbles from coalescing above, as was believed to occur. Currently, it was limited to a height of 0.50 m for a static bed height of 0.625 m. In comparison, keeping the static bed height constant between no tube bank and the tube bank present rather than the mass of large bed material could also be studied.

Furthermore, investigating the effect of fines particle size over a greater range could provide more statistically significant results for that parameter. Currently the two sizes of fines were relatively close with Sauter mean diameters of 64 and 83 µm. Meanwhile, the effect of fines feed rate could be investigated with the 64 µm fines as well. At last, more experimental trials would be beneficial in providing greater clarity over the source of the significant variation on the fines average residence time in the fluidized bed. Clarity on whether the variation is principally due to the minimum trials conducted for statistical significance i.e. 2, or the oscillating nature of bubbles within the fluidized bed.

Regarding future work, the fines average residence time in the fluidized was thoroughly studied as a function of 5 operating variables. What is most missing, is the significance of the

results at reactive conditions inside the real combustor. For which, the effect of temperature and its synergy with the previous effects remains unknown. Thus, it is planned to fit a non-linear model to the data as a function of the operating variables studied and extrapolate the results to reactive conditions. Which notably include changed minimum fluidization gas velocity, gas density, gas viscosity, fines particle density and gas composition at reactive conditions among others. Although, in the real application, coal would be combusted as it flows through the large bed material reducing its particle size. Thus the extrapolation of results to reactive conditions would provide an upper limit to the average residence time of fines in the Oxy-PFBC, and its range of applicability may be limited.

References

[1] NASA Global Climate Change, Climate change: How do we know?, retrieved December 20, 2016, from http://climate.nasa.gov/evidence/

[2] GRID-Arendal (2014), Vital Climate Graphics – Global atmospheric concentration of CO2, retrieved December 20, 2016, from http://www.grida.no/publications/vg/climate/page/3062.aspx

[3] Committee on Stabilization Targets for Atmospheric Greenhouse Gas Concentrations and National Research Council, Climate Stabilization Targets: Emissions, Concentrations, and Impacts over Decades to Millennia (2011), retrieved December 20, 2016, from https://www.nap.edu/read/12877/chapter/1

[4] 350.org, 400 ppm (2016), retrieved December 20, 2016, from http://400.350.org/

[5] NASA Global Climate Change, Graphic: Global warming from 1880 to 2013, retrieved December 20, 2016, from http://climate.nasa.gov/climate_resources/28/

[6] The University Corporation for Atmospheric Research (2016), Graphic: Global warming from 1880 to 2013, retrieved December 20, 2016, from https://www2.ucar.edu/climate/faq/how-much-has-global-temperature-risen-last-100-years.

[7] National Geographic (2016), Global Warming Fast Facts, retrieved December 20, 2016, from http://news.nationalgeographic.com/news/2004/12/1206_041206_global_warming.html.

[8] Statistics Canada (2011), Temperature trends in Canada, retrieved December 20, 2016, from http://www.statcan.gc.ca/pub/16-002-x/2011001/part-partie2-eng.htm.

[9] United States Environmental Protection Agency (2017), Global Greenhouse Gas Emissions Data, retrieved January 17, 2017, from https://www.epa.gov/ghgemissions/global-greenhouse-gas-emissions-data

[10] Green Eatz (n. d.), Food's Carbon Footprint, retrieved December 20, 2016, from http://www.greeneatz.com/foods-carbon-footprint.html

[11] Production and end-use data from Energy Information Administration, Annual Energy Review 2002.

[12] Annual Energy Review, Production and end-use data from Energy Information Administration, 2002.

[13] The Energy Collective (2017), Can Switching Heavy Duty Trucks to Rail Transport Reduce Carbon Emissions?, retrieved April 4, 2017, from http://www.theenergycollective.com/jemiller_ep/248811/can-switching-heavy-duty-trucks-rail-transport-substantially-reduce-us-carbon-emis

[14] Treehugger (2017), Rail Versus Trucking: Who's The Greenest Freight Carrier?, retrieved April 4, 2017, from http://www.treehugger.com/cars/rail-versus-trucking-whos-the-greenest-freight-carrier.html

[15] Toyota Motor Corporation (2016), Ascent Sedan Manual, retrieved December 20, 2016, from http://www.toyota.com.au/corolla/specifications/ascent-sedan-manual.

[16] S. C. Walpole, D. Prieto-Merino, P. Edwards, J. Cleland, G. Stevens, I. Roberts, The weight of nations: an estimation of adult human biomass, BMC Public Health Vol. 12, No. 1, pp. 439, 2012.

[17] United Nations Department of Economic and Social Affairs (2016), World population projected to reach 9.7 billion by 2050, retrieved December 20, 2016, from http://www.un.org/en/development/desa/news/population/2015-report.html.

[18] CBC/Radio-Canada (2017), Syrian civil war: The costs after 5, retrieved March 20, 2017, from http://www.cbc.ca/news/world/syria-war-after-five-years-1.3489326

[19] CNBC (2017), Syria war could cost country $1.3T by 2020: Study, retrieved March 25, 2017, from http://www.cnbc.com/2016/03/08/syria-war-could-cost-country-13t-by-2020-study.html

[20] International Energy Agency (2011), Emissions from coal fired power Generation, retrieved March 8, 2017, from https://www.iea.org/media/workshops/2011/cea/Ito.pdf

[21] C. D. Cooper, F. C. Alley, Air Pollution Control Fourth Edition. Long Grove, IL, USA; Waveland Press Inc., 2011.

[22] G. T. Rochelle, 2009, Amine Scrubbing for CO Capture, Science Vol. 325, No. 5948, pp. 1652-1654. Retrieved March 8, 2017 from http://science.sciencemag.org/content/325/5948/1652.full

[23] How Products Are Made (2017), Oxygen Background, retrieved March 9, 2017, from http://www.madehow.com/Volume-4/Oxygen.html

[24] Universal Industrial Gases (2016), Oxygen (O_2) Properties, Uses, Applications, retrieved March 9, 2017, from http://www.uigi.com/oxygen.html

[25] W-C. Yang, Handbook of Fluidization and Fluid-Particle Systems. Pittsburg, PA, USA; Marcel Dekker Inc., 2003.

[26] D. Geldart, Types of gas fluidization, Powder Technology, Vol. 5, No. 5, pp. 285-292, 1973.

[27] J. Ruud van Ommen, N. Ellis, Fluidization, JMBC/OSPT course Particle Technology (2010), retrieved March 24, 2017, from https://www2.msm.ctw.utwente.nl/sluding/TEACHING/ParticleTechnology/vanOmmen_Fluidization.pdf

[28] A. Haider and O. Levenspiel, Drag coefficient and terminal velocity of spherical and nonspherical particles, Powder Technology, Vol. 58, No. 1, pp. 63-70, 1989.

[29] E Hoekstra, S. Sookai, The effect of gas density on fluidized-bed entrainment, South African Journal of Chemical Engineering, Vol. 19, No. 3, pp. 90-98, 2014.

[30] R. Clift, J. R. Grace and M. E. Weber, Bubbles, drops, and particles. New York: Academic Pres, 1978.

[31] R. Turton, O. Levenspiel, A short note on the drag correlation for spheres, Powder Technology, Vol. 47, No. 1, pp. 83-86, 1986.

[32] C-Y. Wen and R. F. Hashinger, Elutriation of solid particles from a dense-phase fluidized bed, AIChE Journal, Vol. 6, No. 2, pp. 220-226, 1960.

[33] M. Leva, Elutriation of fines from fluidized systems, Chemical Engineering Progress, issue 47, No. 1, pp. 39-45, 1951.

[34] G. L. Osberg, Industrial & Engineering Chemistry, issue 47, pp. 566, 1951.

[35] J. G. Yates, Review article number 49 - Effects of temperature and pressure on gas-solid fluidization, Chemical Engineering Science, Vol. 51, No. 2, pp. 167-205, 1996.

[36] P. R. Tardin Jr., L. Goldstein Jr. and W. A. Bizzo, Entrainment of FCC particles from a pilot-scale fluidized bubbling bed. Part 1: experimental study, Powder Technology, Vol. 269, No. 1, pp. 596-604, 2015.

[37] J. Baeyens, D. Geldart and S.Y. Wu, Elutriation of fines from gas fluidized beds of Geldart A-type powders – effect of adding superfines, Powder Technology, Vol. 71, No. 1, pp. 71-80, 1992.

[38] X. Ma and K. Kato, Effects of interparticle adhesion forces of fine powders from a fluidized bed of a binary particle mixture, Powder Technology, Vol. 95, No. 2, pp. 93-101, 1998.

[39] M. Colakyan and O. Levenspiel, Elutriation from fluidized beds, Powder Technology, Vol. 38, No. 3, pp. 223-232, 1984.

[40] I Tanaka, H. Shinohara, H. Horisue and Y. Tanaka, Elutriation of fines from a fluidized bed, Journal of Chemical Engineering of Japan, Vol. 5, No. 1, pp. 51-57, 1972.

[41] C. D. Cooper, F.C. Alley, Air Pollution Control – A Design Approach: Cyclones, 2011.

[42] S. Yagi and D. Kunii, Fluidized-solids reactors with continuous solids feed-1 Residence time of particles in fluidized beds, Chemical Engineering Science, Vol. 16, No. 3-4, pp. 364-371, 1961.

[43] A. C. Hoffman, J. G. Yates, Experimental observations of fluidized beds at elevated pressures, Chemical Engineering Communications, Vol. 41, No. 1, pp. 133-149, 1986.

[44] P. C. Upson, D. L. Pyle, The stability of bubbles in fluidized beds, Fluidization and its Applications, pp. 207-222. Società di La Chimica e l'Industria., Paris, 1973.

[45] R. Clift, J. R. Grace, M. E. Weber, Stability of bubbles in fluidized beds, J E C Funds, Vol. 13, No. 1, pp. 45-51, 1974.

[46] D. F. King, D. Harrison, The bubble phase in high pressure fluidized beds, Fluidization, pp. 133-149, 1980. Plenum, New York.

[47] P. A. Olowson, A. E. Almstedt, Influence of pressure and fluidization velocity on the bubble behavior and gas flow distribution in a fluidized bed, Chemical Engineering Science, Vol. 39, No. 1, pp. 1733-1741, 1990.

[48] J. R. van Ommen, S. Sasic, J. van der Schaaf, S. Gheorghiu, F. Johnsson and M-O. Coppens, 2011, Time-series analysis of pressure fluctuations in gas-solid fluidized beds – A review, International Journal of Multiphase Flow 37, 403–428.

[49] M. Liu, Y. Zhang, H. Bi, J. R. Grace and Y. Zhu, 2010, Non-intrusive determination of bubble size in a gas-solid fluidized bed: An evaluation, Chemical Engineering Science 65, 3485-3493.

[50] Bi, H.T., 2007. A critical review of the complex pressure fluctuation phenomenon in gas–solids fluidized beds. Chem. Eng. Sci. 62, 3473–3493.

[51] Sasic, S., Leckner, B., Johnsson, F., 2007. Characterization of fluid dynamics of fluidized beds by analysis of pressure fluctuations. Prog. Energy Combust. Sci. 33, 453–496.

[52] J. G. Yates and R. S. Ruiz-Martinez, Interaction between horizontal tubes and gas bubbles in a fluidized bed, Chemical Engineering Communications, Vol. 62, pp. 67-78, 1987.

[53] J. G. Yates, R. S. Ruiz-Martinez and D. J. Cheesman, Prediction of bubble size in a fluidized bed containing horizontal tubes, Chemical Engineering Science, Vol. 45, No. 4, pp. 1105-1111, 1990.

[54] S. E. Olsson, J. Wiman and A. E. Almstedt, Hydrodynamics of a pressurized fluidized bed with horizontal tubes: influence of pressure, fluidization velocity, and tube-bank geometry, Chemical Engineering Science, Vol. 50, No. 4, pp. 581-592, 1995.

[55] J. Wiman and A. E. Almstedt, Hydrodynamics, erosion and heat transfer in a pressurized fluidized bed: influence of pressure, fluidization velocity, particle size and tube-bank geometry, Chemical Engineering Science, Vol. 52, No. 16, pp. 2677-2695, 1997.

[56] J. Chew, et al., Review of entrainment correlations in gas-solid fluidization, Chemical Engineering Journal, Vol. 260, pp. 152-171, 2015.

[57] Anval (n.d.), Bulk density chart, retrieved July 19, 2016, from http://www.anval.net/downloads/bulk%20density%20chart.pdf

[58] P. A. Olowson and A. E. Almstedt, Influence of pressure and fluidization velocity on the bubble behavior and gas flow distribution in a fluidized bed, Chemical Engineering Science, Vol. 45, pp. 1733-1741, 1990.

[59] H. Löfstrand, A. E. Almstedt and S. Andersson, Dimensionless expansion model for bubbling fluidized beds with and without internal heat exchanger tubes, Chemical Engineering Science, Vol. 50, pp. 245-253, 1995.

[60] D. Rong and M. Horio, Behavior of particles and bubbles around immersed tubes in a fluidized bed at high temperature and pressure: a DEM simulation, International Journal of Multiphase Flow, Vol. 27, pp. 89-105, 2001.

[61] H. Yurong, L. Huilin, S. Qiaoqun, Y. Lidan, Z. Yunhua, D. Gidaspow and J. Bouillard, Hydrodynamics of gas-solid flow around immersed tubes in bubbling fluidized beds, Powder Technology, Vol. 145, pp. 88-105, 2004.

[62] J. Yerushalmi and N.T. Cankrut, Further studies of the regimes of fluidization, Powder Technology, Vol. 24, pp. 187-205, 1979.

[63] D. Kunii and O. Levenspiel, Fluidized reactor models 1. For bubbling beds of fine, intermediate, and large particles 2. For the lean phase: freeboard and fast fluidization, Industrial & Engineering Chemistry Research, Vol. 29, pp. 1226-1234, 1990.

[64] H. Li and Y. Tomita, Particle velocity and concentration characteristics in a horizontal dilute swirling flow pneumatic conveying, Powder Technology, Vol. 107, pp. 144-152, 2000.

[65] C. Y. Wen, L. H. Chen, Fluidized bed freeboard phenomena: entrainment and elutriation, AIChE Journal, Vol. 28, No. 1, pp. 117-128, 1982

[66] F. A. Zenz, N. A. Weil, A theoretical-empirical approach to the mechanism of particle entrainment from fluidized beds, AIChE Journal, Vol. 4, No. 4, pp. 472-479, 1958

[67] N. Nakagawa, S. Arita, H. Uchida, N. Takamura, T. Takarada, K. Kato, Particle hold-up and elutriation rate in the freeboard of fluid beds, Journal of Chemical Engineering of Japan, Vol. 27, No. 1, pp. 79-84, 1994

[68] J-H. Choi, I-Y. Chang, D-W. Shun, C-K Yi, J-E. Son, S-D. Kim, Correlation on the particle entrainment rate in gas fluidized beds, Industrial & Engineering Chemistry Research, Vol. 38, No. 6, pp. 2491-2496, 1999

[69] S. M. Tasirin, D. Geldart, Entrainment of fines from fluidized beds with an expanded freeboard, Chemical Engineering Communications, Vol. 166, No. 1, pp. 217-230, 1998.

[70] S. M. Tasirin, Ph.D. Thesis, University of Bradford, United Kingdom. 1995.

[71] S. Yagi, D. Kunii, Fluidized-solids reactors with continuous solids feed-1: Residence time of particles in fluidized beds, Chemical Engineering Science, Vol. 16, No. 3-4, pp. 364-371, 1961.

[72] J. Ruud van Ommen, J. C. Schouten, M. L. M. vander Stappen, C. M. van den Bleek, Response characteristics of probe-transducer systems for pressure measurements in gas-solid fluidized beds: how to prevent pitfalls in dynamic pressure measurements, Powder Technology, Vol. 106, No. 1, pp. 199-218, 1999.

Appendix A: Detailed Pictures of the Fluidization Apparatus

The following appendix includes various pictures of the fluidization apparatus used for this research.

Figure A.1. Vertical profile of the 2.94 m fluidization column.

Figure A.2. View of the pressure vessel containing the feeder. The outlet tee has the auger pushing out the solids horizontally with the pneumatic convey gas coming from the top.

Figure A.3. Pressure vessel containing the feeder. Focus on the outlet tee used to discharge solids into the pneumatic convey line.

The auger pushes out the solids horizontally with the convey gas coming from the top in 0.013 m (1/2 in.) tubing. The gas and solids were funnel together and exited at the bottom into a 0.006 m (1/4 in.) convey line.

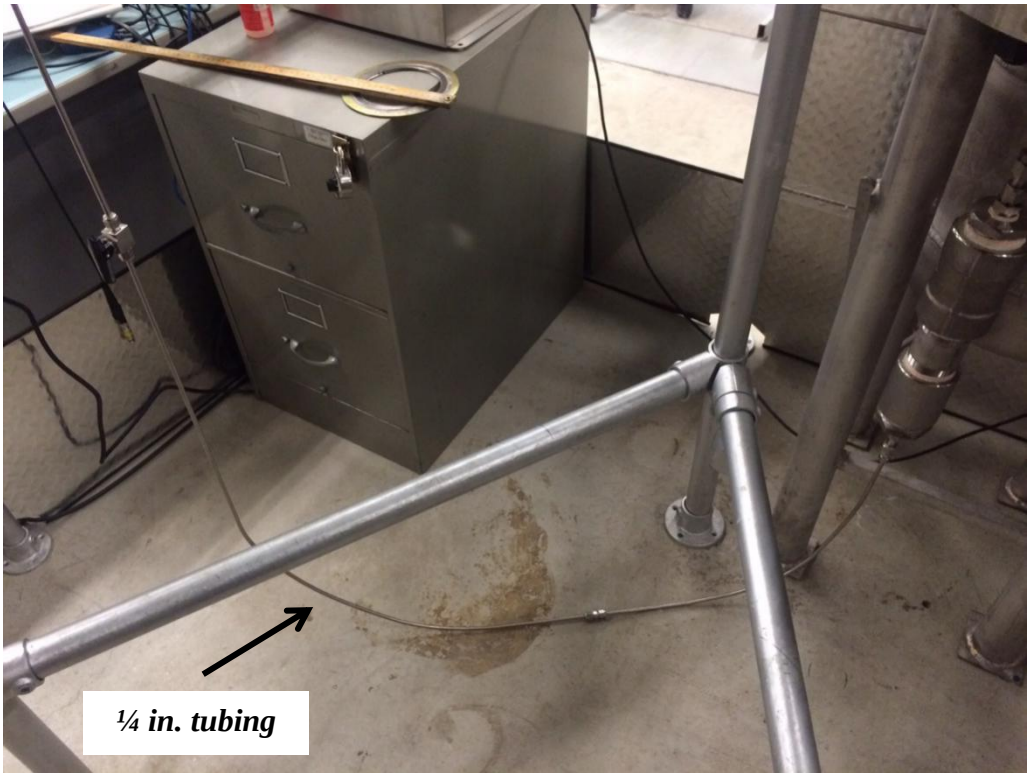

Figure A.4. View of the initial section of the 0.006 m (1/4 in.) pneumatic convey line for fines.

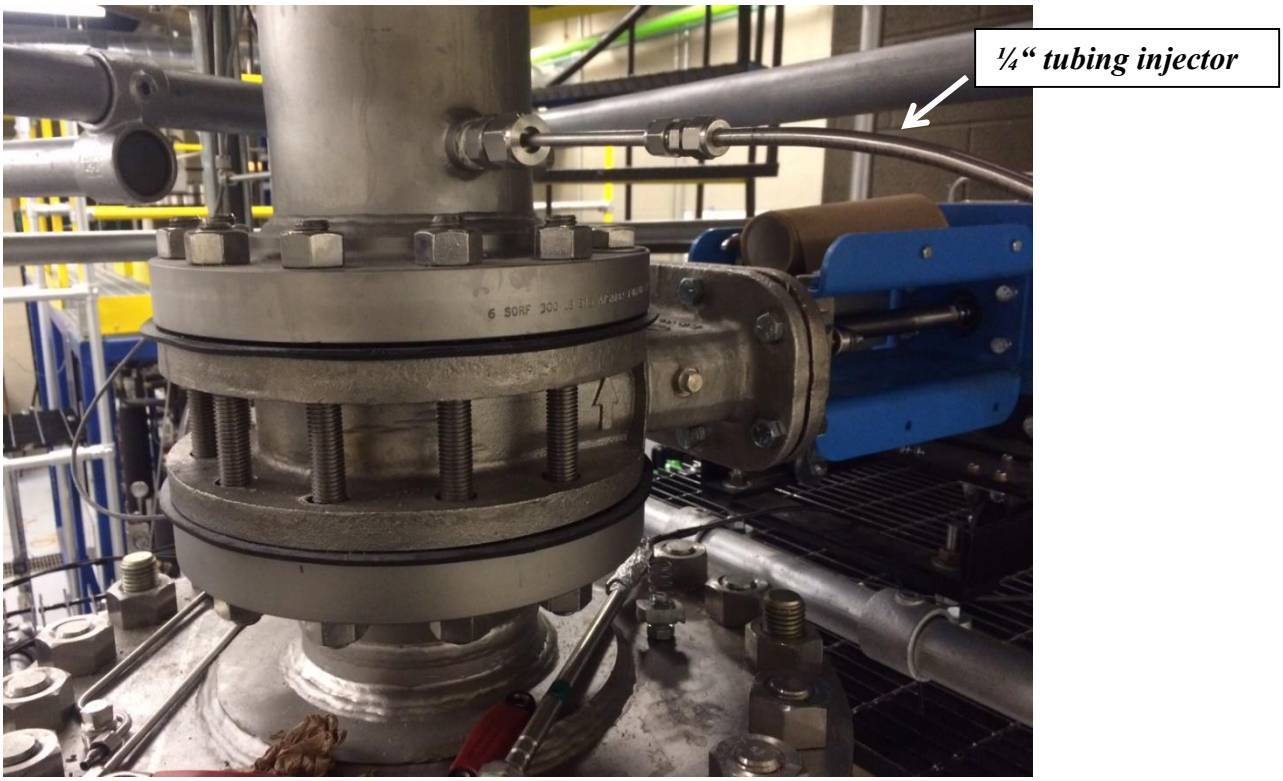

Figure A.5. View of the injection port used for fines injection at the center of the fluidized bed above the distributor plate.

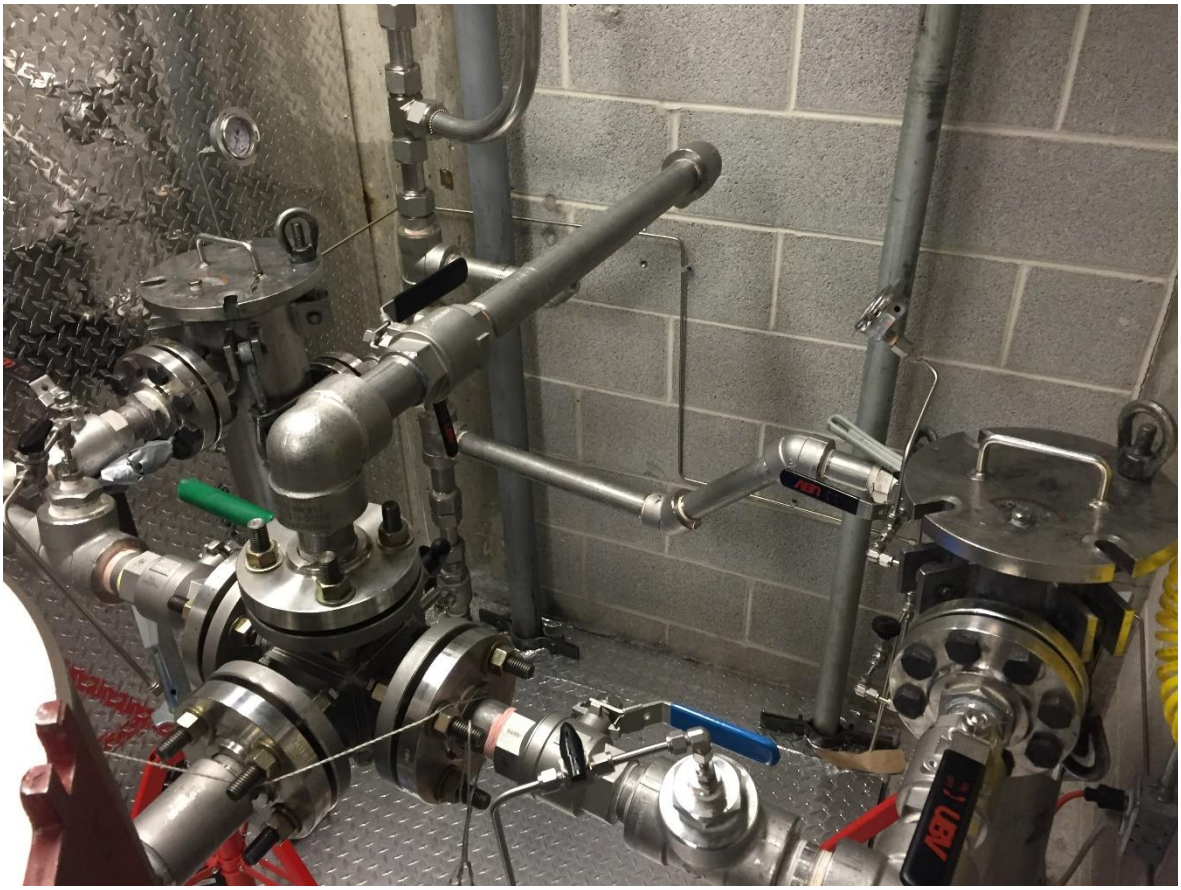

Figure A.6. View of the capture system with both filters in parallel.

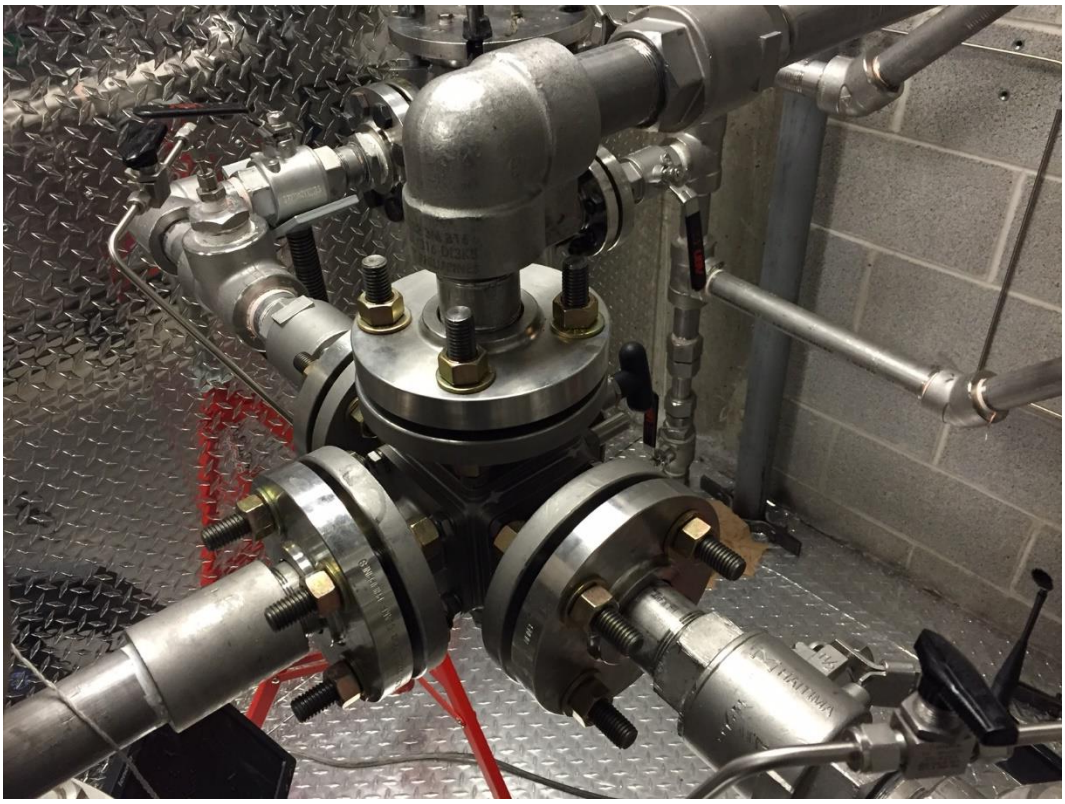

Figure A.7. View of the 3-way outlet valve.

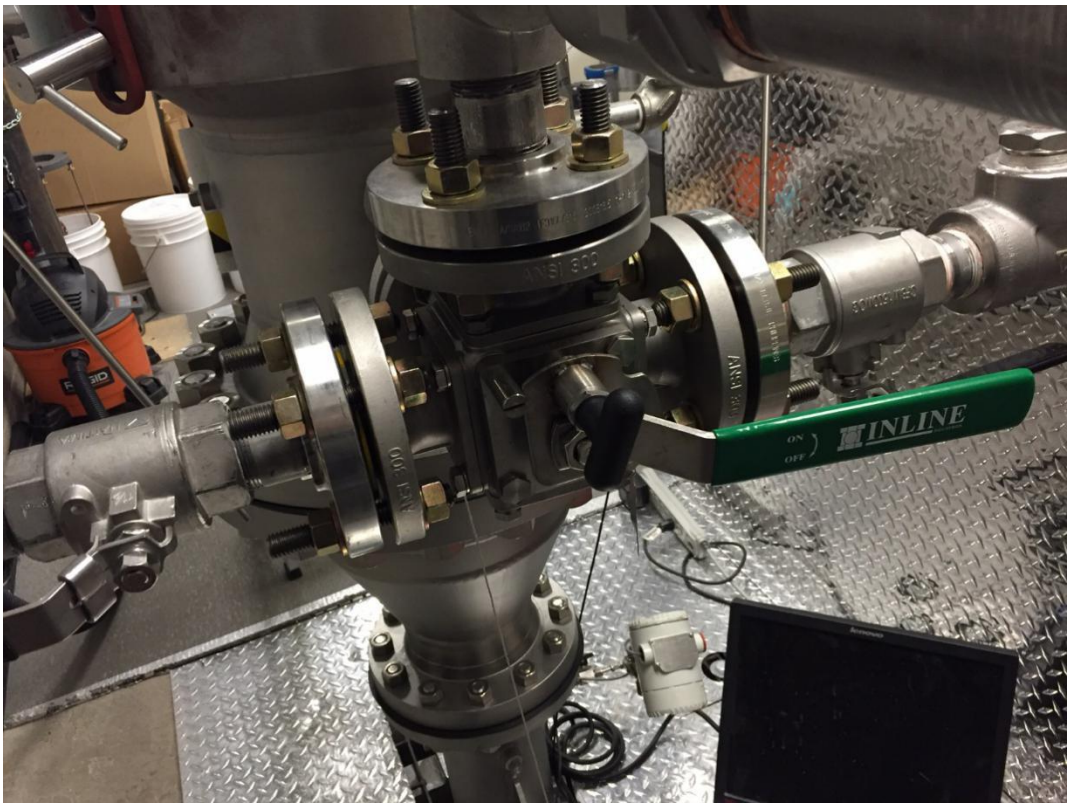

Figure A.8. View of the lever for the 3-way outlet valve.

Figure A.9. View of the large elbow. Approximate height of 0.42 m.

Appendix B: Schematic of the Tube Bank

Here is the schematic of the tube bank sleeve lowered in the column during experiments with a tube bank. The length of the tube bank was 0.50 m with an inner diameter of 0.14 m.

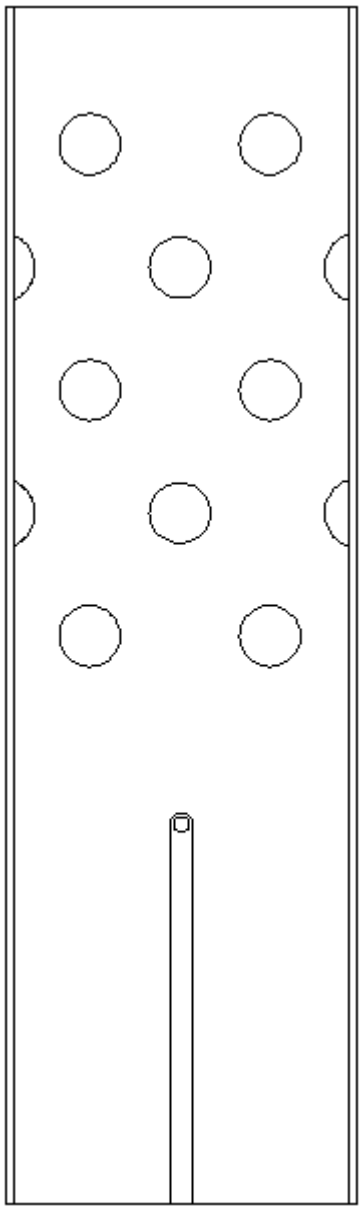

Figure B.1. Schematic of the tube bank, due to confidentiality reasons, and to protect GTI proprietary information, dimensions were not provided.

Appendix C: Fines Particle Size Distribution

The following table presents the particle size distribution of fines used in this work as the coal surrogate. The distribution was obtained with the Malvern Mastersizer instrument which uses the technique of laser diffraction to measure particle size. The two types of fines had Sauter mean particle diameters of 64 and 83 μm respectively.

Table C.1. Fines particle size distribution for the two different types of fines used

Particle size (um)	**Weight percentage (%)**	
	64 μm fines	**83 μm fines**
30.2	0.02	0.00
34.7	0.28	0.00
39.8	1.76	0.01
45.7	5.22	0.36
52.5	10.74	2.01
60.3	16.59	6.01
69.2	19.99	11.98
79.4	19.00	18.11
91.2	14.16	20.73
104.7	8.09	19.03
120.2	3.33	12.21
138.0	0.77	7.05
158.5	0.06	2.13
182.0	0.00	0.38

Attached below are the two respective histograms for the PSD of 64 and 83 μm fines.

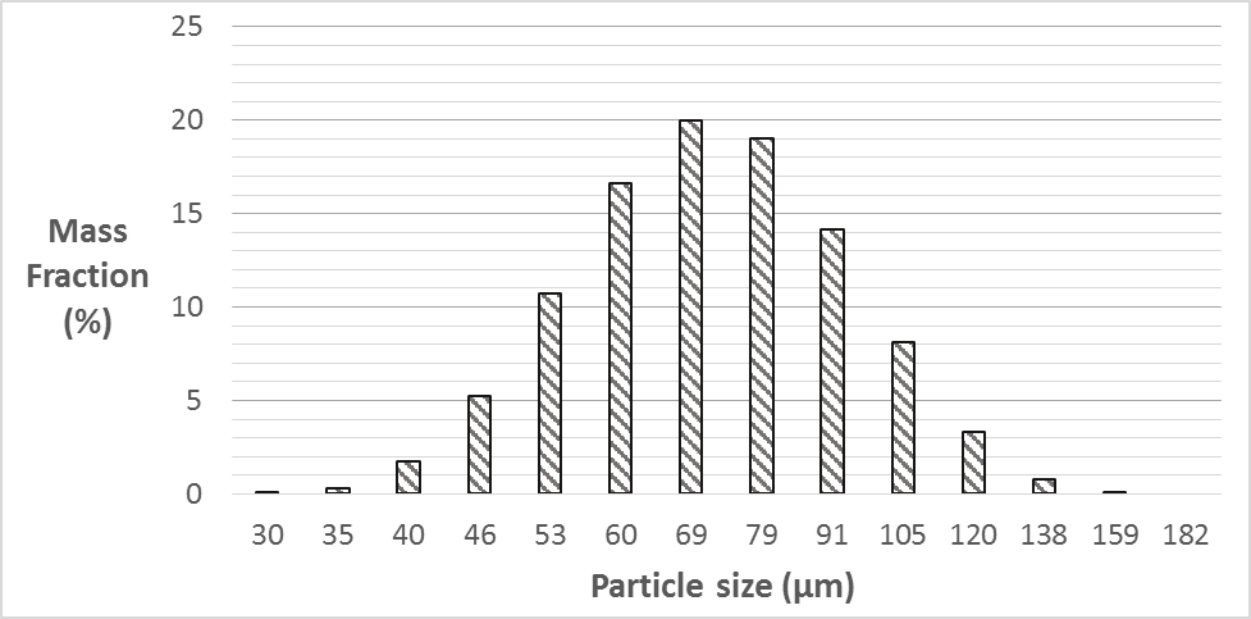

Figure C.1. PSD histogram of the 64 µm fines used for experiments.

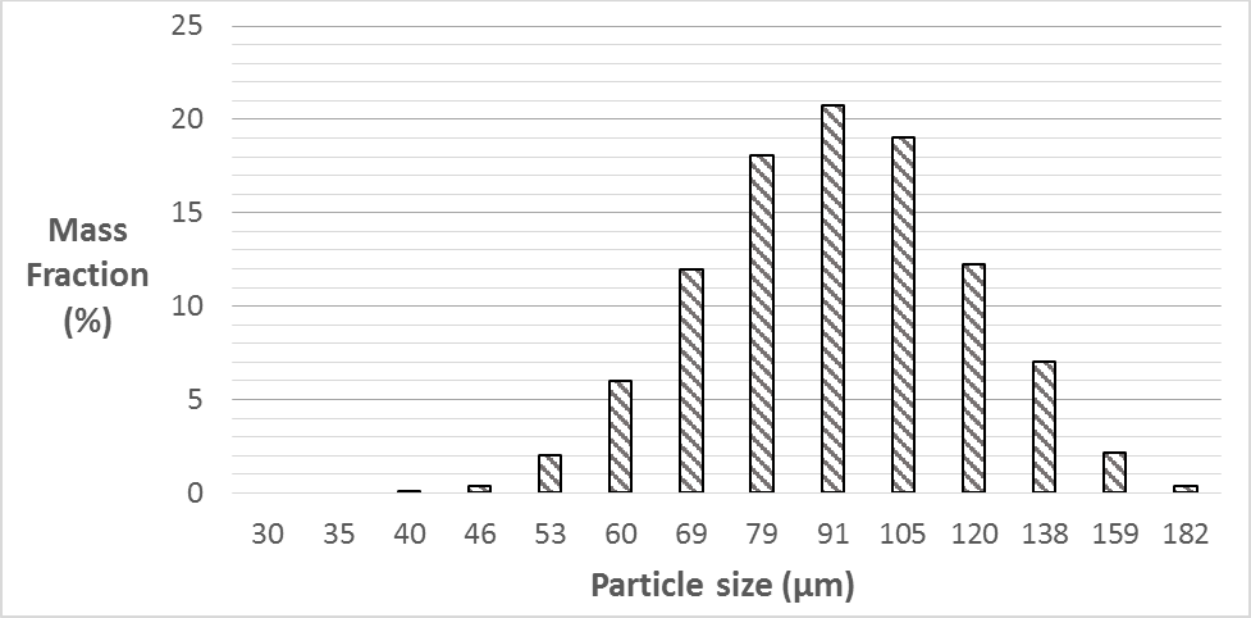

Figure C.2. PSD histogram of the 83 µm fines used for experiments.

Appendix D: Fines Terminal Velocity

Table D.1. Particle terminal velocity as a function of particle size and pressure.

Particle size (µm)	**40**	**46**	**52**	**60**	**69**	**79**	**91**	**105**	**120**	**138**	**158**
Terminal velocity at 101 kPa (m/s)	0.11	0.15	0.18	0.24	0.30	0.38	0.47	0.58	0.71	0.86	1.02
Terminal velocity at 600 kPa (m/s)	0.10	0.12	0.15	0.19	0.23	0.27	0.33	0.39	0.46	0.54	0.62
Terminal velocity at 1200 kPa (m/s)	0.09	0.11	0.13	0.16	0.20	0.23	0.27	0.32	0.38	0.44	0.51

Appendix E: Operating Gas and Minimum Fluidization Velocities

The table below contains the superficial and excel gas velocities for the various multiples of U_{mf} tested. Values underlined were those tested for a given pressure. Not all conditions of interest could be tested due to limitations with the experimental apparatus. U_{ex} denotes the excess gas velocity $U_g - U_{mf}$.

Table E.1. Absolute operating gas velocities for each operating pressure for the various operating factors of the minimum fluidization velocity.

Gas velocity (U_g/U_{mf})	**1**		**1.5**		**1.9**		**2.5**		**3.2**	
	U_g	U_{ex}	U_g	U_{ex}	U_g	U_{ex}	U_g	U_{ex}	U_g	U_{ex}
101 kPa (m/s)	0.57	0	0.86	0.29	1.08	0.51	1.43	0.86	1.83	1.26
600 kPa (m/s)	0.33	0	0.49	0.16	0.62	0.29	0.82	0.49	1.04	0.72
1200 kPa (m/s)	0.23	0	0.35	0.12	0.44	0.21	0.58	0.35	0.74	0.51